

**Radiation Pattern Analysis  
of the Tapered Slot Antenna**

**Ramakrishna Janaswamy**

*M-32*

*63688*

**ANTLAB Report No. 8602**

**August 1986**

**Department of Electrical and Computer Engineering  
University of Massachusetts  
Amherst, MA 01003**

**RADIATION PATTERN ANALYSIS OF THE TAPERED SLOT ANTENNA**

**A Dissertation Presented**

**by**

**RAMAKRISHNA JANASWAMY**

**Submitted to the Graduate School of the  
University of Massachusetts in partial fulfillment  
of the requirements for the degree of**

**DOCTOR OF PHILOSOPHY**

**September 1986**

**Department of Electrical and Computer Engineering**

This Research was supported in part by the  
NASA Langley Research Center under  
Grant NAG-1-279

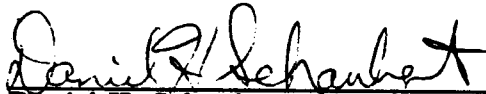
# RADIATION PATTERN ANALYSIS OF THE TAPERED SLOT ANTENNA

A Dissertation Presented

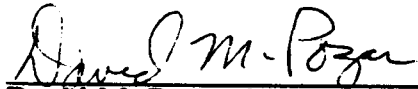
by

RAMAKRISHNA JANASWAMY

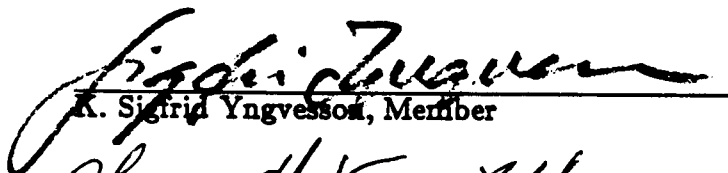
Approved as to style and content by:



Daniel H. Schaubert, Chairperson of Committee



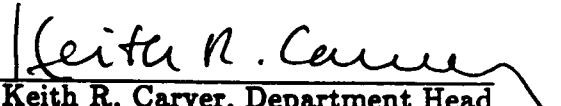
David M. Pozar, Member



K. Sigrid Yngvesson, Member



George H. Knightly, External Member



Keith R. Carver, Department Head  
Electrical and Computer Engineering

*To my Mother and Father*

SARALA and MARKANDEYA SASTRY

*Between the paths of pleasures, and pains,  
they chose to tread the latter.*

## ACKNOWLEDGEMENT

I would like to take this opportunity to express my deepest sense of gratitude to my advisor, Professor Daniel H. Schaubert. What I have amassed from him—both technically and socially—during my short stay here, shall leave a lasting impression on me. I owe him a lot for moulding my thought from a total naivety to the present maturity. I hope more and more students are benefited through him. I am also thankful to Professors David M. Pozar and K. Sigfrid Yngvesson for providing me with many technical suggestions without which this work could not have been completed. I must express my sincere thanks to Professor George H. Knightly of the Department of Mathematics for serving as a member of my committee. Finally, I would like to express my thanks to all my colleagues—past and present—for their many useful discussions and for making my stay here very enjoyable.

## ABSTRACT

### RADIATION PATTERN ANALYSIS OF THE TAPERED SLOT ANTENNA

SEPTEMBER 1986

*Ramakrishna Janaswamy*, B.Tech., R.E.C., WARANGAL, INDIA

M.Tech., I.I.T., KHARAGPUR, INDIA

Ph.D., UNIVERSITY OF MASSACHUSETTS

Directed by: Professor Daniel H. Schaubert

A theoretical model for the radiation characteristics of the tapered slot antenna is presented. The theory presented is valid for antennas having an arbitrary and smooth taper shape. The model adequately predicts the pattern dependence on the structural parameters of the antenna such as its length, the taper shape, the dielectric substrate and its thickness. The antenna is modelled as a tapered slot radiating in the presence of a conducting half-plane. The electric field distribution in the tapered slot is determined by effecting a stepped approximation to the continuous taper. Data on a uniform slot line is used to determine the slot field distribution in the stepped model. The uniform slot line is solved by the spectral Galerkin's method and data on the slot wavelength and the characteristic impedance are generated. Closed form expressions for these slot line parameters are developed. The half-plane Green's function is used to compute the radiated fields from the tapered slot. Comparison is made between the computed and measured radiation patterns. Results are presented for the cases of a constant width, a linear taper and an exponential taper of the slot and the versatility of the model in treating an arbitrary slot taper is demonstrated. Newly observed experimental effects concerning the pattern dependence on the lateral dimension of the antenna are presented. Studies done to account for these effects for the special case of an air dielectric antenna are presented.

## TABLE OF CONTENTS

ACKNOWLEDGEMENT . . . . .	v
ABSTRACT . . . . .	vi
LIST OF TABLES . . . . .	ix
LIST OF FIGURES . . . . .	x
Chapter	
1. INTRODUCTION . . . . .	1
2. METHOD OF ANALYSIS . . . . .	4
3. SLOT LINE DATA ON LOW PERMITTIVITY SUBSTRATES . . . . .	9
3.1 Formulation of the Problem . . . . .	9
1. Slot Wavelength . . . . .	11
2. Characteristic Impedance . . . . .	12
3.2 Numerical Results and Discussion . . . . .	13
3.3 Closed Form Expressions for $\lambda'$ and $Z_0$ . . . . .	15
4. FAR-FIELDS OF THE ANTENNA . . . . .	24
4.1 TEM-LTSA . . . . .	24
1. Formulation . . . . .	24
2. Numerical Results and Discussion . . . . .	28
4.2 Dielectric Supported Antennas . . . . .	36
1. Stepped Approximation . . . . .	36
4.3 Numerical Results and Discussion . . . . .	40
1. LTSA . . . . .	42
2. CWSA . . . . .	60
3. Vivaldi . . . . .	63
4. Use of Curve-Fitted Slot Line Data . . . . .	68
5. EFFECT OF LATERAL TRUNCATION ON THE ANTENNA PATTERN . . . . .	76
5.1 Experimental Results . . . . .	76
5.2 Theoretical Studies . . . . .	80



6. CONCLUSION . . . . .	92
APPENDIX	
A. EFFECT OF ADHESIVE ON SLOT WAVELENGTH . . . . .	94
B. MEASURED RADIATION PATTERNS . . . . .	96
BIBLIOGRAPHY . . . . .	106

## LIST OF TABLES

### Table

3.1	Comparison of computed slot wavelength. . . . .	15
3.2	Comparison of computed and measured slot wavelength. . . . .	15
3.3	Effect of adhesive on slot wavelength. . . . .	19
3.4	Comparison of computed characteristic impedance. . . . .	19
4.1	Pattern comparison for TEM-LTSA. . . . .	44
4.2	Pattern comparison for $\epsilon_r = 2.22$ LTSA. . . . .	44

## LIST OF FIGURES

### Figure

2.1	Geometry of LTSA. (a) Original problem (c) Stepped approximation. . . . .	5
3.1	Geometry of slot line. . . . .	10
3.2	Normalized slot wavelength versus slot width. . . . .	20
3.3	Characteristic impedance of slot line versus slot width. . . . .	21
3.4	Normalized slot wavelength versus slot width. . . . .	22
3.5	Characteristic impedance of slot line versus slot width. . . . .	23
4.1	Geometry of coplanar bifin structure. . . . .	25
4.2	Radiation patterns—relative contributions of forward and backward waves. . . . .	29
4.3	Radiation pattern of TEM-LTSA. . . . .	31
4.4	Measured and computed beamwidths of TEM-LTSA versus flare-angle. . . . .	32
4.5	E-plane beamwidth of TEM-LTSA versus normalized length. . . . .	33
4.6	H-plane beamwidth of TEM-LTSA versus normalized length. . . . .	35
4.7	Geometry of Tapered Slot Antenna. (a) Original problem (b) Stepped approximation. . . . .	37
4.8	Radiation patterns of TEM-LTSA obtained using stepped approximation and exact aperture distribution. . . . .	41
4.9	Measured and computed radiation patterns of LTSA on thin substrate. . . . .	43
4.10	Radiation patterns of LTSA on thin substrate obtained using <i>corrected</i> and <i>uncorrected</i> slot wavelengths. . . . .	46

4.11	Computed radiation patterns of LTSA on thin substrate, obtained using <i>generated</i> slot line data and <i>curve-fitted</i> slot line data. . . .	48
4.12	Measured and computed radiation patterns of a wide-flare-angle LTSA on thin substrate. . . . .	49
4.13	Computed radiation patterns of wide-flare-angle LTSA obtained using <i>corrected</i> and <i>uncorrected</i> slot wavelengths. . . . .	50
4.14a	Measured and computed radiation patterns of LTSA on thick substrate. Frequency = 12 GHz . . . . .	52
4.14b	Effect of wavelength correction on the radiation pattern of LTSA on thick substrate. . . . .	53
4.15	Measured and computed radiation patterns of LTSA on thick substrate. Frequency = 8 GHz. . . . .	55
4.16a	Measured and computed radiation patterns of LTSA on high- $\epsilon_r$ substrate. Frequency = 8 GHz . . . . .	56
4.16b	Effect of wavelength correction on the radiation pattern of LTSA on high- $\epsilon_r$ substrate. . . . .	57
4.17	Measured and computed radiation patterns of LTSA on high- $\epsilon_r$ substrate. Frequency = 10 GHz. . . . .	59
4.18	Geometry of CWSA. . . . .	61
4.19a	Measured and computed radiation patterns of CWSA on thin substrate. Frequency = 10 GHz. . . . .	62
4.19b	Effect of backward wave on CWSA pattern. . . . .	64
4.20	Computed radiation patterns of CWSA on thin substrate obtained using <i>corrected</i> and <i>uncorrected</i> slot wavelengths. . . . .	65
4.21	Measured and computed radiation patterns of CWSA on thin substrate. Frequency = 8 GHz. . . . .	66
4.22	Measured and computed radiation patterns of Vivaldi antenna on a 1/2-inch styrofoam sheet. . . . .	67
4.23	Computed radiation patterns of CWSA— <i>generated</i> and <i>curve-fitted</i> slot line data. . . . .	69

4.24	Computed radiation patterns of LTSA— <i>generated and curve-fitted</i> slot line data. . . . .	70
4.25	Computed radiation patterns of Vivaldi— <i>generated and curve-fitted</i> slot line data. . . . .	71
4.26	Computed radiation patterns of CWSA— <i>generated and curve-fitted</i> slot line data. . . . .	73
4.27	Computed radiation patterns of LTSA— <i>generated and curve-fitted</i> slot line data. . . . .	74
4.28	Computed radiation patterns of Vivaldi— <i>generated and curve-fitted</i> slot line data. . . . .	75
5.1	Measured radiation pattern of LTSA on a 1-inch styrofoam sheet as a function of $H$ . ( $L = 24$ cm, $W_f = 1.5$ mm, $W_o = 5.1$ cm, $f = 9$ GHz) . . . . .	77
5.2	Measured radiation pattern of LTSA on a 1-inch styrofoam sheet as a function of $H$ . ( $L = 24$ cm, $W_f = 1.5$ mm, $W_o = 5.1$ cm, $f = 9$ GHz) . . . . .	78
5.3	Measured radiation pattern of LTSA on a 1-inch styrofoam sheet as a function of $H$ . ( $L = 24$ cm, $W_f = 1.5$ mm, $W_o = 5.1$ cm, $f = 9$ GHz) . . . . .	79
5.4	Measured radiation pattern of LTSA on Duroid substrate as a function of $H$ . ( $L = 12.6$ cm, $W_f = 1$ mm, $W_o = 2.2$ cm, $\epsilon_r = 2.22$ , $d = 20$ mils, $f = 8$ GHz) . . . . .	81
5.5	Measured radiation pattern of LTSA on Duroid substrate as a function of $H$ . ( $L = 12.6$ cm, $W_f = 1$ mm, $W_o = 2.2$ cm, $\epsilon_r = 2.22$ , $d = 20$ mils, $f = 8$ GHz) . . . . .	82
5.6	Measured radiation pattern of LTSA on Duroid substrate as a function of $H$ . ( $L = 12.6$ cm, $W_f = 1$ mm, $W_o = 2.2$ cm, $\epsilon_r = 2.22$ , $d = 20$ mils, $f = 8$ GHz) . . . . .	83
5.7	Geometry of rectangular plates. . . . .	85
5.8	Computed radiation pattern of antenna. . . . .	86
5.9	Measured radiation pattern of antenna. ( $L = 15$ cm, $H' = 3.75$ cm, $2\gamma = 11.5^\circ$ , $W_f = 1.3$ mm) . . . . .	87

5.10	Magnitude and Phase of current ( <i>cut-AA</i> ). . . . .	89
5.11	Magnitude and Phase of current ( <i>cut-BB</i> ). . . . .	90
5.12	Mode layout on $0.5\lambda_0 \times \lambda_0$ square conducting plate. . . . .	91
B1.	Measured radiation pattern of LTSA on thin substrate. ( $\epsilon_r = 2.22, d = 20$ mils, $L = 12.6$ cm, $2\gamma = 10^\circ, W_f = 1.5$ mm, $W_o = 2.35$ cm, $H = 7$ cm, $f = 10$ GHz) . . . . .	97
B2.	Measured radiation pattern of LTSA on thin substrate. ( $\epsilon_r = 2.22, d = 20$ mils, $L = 15.0$ cm, $2\gamma = 16^\circ, W_f = 1.5$ mm, $W_o = 4.37$ cm, $H = 10.2$ cm, $f = 8$ GHz) . . . . .	98
B3.	Measured radiation pattern of LTSA on thick substrate. ( $\epsilon_r = 2.22, d = 59$ mils, $L = 15.2$ cm, $2\gamma = 14.25^\circ, W_f = 0.5$ mm, $W_o = 3.8$ cm, $H = 12.7$ cm, $f = 12$ GHz) . . . . .	99
B4.	Measured radiation pattern of LTSA on thick substrate. ( $\epsilon_r = 2.22, d = 59$ mils, $L = 15.2$ cm, $2\gamma = 14.25^\circ, W_f = 0.5$ mm, $W_o = 3.8$ cm, $H = 12.7$ cm, $f = 8$ GHz) . . . . .	100
B5.	Measured radiation pattern of LTSA on high- $\epsilon_r$ substrate. ( $\epsilon_r = 10.5, d = 10$ mils, $L = 14.9$ cm, $2\gamma = 14^\circ, W_f = 0.5$ mm, $W_o = 3.7$ cm, $H = 12.7$ cm, $f = 8$ GHz) . . . . .	101
B6.	Measured radiation pattern of LTSA on high- $\epsilon_r$ substrate. ( $\epsilon_r = 10.5, d = 10$ mils, $L = 14.9$ cm, $2\gamma = 14^\circ, W_f = 0.5$ mm, $W_o = 3.7$ cm, $H = 12.7$ cm, $f = 10$ GHz) . . . . .	102
B7.	Measured radiation pattern of CWSA on thin substrate. ( $\epsilon_r = 2.22, d = 20$ mils, $L_f = 2.5$ cm, $L_a = 14.8$ cm, $W_f = 0.5$ mm, $W_o = 2.95$ cm, $H = 12.7$ cm, $f = 10$ GHz) . . . . .	103
B8.	Measured radiation pattern of CWSA on thin substrate. ( $\epsilon_r = 2.22, d = 20$ mils, $L_f = 2.5$ cm, $L_a = 14.8$ cm, $W_f = 0.5$ mm, $W_o = 2.95$ cm, $H = 12.7$ cm, $f = 8$ GHz) . . . . .	104
B9.	Measured radiation pattern of Vivaldi antenna. ( $L = 18.9$ cm, $W_f = 1.2$ mm, $W_o = 5.3$ cm, $H = 12.7$ cm, $f = 10$ GHz) . . . . .	105

## CHAPTER 1

### INTRODUCTION

Over the past few years there has been an increasing interest in the use of planar antennas in microwave and millimeter wave systems. The various kinds of planar antennas presently in use may be classified into broadside radiating elements and end-fire radiating elements. Resonant elements such as printed dipoles, slots, and microstrip patches all radiate in the broadside direction. The element gain for all these antennas is fairly low and does not suffice in applications where 10 dB beamwidths of the order of  $12^\circ - 60^\circ$  are required. This requirement can be readily met by using travelling wave antennas. The tapered slot antenna belongs to the class of end-fire travelling wave antennas and has several interesting applications in integrated circuitry, imaging and phased arrays.

The tapered slot antenna consists of a tapered slot cut in a thin film of metal with or without an electrically thin substrate on one side of the film. The slot is narrow towards one end for efficient coupling to devices such as mixer diodes. Away from this region, the slot is tapered and a travelling wave propagating along the slot radiates in the end-fire direction. Gibson [7] used an exponentially tapered slot antenna (he called it the Vivaldi antenna) on an alumina substrate in a 8 – 40 GHz video receiver module. Prasad and Mahapatra [24] introduced the Linearly Tapered Slot Antenna (LTSA). Their antenna was short ( $\approx \lambda_0$ ) and etched on a 25-mil alumina substrate. Korzeniowski *et al.* [20] developed an imaging array system at 94 GHz using a  $10\lambda_0$  LTSA on a 1-mil kapton substrate as an element. Yngvesson *et al.* [26] presented experimental results on Constant Width Slot Antennas (CWSAs). In all these works, it was demonstrated experimentally that the tapered

slot antenna has a very wide pattern bandwidth and has the capacity to generate a symmetric main beam despite its planar geometry. Use of these antennas has so far been based on empirical designs, as no theory was available. It is highly desirable to have a theoretical model that can predict the radiation characteristics of the antenna so as to facilitate successful designs. The successful model should be able to account for the pattern dependence on the antenna structural parameters such as the length, shape of the taper, and the dielectric substrate permittivity and thickness.

The purpose of this dissertation is to develop a theoretical model for the radiation characteristics of the tapered slot antenna. The theory presented is quite general in the sense that it is valid for any smooth taper of the slot. To validate the model, sufficient comparison with experiment is made using antennas of various lengths, taper shapes such as constant, linear and exponential, and for various substrate parameters. In the course of these comparisons, new experimental effects were observed concerning the pattern dependence on an additional parameter of the antenna and these are also presented.

Chapter 2 deals with a qualitative development of the model. The basic steps that constitute the theory and some of its salient features are described. It is shown that transmission line data on a wide uniform slot line are imperative in the development of the model. Questions as to why the antenna cannot be treated using a simpler model are addressed.

Chapter 3 presents data on the transmission line properties of a uniform wide slot line on low permittivity substrates. The eigenvalue problem for the slot wavelength and the slot electric field is solved by the spectral Galerkin's technique.



Comparison is made between the computed results and those available in the literature for high permittivity substrates. Comparison is also made with measurements. Closed form expressions for the slot wavelength and the slot line characteristic impedance are developed by curve-fitting the computed data.

In Chapter 4, theory and results are presented for the radiation pattern of the antenna. The simpler case of an air dielectric LTSA is treated first. The slot field is obtained by employing a conformal mapping. The slot field for the more general case of a dielectric supported antenna and arbitrary slot taper is obtained by affecting a stepped approximation to the continuous taper. Transmission line data on a wide uniform slot line presented in Chapter 3 are utilized in this model. In either of the above two cases, radiated fields from the tapered slot are computed by using the half-plane Green's function. Use of the half-plane Green's function rather than the free space Green's function for computing the far-fields is justified in this chapter.

Chapter 5 presents results on the newly observed effects of the pattern dependence on the lateral dimension of the antenna. Whereas the theoretical model developed in Chapter 4 adequately predicts the radiation pattern when the lateral dimension of the antenna is electrically large, the pattern exhibits some interesting features as the antenna is truncated laterally. In particular, the main beam in the E-plane is greatly narrowed, without causing much sidelobe degradation and without deteriorating the beam shape in the H-plane. Results are presented both for air dielectric and dielectric supported antennas. Studies done to treat these effects for the special case of an air dielectric LTSA are presented.

Chapter 6 forms the conclusion. Some limitations of the theoretical model developed are also discussed.

## CHAPTER 2

### METHOD OF ANALYSIS

In this chapter, a qualitative development of the theoretical model is presented. The key steps involved in the theory are summarized and the need for the model adopted is justified.

Fig. 2.1a shows the geometry of a Linearly Tapered Slot Antenna (LTSA). Metalization is present on only one side of the substrate. The antenna radiates in the end-fire direction i.e., in the negative x-direction. The radiated electric field is linearly polarized and is parallel to the plane of the slot. The antenna is usually etched on a thin and low- $\epsilon_r$  substrate and made  $3 - 10\lambda_0$  long, where  $\lambda_0$  is the free space wavelength. Well formed radiation patterns can be obtained when the lateral dimension  $H$  is electrically small or electrically large. In the ensuing analysis it is assumed that  $H$  is electrically very large and will be considered to be infinite. The method of analysis consists of two steps. In the first step, the tangential component of the electric-field distribution in the tapered slot, hereafter referred to as the aperture distribution, is obtained. In the second step, far-fields radiated by the equivalent magnetic current in the slot are obtained by using an appropriate Green's function.

The aperture distribution in the tapered slot is determined by employing the usual travelling wave antenna assumption that the aperture distribution is governed predominantly by the propagating modes corresponding to the non-terminated structure [4]. The effect of the termination of the structure at ABCD can be incorporated by adding a backward travelling wave. One recognizes that under these conditions, the problem reduces to finding the field distribution for the case

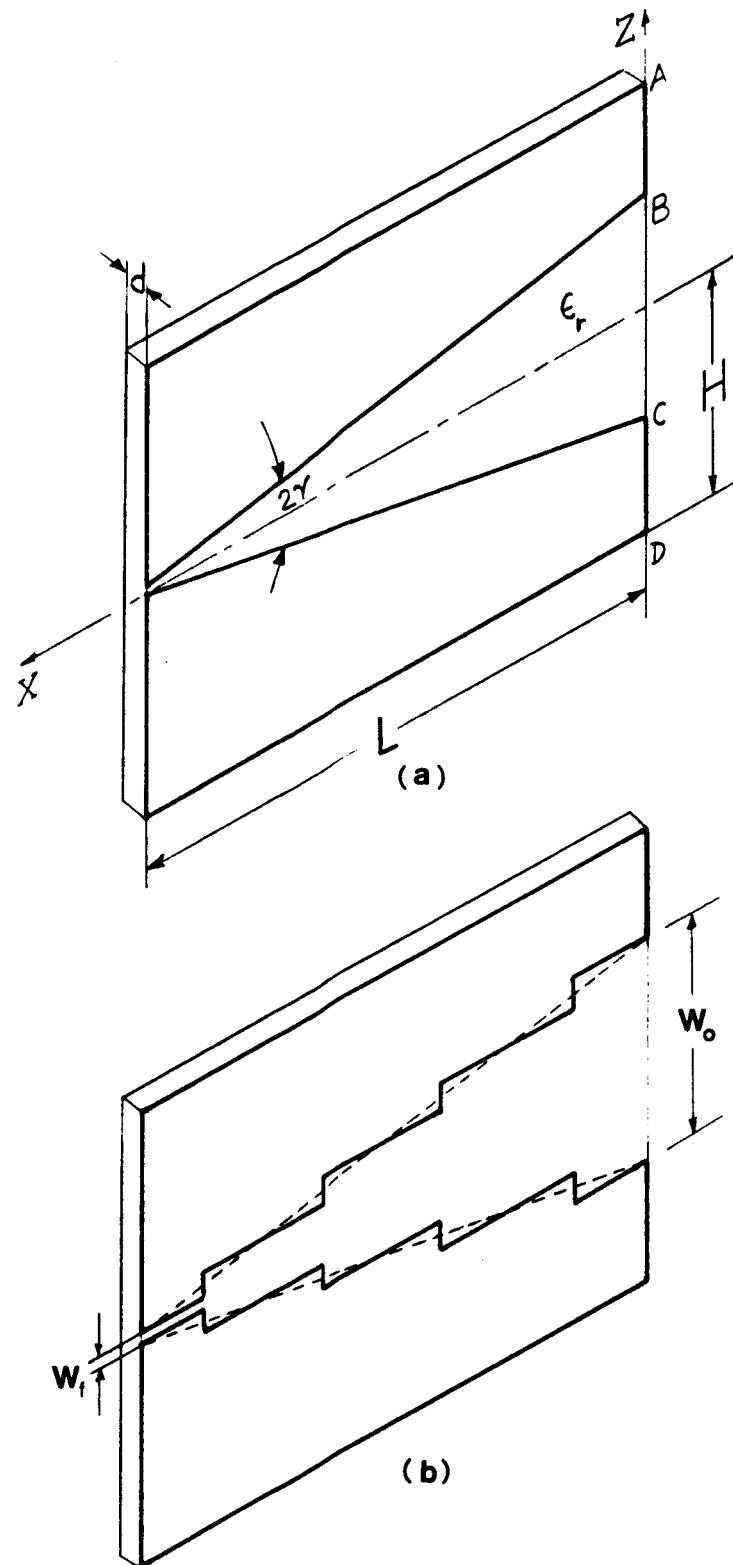


**Fig. 2.1** Geometry of LTSA. (a) Original problem (b) Stepped approximation.

of a tapered *slot line*. To accomplish this, the continuous taper is approximated by means of a number of sections of line of uniform width connected end to end. This is illustrated in Fig. 2.1b. The slot wavelength and the characteristic impedance vary from section to section in accordance with the slot width. At this stage, one may use the theory of small reflections [3] to get an estimate for the overall reflection coefficient arising from reflections from each of the step junctions and from the termination. However, for a long travelling wave antenna, the backward travelling wave on the structure does not contribute much to the front lobe. This will actually be illustrated in Chapter 4 by comparing the relative contributions due to unit strength forward and backward travelling waves on the tapered structure. Numerical studies have shown that the contribution due to the backward wave can be ignored whenever  $L \geq 3\lambda_0$ .

The aperture distribution for the stepped model is found in the following manner. Solution to the eigenvalue problem for a uniform slot line completely determines the aperture distribution in each parallel section (the slot electric field is determined up to a multiplicative constant and this is of no consequence if one were interested in a uniform slot line alone). To account for the step discontinuity, a power continuity criterion (i.e., constant power flow along the axis of the tapered line) is enforced at the step junction. This criterion relates the undetermined multiplicative constants in each section, thus yielding the field distribution in the stepped structure corresponding to a forward travelling wave on the aperture. It will be shown that data on the characteristic impedance of a wide uniform slot line are needed to enforce this criterion. The slot wavelength, the slot electric field and the characteristic impedance of a uniform wide slot line on a low permittivity substrate are obtained

in [12], and [14].

The second step in the analysis is the determination of the fields radiated by the tapered slot using the field distribution found in the first step. Termination of the aperture results in the edge ABCD in the metalization and currents are induced due to edge diffraction. These must be included in the analysis. The edge induced currents are important because the radiation pattern of a slot in an infinite ground plane (i.e., without taking the edge ABCD into account) has a null in the plane of the conductor. It is shown in Chapter 4 that the E-plane pattern is governed entirely by the edge induced currents. The prospective Green's function must be able to directly accommodate this important phenomenon. It is seen from Fig. 2.1 that the slot extends as far as the edge ABCD, thus precluding the use of far-field ray scattering theories such as GTD and UAT. This important near-field scattering is taken into account by treating the slot as radiating in the presence of a conducting half-plane (i.e., the half-plane Green's function is used).

It may also be noted that a simple analysis based on approximating the currents on the metalization as flowing along wires—similar to a V-antenna—and subsequently using the free space Green's function to find the far-fields is not satisfactory. Such a model incorrectly predicts a minimum in the end-fire direction as the flare angle  $2\gamma \rightarrow 0$  (as in a CWSA), whereas the two step procedure described above correctly predicts an end-fire main beam. The success of the latter is attributed mainly to the use of the half-plane Green's function.

Tai [25] has developed the exact theory of infinitesimal slots (both—one sided and two sided) radiating in the presence of a conducting half-plane. This half-plane Green's function is used in conjunction with the aperture distribution found in step

one to compute the far-fields radiated by each uniform section. Radiation from the entire length is determined by adding the contributions from all the sections.

## CHAPTER 3

### SLOT LINE DATA ON LOW-PERMITTIVITY SUBSTRATES

Transmission line properties of a uniform slot line shown in Fig. 3.1 have been investigated by a number of authors [2], [6], [11], and [18]. However, all the data available in the literature are on high- $\epsilon_r$  substrates and for narrow slots. In particular, the data are restricted to  $\epsilon_r \geq 9.6$ ,  $W/d < 2$ ,  $d/\lambda_0 \geq 0.02$ , where  $\lambda_0$  is the free-space wavelength. For use as an antenna, the slot is very wide, typically approaching one free-space wavelength and the antenna is usually built on a low- $\epsilon_r$  substrate. It is desirable to know the transmission line properties of wide slot lines on low- $\epsilon_r$  substrates. In this chapter, theoretical and experimental results are presented for the slot wavelength  $\lambda'$  and the characteristic impedance  $Z_0$  of a wide uniform slot line on low- $\epsilon_r$  substrates. The problem is formulated in the spectral domain and solved by the spectral Galerkin technique. Comparison is made between the computed results and those available in the literature for high- $\epsilon_r$  substrates. Comparison for the slot wavelength is also made with measurements. Closed form expressions are developed for  $\lambda'$  and  $Z_0$ . Material presented in this chapter is published in [12] and [14] and has a direct bearing in the development of the theoretical model for the slot antenna. The formulation of a slot line using the spectral Galerkin's technique is not new but is included here for the sake of completeness.

#### 3.1 Formulation of the Problem

Fig. 3.1 shows the geometry of a uniform slot line. The objective is to solve for  $\lambda'$  and  $Z_0$  for the dominant mode on the line. Using the generalized spectral domain immittance approach [10], expressions are obtained for the two dimensional Green's

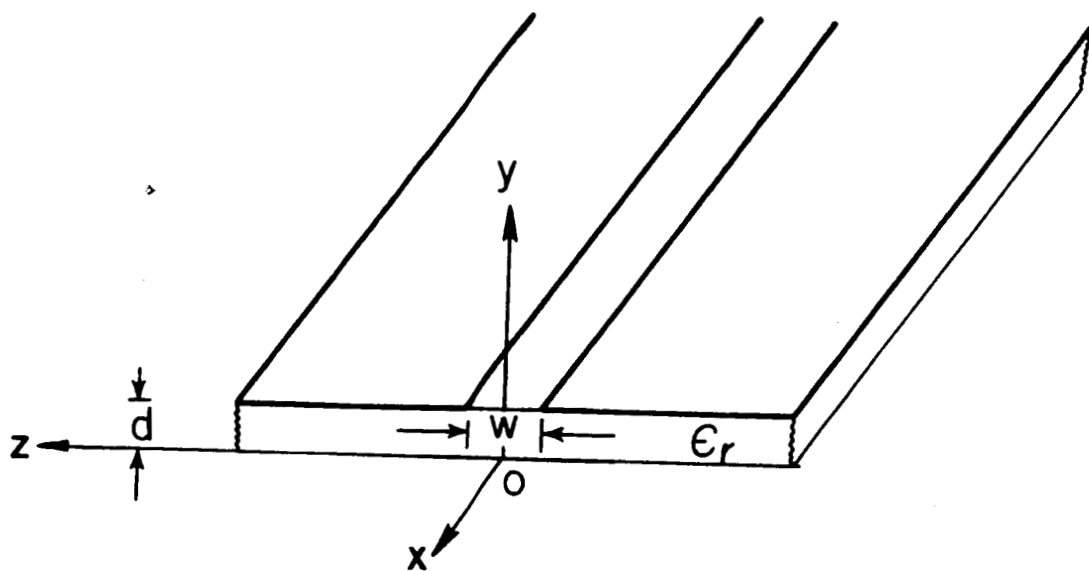


Fig. 3.1 Geometry of slot line.



dyadic. This Green's dyadic relates the slot electric field to the *total* surface current that resides on the slot-side of the air-dielectric interface. The unknown transverse and longitudinal slot fields are expanded in a set of basis functions and Galerkin's testing procedure employed. Parseval's theorem is invoked to finally result in a matrix eigenvalue problem. The eigensolution of this system completely determines  $\lambda'$  and  $Z_0$ .

**1. Slot Wavelength.** The foregoing procedure leads to [12]

$$\begin{pmatrix} \mathbf{P} & \mathbf{Q} \\ \mathbf{R} & \mathbf{S} \end{pmatrix} \begin{pmatrix} a_1 \\ \vdots \\ a_{M_s} \\ b_1 \\ \vdots \\ b_{M_s} \end{pmatrix} = \begin{pmatrix} 0 \\ \vdots \\ 0 \\ 0 \\ \vdots \\ 0 \end{pmatrix} \quad (3.1)$$

where the elements of the submatrices P, Q, R and S are given by

$$P_{mn} = \int_{-\infty}^{+\infty} \tilde{Y}_{zz} \tilde{e}_m^z \tilde{e}_n^z d\alpha \quad (3.2a)$$

$$Q_{mn} = R_{nm} = \int_{-\infty}^{+\infty} \tilde{Y}_{zz} \tilde{e}_m^z \tilde{e}_n^z d\alpha \quad (3.2b)$$

$$S_{mn} = \int_{-\infty}^{+\infty} \tilde{Y}_{zz} \tilde{e}_m^z \tilde{e}_n^z d\alpha \quad (3.2c)$$

and the elements of the Green's dyadic are given by

$$Y_{zz} = \frac{1}{j\omega\mu_0\gamma_1 T^e T^m} \left[ (T^e - 1)(\gamma_1 + T^m)[2k_z^2 - k_0^2(\epsilon_r + 1)] + (k_z^2 - k_0^2) \right]$$

$$Y_{zz} = Y_{zz} = \frac{\alpha k_z}{j\omega\mu_0\gamma_1 T^e T^m} \left[ \frac{2\epsilon_r\gamma_1 + X_0 d\{2(\epsilon_r + 1)\gamma_1^2 - k_0^2(\epsilon_r - 1)\}}{+ \gamma_1(X_0 d)^2\{2\gamma_2^2 + \epsilon_r(\epsilon_r - 1)k_0^2\}} \right]$$

$$Y_{zz} = \frac{1}{j\omega\mu_0\gamma_1 T^e T^m} \left[ (T^e - 1)(\gamma_1 + T^m)[2\alpha^2 - k_0^2(\epsilon_r + 1)] + (\alpha^2 - k_0^2) \right]$$

where  $k_0 = \omega\sqrt{\mu_0\epsilon_0}$  is the free space wavenumber and  $\gamma_1$  and  $\gamma_2$  are the y-directed propagation constants in air and the dielectric slab respectively, and

$$\alpha^2 + k_z^2 = \gamma_1^2 + k_0^2 = \gamma_2^2 + \epsilon_r k_0^2$$

$$X_0 = \tanh(\gamma_2 d) / (\gamma_2 d)$$

$$T^e = 1 + \frac{\gamma_1}{\gamma_2} \tanh(\gamma_2 d)$$

$$T^m = \epsilon_r \gamma_1 + \gamma_2 \tanh(\gamma_2 d)$$

and it has been assumed that the slot field is expanded as

$$E_z^s = \sum_{n=1}^{M_s} a_n e_n^z \quad E_z^s = \sum_{n=1}^{M_s} b_n e_n^z \quad (3.3)$$

A tilde in the above expressions denotes quantities Fourier transformed with respect to  $z$  and the superscript  $s$  stands for slot.  $\alpha$  is the transform variable. The elements of the coefficient matrix are all functions of the slot wavelength  $\lambda'$ . The dispersion relation is obtained by solving for values of  $\lambda'$  that render the determinant of the coefficient matrix to zero at a particular frequency,  $d$ ,  $W$  and  $\epsilon_r$ . The corresponding eigenvector determines the unknowns in the expansion (up to a multiplicative constant).

**2. Characteristic Impedance.** The characteristic impedance  $Z_0$  of the slot line is defined as [18]

$$Z_0 = \frac{|V_0|^2}{P_f} \quad (3.4)$$

where  $V_0$  is the voltage across the slot at  $y = d$  and given by

$$V_0 = \int_{-W/2}^{+W/2} E_z^s dz = \tilde{E}_z(\alpha)|_{\alpha=0} = \tilde{E}_z(0) \quad (3.5)$$

$P_f$  is the real part of the complex power flow along the line and is given by

$$P_f = \iint_{yz} (E_y H_z^* - E_z H_y^*) dx dy = \frac{1}{2\pi} \iint_{y\alpha} (\tilde{E}_y \tilde{H}_z^* - \tilde{E}_z \tilde{H}_y^*) d\alpha dy \quad (3.6)$$

The second equality in (3.6) follows from Parseval's theorem. The fields  $\tilde{E}$ ,  $\tilde{H}$  in the spectral domain pertaining to the air and dielectric regions can be expressed in terms of the slot field  $E_x^s$ ,  $E_z^s$  defined in (3.3).

### 3.2. Numerical Results and Discussion

The basis functions employed in all the computations are

$$e_n^z(z) = \left( \frac{2}{\pi W} \right) \frac{T_{2(n-1)}\left(\frac{2z}{W}\right)}{\sqrt{1 - \left(\frac{2z}{W}\right)^2}}, \quad n = 1, 2, \dots \quad (3.7a)$$

$$e_n^x(z) = \left( \frac{2}{\pi W} \right) \sqrt{1 - \left(\frac{2z}{W}\right)^2} U_{(2n-1)}\left(\frac{2z}{W}\right), \quad n = 1, 2, \dots \quad (3.7b)$$

where,  $T_n(\cdot)$  and  $U_n(\cdot)$  are Tchebycheff polynomials of the first and second kind respectively.

The longitudinal (x-directed) component is an odd function of  $z$ , whereas the transverse (z-directed) component is an even function of  $z$ , which is the field configuration for the dominant mode on the line. Also, the basis functions chosen satisfy the proper edge conditions.

The Fourier transforms of the basis functions in (3.7) are readily found in a closed form as [5]

$$\tilde{e}_n^z(\alpha W) = (-1)^{n+1} J_{2(n-1)}\left(\frac{\alpha W}{2}\right) \quad (3.8a)$$

$$\tilde{e}_n^x(\alpha W) = j(-1)^{n+1} 2n \frac{J_{2n}\left(\frac{\alpha W}{2}\right)}{\left(\frac{\alpha W}{2}\right)} \quad (3.8b)$$

The integrals in (3.2) must be evaluated numerically. However, the choice of basis functions in (3.7) facilitates the extraction of the asymptotic contribution of

the integrands and converts them to rapidly converging ones suitable for efficient numerical computation. For computing  $Z_0$  the integration with respect to  $y$  in (3.6) can be carried out in a closed form. However, the integration on the  $\alpha$  variable must be done numerically. The integrands in this case decay (asymptotically) twice as fast as those in (3.2) and can be evaluated easily without asymptotic extraction.

The slot wavelength  $\lambda'$  is stationary with respect to the slot field and it was found that the  $\lambda'$  converges with only one basis function for  $E_z^s$ . However, more than one basis function is needed for the convergence of  $Z_0$ . The maximum number of basis functions needed for  $E_z^s$  and  $E_x^s$  during the computation of  $Z_0$  was 3 and 5 respectively, when the slot width approached one free space wavelength.

Computer programs were developed to compute  $\lambda'$  and  $Z_0$  for a specified  $\epsilon_r$ ,  $\lambda_0$  and  $d$ . Table 3.1 shows the comparison between the present computations and those in [11] for  $\epsilon_r = 20$ ,  $d = 0.348$  cm and  $W = 0.0635$  cm. It is seen that the two agree well within 1%. Also, the results in [11] have been reported to be within 1% of those presented in [21]. Table 3.2 shows the comparison between the computations and measurements done here. The slot wavelength was measured using the scheme suggested in [2]. Experiments were performed both on a narrow slot and on a wide slot. The agreement is generally within 2%. It may be noted, however, that the computed slot wavelength is always greater than the measured value. Measurements performed on yet another substrate (RT/Duroid 5880) indicated the same. This slight discrepancy is found in narrow slot as well as in wide slots. Some studies were made to ascertain this systematic discrepancy. The prime suspect was the presence of a thin layer of adhesive between the metal and dielectric substrate. If the dielectric constant of the adhesive were higher than that of the substrate, it

**TABLE 3.1**  
COMPARISON OF COMPUTED SLOT WAVELENGTH

Frequency (GHz)	$\lambda'/\lambda_0$		% Error
	Itoh [11]	Present	
1	0.368	0.367	-0.40
2	0.344	0.341	-0.27
3	0.330	0.328	-0.60
4	0.319	0.317	-0.40
5	0.308	0.308	-0.07
6	0.299	0.298	-0.20

$\epsilon_r = 20$ ,  $d = 0.348$  cm,  $W = 0.0635$  cm

**TABLE 3.2**  
COMPARISON OF COMPUTED AND MEASURED SLOT WAVELENGTH

$W/d$	Frequency (GHz)	Measured $\lambda'/\lambda_0$	Computed $\lambda'/\lambda_0$	% Error
1.34	2.0	0.873	0.889	+1.39
	2.5	0.866	0.883	+1.50
	3.0	0.862	0.879	+1.90
	3.5	0.852	0.875	+2.00
	4.0	0.867	0.871	+0.39
10.71	2.0	0.933	0.958	+2.64
	3.0	0.945	0.951	+0.66
	4.0	0.929	0.943	+1.50
	5.0	0.922	0.939	+1.89
	6.0	0.916	0.933	+1.80

$\epsilon_r = 2.55$ ,  $d = 1.57$  mm (0.062 in)

could result in a somewhat smaller measured wavelength. Perturbation analysis similar to the one used in [17] was performed so as to quantify this effect. An expression for the wavelength correction  $\Delta\lambda'/\lambda'$  is given in Appendix A. Table 3.3 shows the correction due to the presence of an adhesive with a normalized thickness  $t/d$  of 0.02. Results are shown for two different substrates. The influence of the adhesive on  $\lambda'$  diminishes as the slot width is increased. Also, the correction in the slot wavelength is insignificant even for narrow slots, when a lower  $\epsilon_r$  substrate is used. It was concluded that the presence of a thin layer of adhesive does not account for the 2% discrepancy. Other factors such as the thickness of the metal tend to increase the slot wavelength [16] and were not pursued.

Table 3.4 shows the agreement of the characteristic impedance between the present computations and those in [21]. Figs. 3.2–3.5 illustrate the typical variation of  $\lambda'$  and  $Z_0$  with slot width  $W$ . Curves are presented for  $\epsilon_r = 2.22$  and for  $\epsilon_r = 9.8$ .

### 3.3. Closed Form Expressions for $\lambda'$ and $Z_0$

Empirical formulas have been developed for the normalized slot wavelength  $\lambda'/\lambda_0$  and the characteristic impedance  $Z_0$ . These formulas have been obtained by least-square curve-fitting the computed data. In each case, the average of the absolute percentage error 'Av' and the maximum percentage error 'Max' observed in a nonrandom sample of 120 data points is presented. Also, where possible, the region around which the maximum error has been observed is indicated.

The following formulas are all valid within  $0.006 \leq d/\lambda_0 \leq 0.06$ .

$$2.22 \leq \epsilon_r \leq 3.8$$

$$0.0015 \leq W/\lambda_o \leq 0.075$$

$$\begin{aligned} \lambda'/\lambda_o = & 1.045 - 0.365 \ln \epsilon_r + \frac{6.3(W/d)\epsilon_r^{0.945}}{(238.64 + 100W/d)} \\ & - \left[ 0.148 - \frac{8.81(\epsilon_r + 0.95)}{100\epsilon_r} \right] \ln(d/\lambda_o) \end{aligned} \quad (3.9)$$

Av = 0.37 %, Max = 2.2 % (at one point).

$$\begin{aligned} Z_o = & 60 + 3.69 \sin \left[ \frac{(\epsilon_r - 2.22)\pi}{2.36} \right] + 133.5 \ln(10\epsilon_r) \sqrt{W/\lambda_o} \\ & + 2.81 [1 - 0.011\epsilon_r(4.48 + \ln \epsilon_r)] (W/d) \ln(100d/\lambda_o) \\ & + 131.1(1.028 - \ln \epsilon_r) \sqrt{(d/\lambda_o)} \\ & + 12.48(1 + 0.18 \ln \epsilon_r) \frac{W/d}{\sqrt{\epsilon_r - 2.06 + 0.85(W/d)^2}} \end{aligned} \quad (3.10)$$

Av = 0.67 %, Max = 2.7 % (at one point).

$$0.075 \leq W/\lambda_o \leq 1.0$$

$$\begin{aligned} \lambda'/\lambda_o = & 1.194 - 0.24 \ln \epsilon_r - \frac{0.621\epsilon_r^{0.835}(W/\lambda_o)^{0.48}}{(1.344 + W/d)} \\ & - 0.0617 \left[ 1.91 - \frac{(\epsilon_r + 2)}{\epsilon_r} \right] \ln(d/\lambda_o) \end{aligned} \quad (3.11)$$

Av = 0.69 %, Max = -2.6 % (at two points, for  $W/\lambda_o > 0.8$ ).

$$\begin{aligned} Z_o = & 133 + 10.34(\epsilon_r - 1.8)^2 + 2.87 [2.96 + (\epsilon_r - 1.582)^2] \\ & \left[ \{W/d + 2.32\epsilon_r - 0.56\} \{ (32.5 - 6.67\epsilon_r)(100d/\lambda_o)^2 - 1 \} \right]^{\frac{1}{2}} \\ & - (684.45(d/\lambda_o))(\epsilon_r + 1.35)^2 + 13.23\{(\epsilon_r - 1.722)W/\lambda_o\}^2 \end{aligned} \quad (3.12)$$

$A_v = 1.9\%$ ,  $|\text{Max}| = 5.4\%$  (at three points, for  $W/\lambda_o > 0.8$ ).

$$3.8 \leq \epsilon_r \leq 9.8$$

$$0.0015 \leq W/\lambda_o \leq 0.075$$

$$\begin{aligned} \lambda'/\lambda_o = & 0.9217 - 0.277 \ln \epsilon_r + 0.0322(W/d) \left[ \frac{\epsilon_r}{(W/d + 0.435)} \right]^{\frac{1}{2}} \\ & - 0.01 \ln (d/\lambda_o) \left[ 4.6 - \frac{3.65}{\epsilon_r^2 \sqrt{W/\lambda_o} (9.06 - 100W/\lambda_o)} \right] \end{aligned} \quad (3.13)$$

$A_v = 0.6\%$ ,  $|\text{Max}| = 3\%$  (at three points, for  $W/d > 1$ , and  $\epsilon_r > 6.0$ ).

$$\begin{aligned} Z_o = & 73.6 - 2.15\epsilon_r + (638.9 - 31.37\epsilon_r)(W/\lambda_o)^{0.6} + \left( 36.23\sqrt{\epsilon_r^2 + 41} - 225 \right) \\ & \frac{W/d}{(W/d + 0.876\epsilon_r - 2)} + 0.51(\epsilon_r + 2.12)(W/d) \ln (100d/\lambda_o) \\ & - 0.753\epsilon_r(d/\lambda_o)/\sqrt{W/\lambda_o} \end{aligned} \quad (3.14)$$

$A_v = 1.58\%$ ,  $\text{Max} = 5.4\%$ , (at three points, for  $W/d > 1.67$ ).

$$0.075 \leq W/\lambda_o \leq 1.0$$

$$\begin{aligned} \lambda'/\lambda_o = & 1.05 - 0.04\epsilon_r + 1.411 \left[ \frac{\epsilon_r - 1.421}{100} \right] \ln \{W/d - 2(1 - 0.146\epsilon_r)\} \\ & + 0.111(1 - 0.366\epsilon_r)\sqrt{W/\lambda_o} \\ & + 0.139\{1 + 0.52\epsilon_r(14.7 - \epsilon_r)\}(d/\lambda_o) \ln (d/\lambda_o) \end{aligned} \quad (3.15)$$

$A_v = 0.75\%$ ,  $|\text{Max}| = 3.2\%$  (at two points, for  $W/\lambda_o = 0.075$ ,  $(d/\lambda_o) > 0.03$ ).

$$\begin{aligned} Z_o = & 120.75 - 3.74\epsilon_r + 50 \left[ \tan^{-1}(2\epsilon_r) - 0.8 \right] (W/d) \left[ 1.11 + 0.132 \frac{(\epsilon_r - 27.7)}{(100d/\lambda_o + 8)} \right] \\ & \ln \left[ (100d/\lambda_o) + \sqrt{(100d/\lambda_o)^2 + 1} \right] \\ & + 14.21(1 - 0.458\epsilon_r)(W/\lambda_o + 0.33)^2 \{ (100d/\lambda_o) + 5.1 \ln \epsilon_r - 13.1 \} \end{aligned} \quad (3.16)$$

$A_v = 2.0\%$ ,  $|\text{Max}| = 5.8\%$  (at two points, for  $W/\lambda_o < 0.1$ ). In the above expression,  $\tan^{-1}(\cdot)$  assumes its principal value.



**TABLE 3.3**  
EFFECT OF ADHESIVE ON SLOT WAVELENGTH

$\epsilon_r^s$	$W/d$	$d/\lambda_0$	$\lambda'/\lambda_0$	$Z_0 (\Omega)$	$\epsilon_r^a$	$\Delta\lambda'/\lambda'$
20.00	0.69	0.020	0.373	82.3	3.25	$+4.20 \times 10^{-2}$
2.55	1.34	0.016	0.879	135.0	4.00	$-0.99 \times 10^{-2}$
2.55	10.71	0.010	0.958	200.0	4.00	$-1.75 \times 10^{-3}$

$t/d = 0.02$ , \* (the superscripts *s* and *a* denote substrate and adhesive respectively)

**TABLE 3.4**  
COMPARISON OF COMPUTED CHARACTERISTIC IMPEDANCE

$\epsilon_r$	$d/\lambda_0$	$W/d$	$Z_0 (\Omega)$	
			Mariani [21]	Present
9.6	0.060	1.0	140	142
11.0	0.040	1.5	160	160
13.0	0.030	0.4	80	82
16.0	0.025	2.0	150	151
20.0	0.030	1.0	100	101

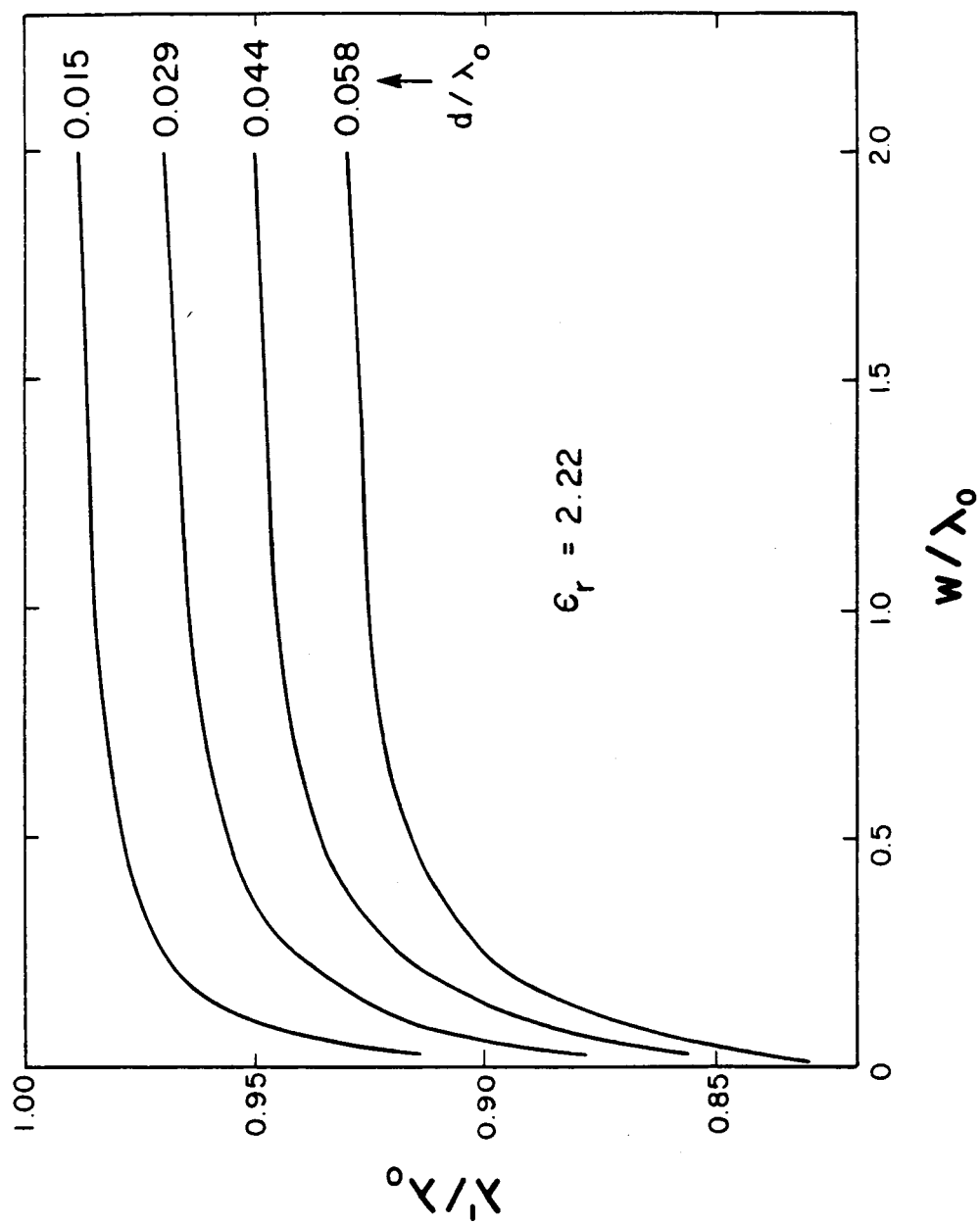


**Fig. 3.2** Normalized slot wavelength versus slot width.

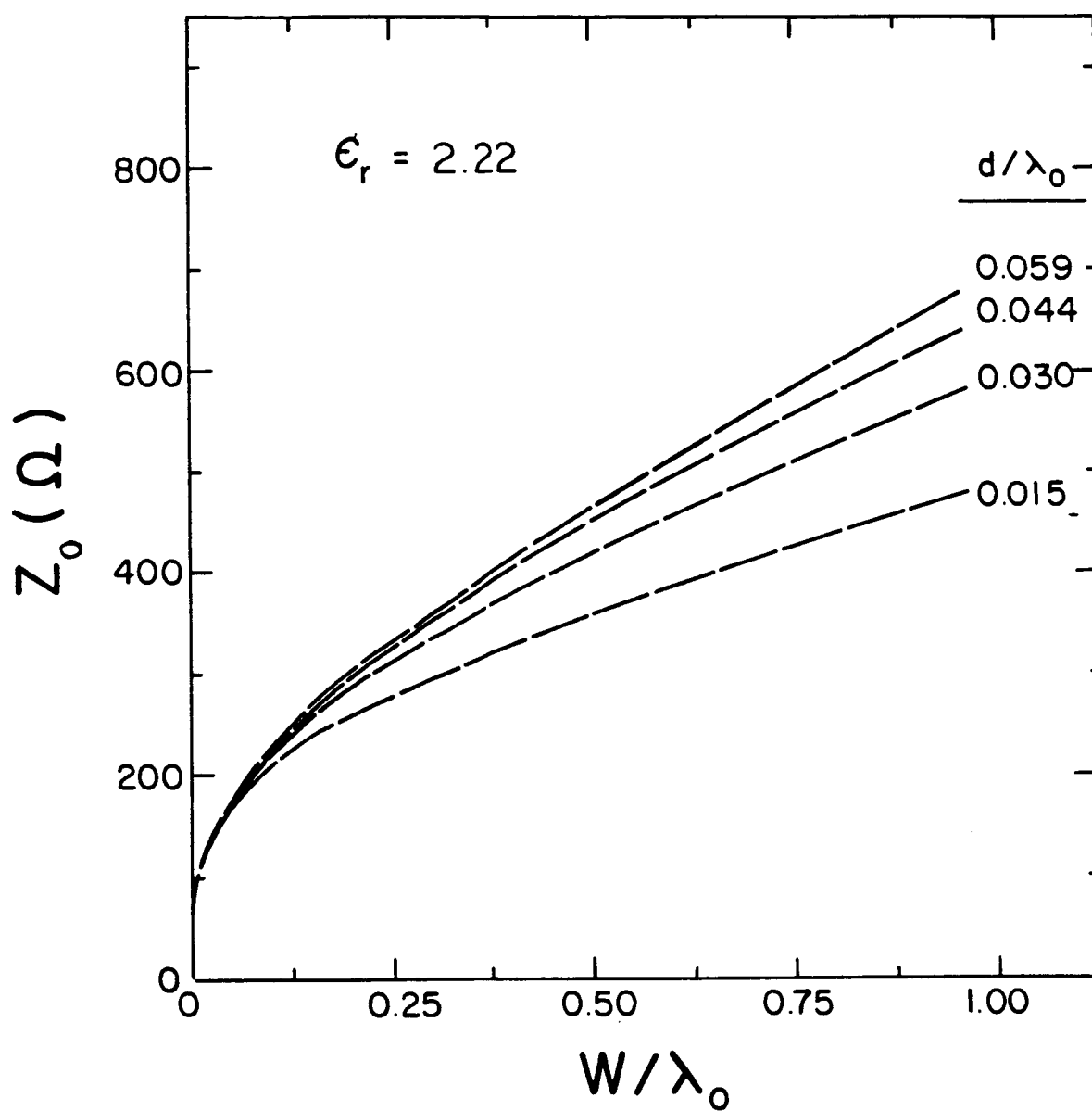


Fig. 3.3 Characteristic impedance of slot line versus slot width.

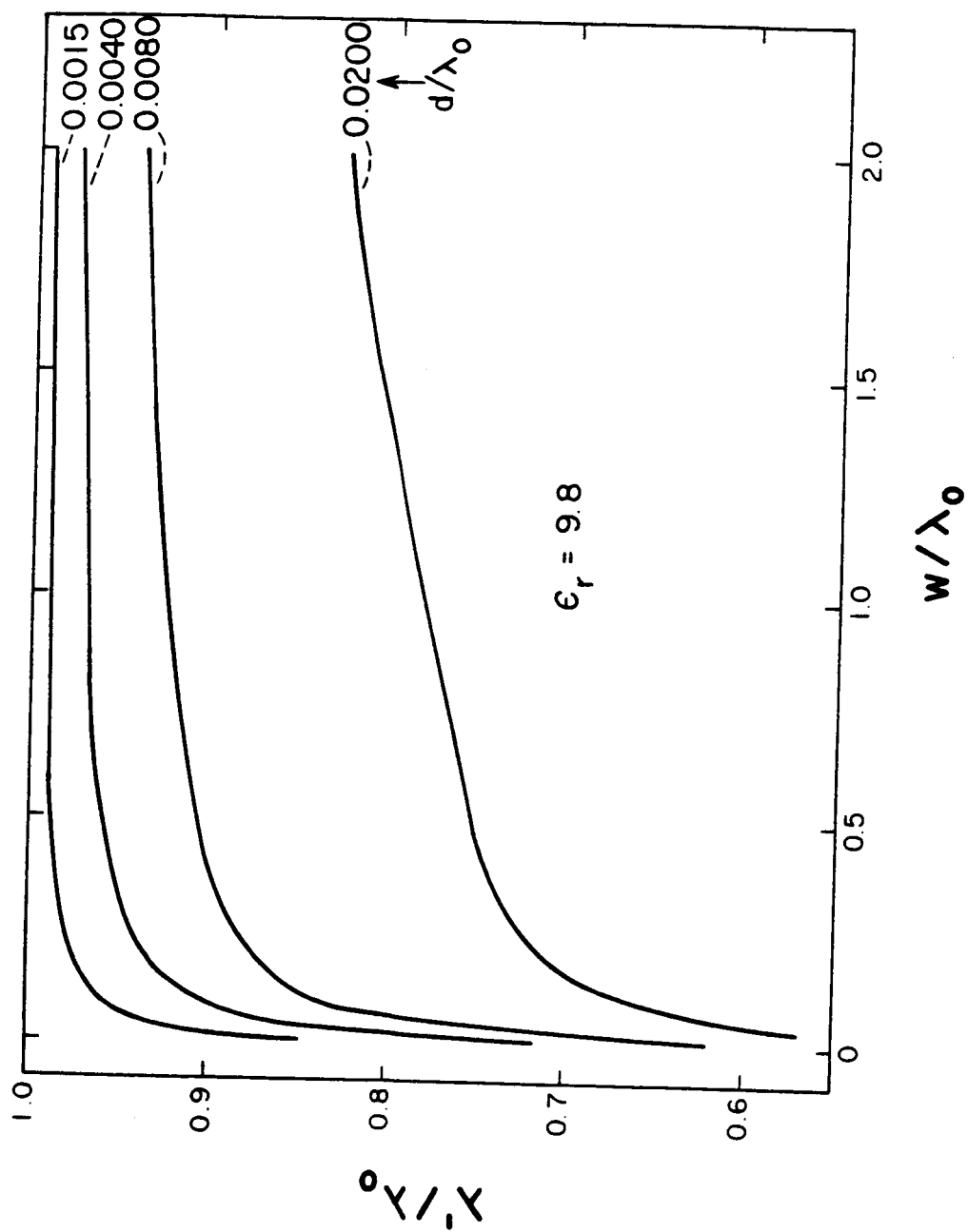


Fig. 3.4 Normalized slot wavelength versus slot width.

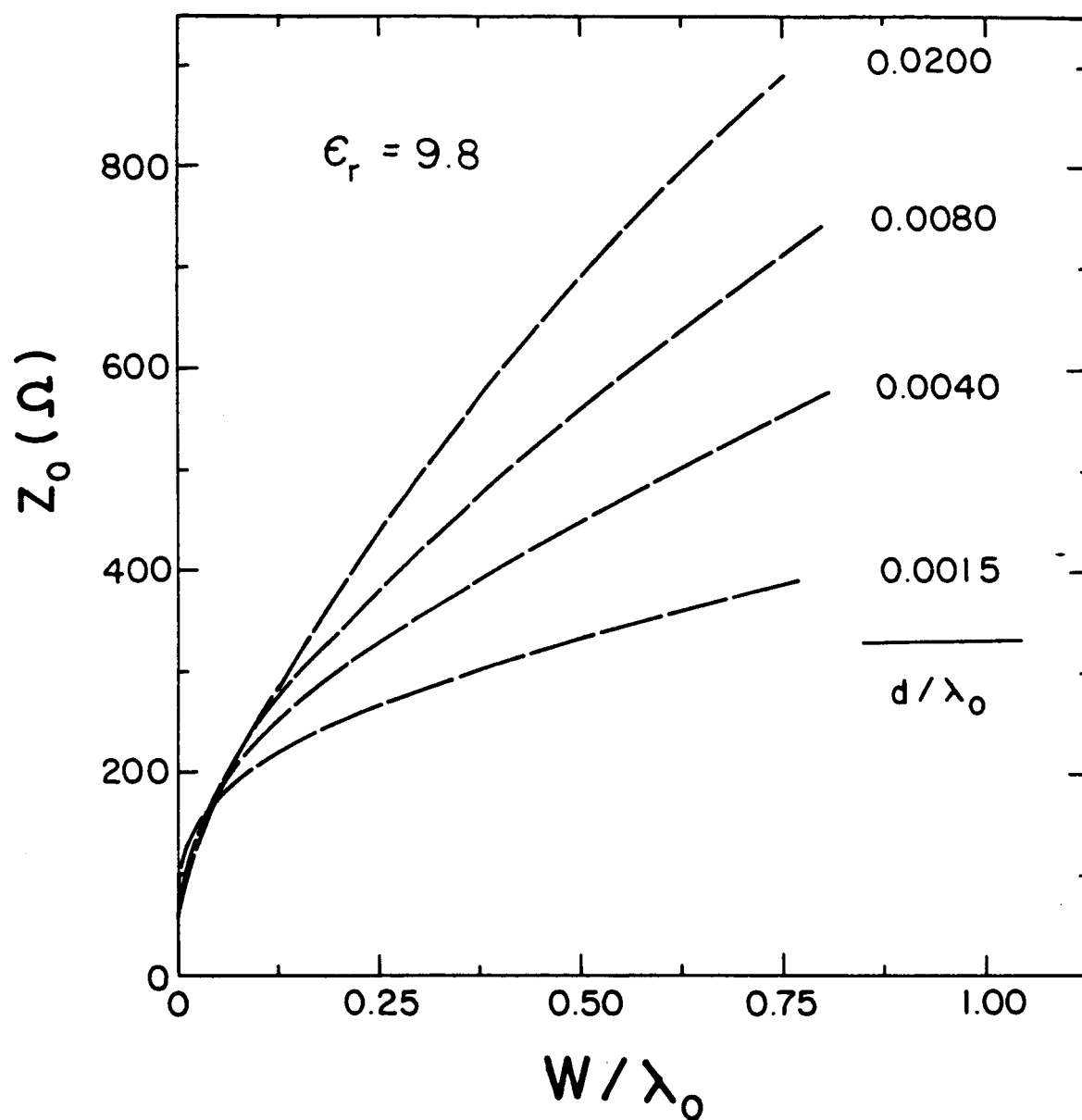


Fig. 3.5 Characteristic impedance of slot line versus slot width.

## CHAPTER 4

### FAR-FIELDS OF THE ANTENNA

In this chapter theory and results for the far-fields of the tapered slot antenna are presented. The simpler case of an air dielectric LTSA (TEM-LTSA) is treated first and presented in section 4.1. The TEM-LTSA is simpler and direct to treat analytically but will nevertheless shed light on the basic physics governing the radiation mechanism of the tapered slot antenna. Furthermore, it forms the basis of analysis and will serve as a check for the more general case of dielectric supported antennas ( $\epsilon_r > 1$ ). The aperture distribution for this general case is developed in section 4.2 via the stepped approximation. Basic steps leading to the development of the model are presented and expressions for the far-fields of the antenna are given. In section 4.3 comparison is shown between the computed and measured results. Numerous cases are considered to demonstrate the versatility of the theoretical model in treating an arbitrary taper. In particular, results are presented for the case of a constant taper (the CWSA), linear taper (the LTSA) and the exponential taper (the Vivaldi). Results are presented both for the case of a thin substrate and a thick substrate.

#### 4.1. TEM-LTSA

A detailed account of the mathematical derivation of the aperture distribution and the far-fields of a TEM-LTSA is published in [15]. Only the important steps relevant to understanding of the problem will be presented here.

1. **Formulation.** As discussed in Chapter 2, the aperture distribution for the antenna can be determined approximately by solving the non-terminated version of the antenna structure. For the special case of air dielectric and a linear taper, the

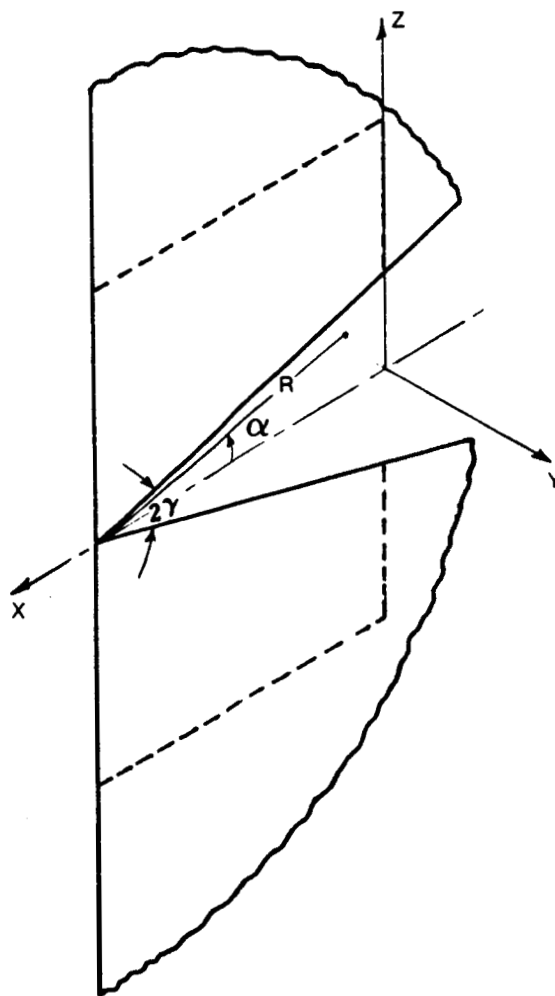


**Fig. 4.1** Geometry of coplanar bifin structure.

structure is reduced to a pair of coplanar fins as shown in Fig. 4.1. A pair of infinite cones in a homogeneous medium supports a TEM wave and the wave equation can be solved exactly by employing a conformal mapping [1]. It is shown in [15] that the x- and z-directed components of the slot electric field are given approximately as

$$E_z^s \approx \frac{e^{-jk_0 R}}{R} \frac{\sin \alpha}{\sqrt{\tan^2(\frac{\gamma}{2}) - \tan^2(\frac{\alpha}{2})}} \quad (4.1)$$

$$E_x^s \approx \frac{e^{-jk_0 R}}{R} \frac{\cos \alpha}{\sqrt{\tan^2(\frac{\gamma}{2}) - \tan^2(\frac{\alpha}{2})}} \quad (4.2)$$

where  $(R, \alpha)$  are the polar coordinates in the plane of the slot as shown in Fig. 4.1 and  $2\gamma$  is the flare angle of the LTSA.

The equivalent magnetic currents in the slot are proportional to (4.1) and (4.2) and radiate in the presence of a conducting half-plane as described in Chapter 2. This half-plane Green's function rigorously accounts for the near-field scattering by the edge ABCD. It can be shown from the analysis of infinitesimal slots radiating in the presence of a conducting half-plane that the longitudinal slot field  $E_z^s$  does not contribute to the far-field in either principal plane. This may be explained physically as follows. The far-field component at any observation point is composed of two terms—a term involving the incident field i.e., field in the absence of the edge ABCD and a second term, the scattered field, that arises as a result of induced currents on the metal due to the presence of the edge ABCD. Both the incident field and the scattered field arising out of  $E_z^s$  are perpendicular to the  $xz$ -plane and contribute only to the cross-polarized component. Hence, only field due to  $E_x^s$  is needed as far as the copolar component is concerned. The far-field  $e_\theta(\theta, \phi)$  due to an x-directed two sided infinitesimal slot (that supports  $E_x^s$ ) located at  $(x', y')$  on a conducting



half-plane is given by [15] (suppressing the constants)

$$e_\theta(\theta, \phi) = |\sin \phi| e^{j\pi/4} F(v) e^{+jk_0(x' \sin \theta \cos \phi + z' \cos \theta)} + \frac{\sin\left(\frac{\phi}{2}\right) e^{-j[\pi/4 + k_0(x' \sin \theta - z' \cos \theta)]}}{\sqrt{\pi k_0 x' \sin \theta}} \quad (4.3)$$

where  $v = k_0 x' \sin \theta (1 + \cos \phi)$  and  $F(\cdot)$  is the Fresnel integral defined by

$$F(v) = \int_0^v \frac{e^{-jt}}{\sqrt{2\pi t}} dt \quad (4.4)$$

It may be noted that as the slot is receded away from the edge,  $k_0 x' \rightarrow \infty$  and  $e^{j\pi/4} F(v) \rightarrow 1/\sqrt{2}$ . The second term in (4.3) decays to zero and  $e_\theta$  is dominated by the first term. Further, the first term reduces to the familiar far-field expression for a slot in an infinite ground plane (except for an insignificant constant phase factor). Consequently, the first term may be labelled the 'incident field' and the second term the 'scattered field'. The scattered field is particularly significant for small  $k_0 x'$ . In the E-plane,  $\phi = \pi$  and it is seen from (4.3) that the incident field is identically zero, as expected. The far-field in the E-plane is governed entirely by the scattered field. In contrast to the free-space Green's function, the half-plane Green's function correctly predicts a nonzero field in the E-plane.

The far-zone pattern  $E_\theta$  of the LTSA is obtained by integrating (4.2) over the tapered slot region with (4.3) as a kernel. It is shown in [15] that for small flare angles  $2\gamma$ , the resulting two dimensional integral may be reduced to a one dimensional one. The result is

$$E_\theta(\theta, \phi) \approx \sin \phi \int_{-\gamma}^{+\gamma} \frac{\cos \alpha}{\sqrt{\tan^2\left(\frac{\gamma}{2}\right) - \tan^2\left(\frac{\alpha}{2}\right)}} \frac{1}{v_1} \left[ F(v_2) - e^{-jv_1} F\{v_2(1 - \cos \alpha)\} + \sqrt{\frac{v_3}{v_2}} e^{-jv_1 \sec \alpha} \{F^*(v_3) - F^*(v_3(1 - \cos \alpha))\} \right] d\alpha \quad (4.5)$$

where  $v_1 = k_0 L (1 + \sin \theta \cos \phi \cos \alpha - \cos \theta \sin \theta)$ ,  $v_2 = k_0 L \sin \theta (1 + \cos \phi)$  and  $v_3 = k_0 L \sec \alpha \{1 - \sin(\theta + \alpha)\}$  and the superscript \* denotes complex conjugation.

**2. Numerical Results and Discussion.** The integral in (4.5) must be evaluated numerically. The singularity in the integrand as  $\alpha \rightarrow \pm\gamma$  is integrable and poses no problem in the numerical integration. Radiation patterns for the LTSA have been computed for lengths  $L/\lambda_0$  varying between 3 and 10 and for flare angles  $2\gamma$  ranging between  $8^\circ$  and  $21^\circ$ .

The aperture distribution given in (4.2) includes only a forward travelling wave that would propagate freely on a non-terminated structure. Termination of the structure at ABCD may result in a backward travelling wave. However, the inclusion of a backward travelling wave on the aperture has been found to have a minimal effect on the front lobe of the pattern for a sufficiently long antenna ( $L/\lambda_0 \geq 3$ ). To illustrate this, computed patterns due to unit strength forward and backward waves on the aperture of a  $5\lambda_0$  long LTSA with  $2\gamma = 10^\circ$  are plotted in Fig. 4.2. It is seen that the contribution of the backward wave in the forward half space ( $x < 0$ ) is not very significant. Also, the effect of the backward wave is much less severe in the E-plane than in the H-plane. This is because of the nonzero aperture width in the E-plane that introduces an additional factor in the pattern similar to the space factor of an aperture antenna. This factor is responsible for the decay of the backward wave contribution away from the end-fire direction. There is no such aperture effect in the H-plane. The backward wave contribution diminishes as the length of the antenna is increased. In all the subsequent computations, only the forward travelling wave as given in (4.2) is assumed for the aperture distribution.

The computed pattern in the E- and H-planes for a  $6.3\lambda_0$  long antenna with

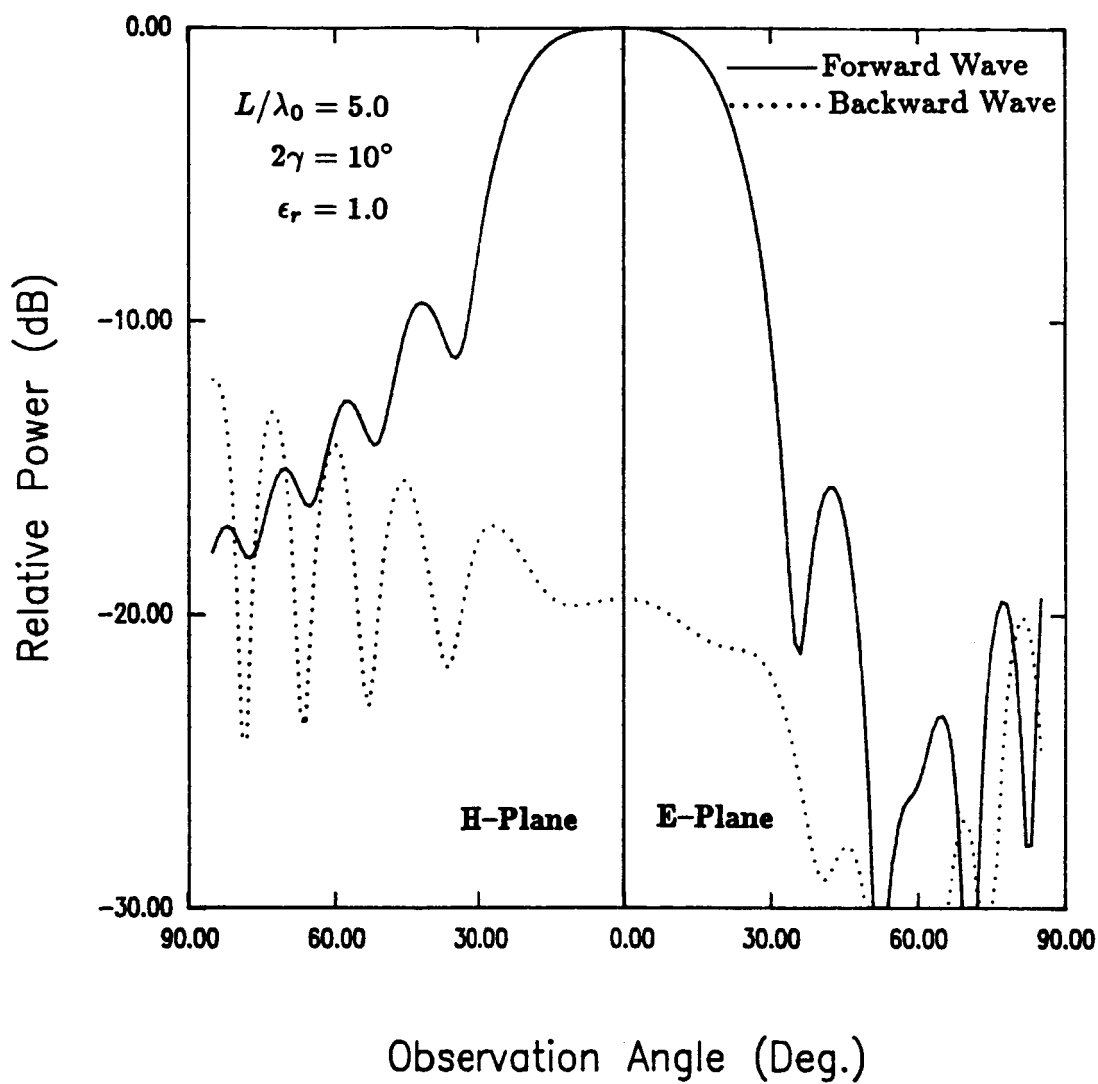


**Fig. 4.2** Radiation patterns—relative contributions of forward and backward waves.

$2\gamma = 15^\circ$  is shown in Fig. 4.3. Corresponding experimental patterns are also plotted on the same figure. The experimental model was built using a 5-mil brass sheet with styrofoam ( $\epsilon_r \approx 1.05$ ) strips attached along the periphery to support it. A half-height (dimension  $H$  in Fig. 2.1a) of 11.0 cm was used for the antenna. A microwave diode (HP-5082-2215) was connected across the feed gap to detect directly the modulated RF signal (at GHz). The diode was left unbiased (to prolong its life). This, however, results in a narrower dynamic range. This explains the levelling off of the measured pattern at around 15 dB that is seen in Fig. 4.5. Table 4.1 summarizes the comparison between theory and experiment. It is seen that excellent agreement is obtained between the two for all the important aspects of the pattern viz., the 3 dB and the 10 dB beamwidth and the first side lobe level. A similar agreement between the theory and experiment has been observed for other antenna lengths between  $3\lambda_0$  and  $10\lambda_0$ . Comparison between theory and experiment has also been made for other flare angles of the LTSA. Fig. 4.4 illustrates the comparison of the 3 dB beamwidth for flare angles varying between  $8^\circ$  and  $21^\circ$  for a fixed length of  $5\lambda_0$ . The slight systematic discrepancy seen in the H-plane is caused by the styrofoam mount that was used during the measurements. Favorable comparison has also been obtained for an  $8\lambda_0$  long antenna over these flare angles. The H-plane beamwidth is relatively insensitive to the flare angle of the antenna as it does not 'see' the aperture width. In all the cases tested, the LTSA half-height  $H$  satisfied  $H \geq 2.75\lambda_0$  and  $H \geq 3W_0$ , where  $W_0 = L \tan \gamma$ . This restriction is placed on  $H$  so that comparison with theory (which assumes infinite  $H$ ) is meaningful.

The computed 3 dB and 10 dB beamwidths of the LTSA in the E- and the H-plane as a function of  $L/\lambda_0$  and with  $2\gamma$  as a parameter are plotted in Fig. 4.5

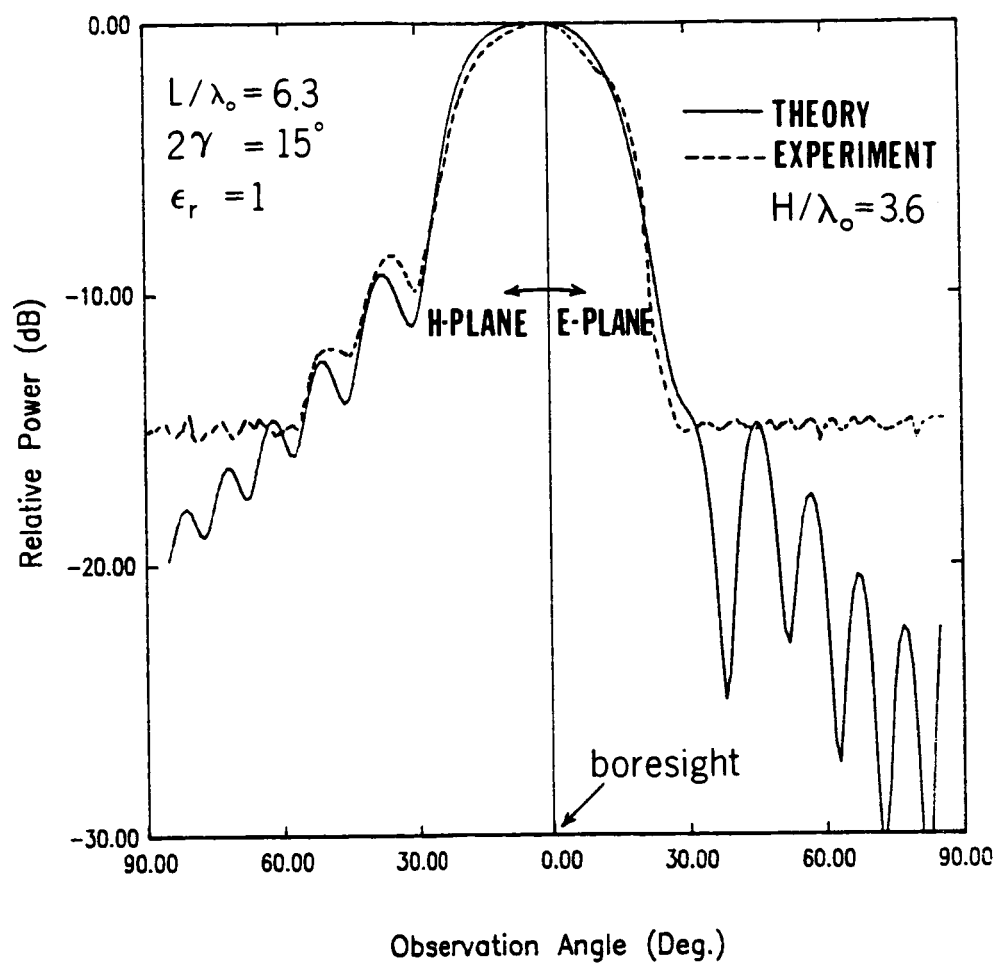


**Fig. 4.3** Radiation pattern of TEM-LTSA.

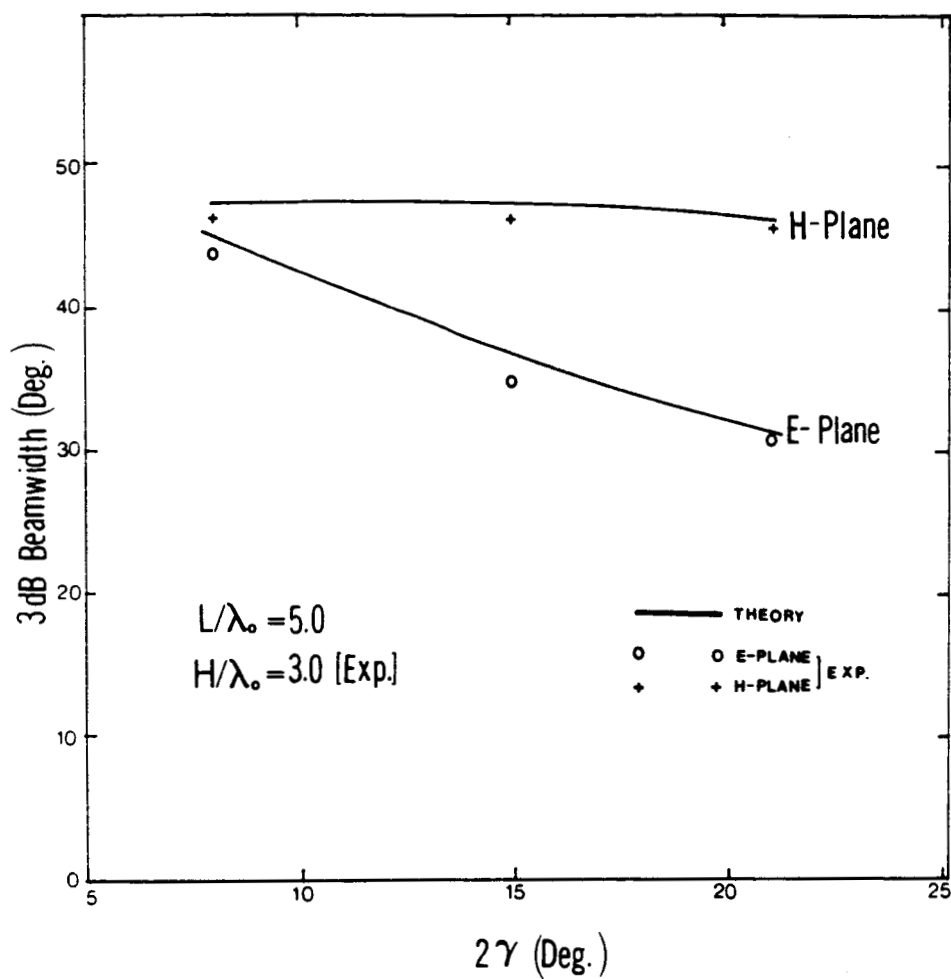


**Fig. 4.4** Measured and computed beamwidths of TEM-LTSA versus flare-angle.

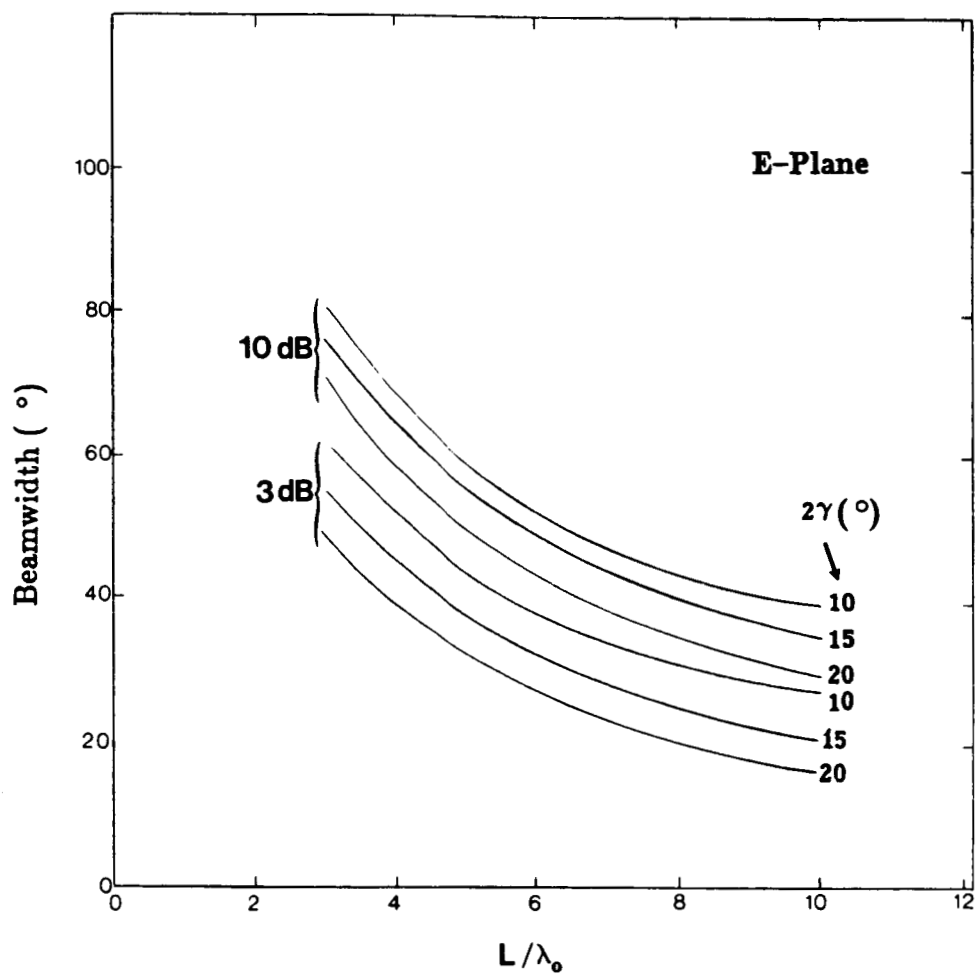


Fig. 4.5 E-plane beamwidth of TEM-LTSA versus normalized length.

and Fig. 4.6 respectively. Also plotted in Fig. 4.6 is the 3 dB beamwidth (H-plane) of a uniform magnitude magnetic line source supporting a travelling wave with freespace propagation constant. The line source is assumed to lie along the axis of the TEM-LTSA. Data for this case is obtained from Fig. 11.3 of [22]. (Note: The element pattern of the line source is *not* considered in Fig. 11.3 of [22], inclusion of which would have resulted in a null in the end-fire direction of the antenna. This is ofcourse consistent with what had already been stated in subsection 1 on the use of the freespace Green's function in computing the far-fields. It is customary to ignore the element pattern while plotting the 3 dB beamwidth of a travelling antenna as is done in [22]). It is seen that the solid curve agrees very closely with the data of [22] suggesting that the TEM-LTSA behaves as a travelling wave antenna in the H-plane. The TEM-LTSA supports a spherical wave as opposed to a plane wave in the magnetic line source case. In spite of this difference, the two have an almost identical 3 dB beamwidth. It can be shown that the H-plane patterns of the TEM-LTSA, and that of a magnetic line source supporting a freespace travelling wave (denoted by the superscript TWA) are given by

$$E_{\theta}^{TEM-LTSA}(\phi) = \frac{\sin \phi}{\{k_0 L(1 + \cos \phi)\}} |F[k_0 L(1 + \cos \phi)]|$$

$$E_{\theta}^{TWA}(\phi) = \frac{\sin \phi}{k_0 L(1 + \cos \phi)} \sin \left\{ \frac{k_0 L}{2} (1 + \cos \phi) \right\}$$

The element pattern  $\sin \phi$  is ignored from the second of these expressions, in the data plotted in Fig. 4.6. Incidentally the first expression that has been obtained using the theory presented here, correctly predicts the end-fire nature of the LTSA pattern, in contrast to the latter. Use of the half-plane Green's function results in the Fresnel integral  $F(\cdot)$  in the former compared to the  $\sin(\cdot)$  factor seen in the



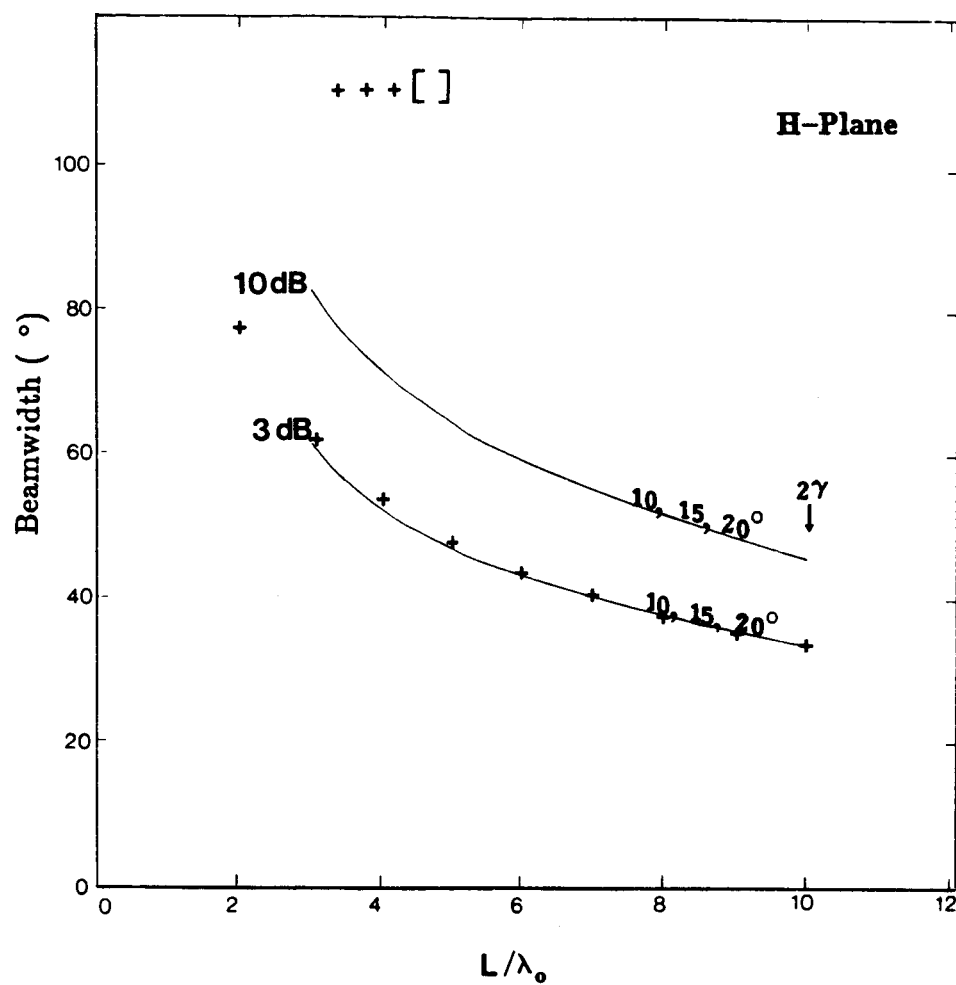


**Fig. 4.6** H-plane beamwidth of TEM-LTSA versus normalized length.

latter that results on using the freespace Green's function. The H-plane pattern of the LTSA is not sensitive to the actual variation of the field across the slot width but only to the *average* of the slot field. This average slot field coincides with the *equipotential* surface of the coplanar fin structure (cf. Fig. 4.1) that lies along the antenna axis. Although the TEM-LTSA supports a spherical wave, the field for which decays along the antenna axis, the average value remains the same throughout. This explains for the fact that the 3 dB beamwidth of the spherical-wave-supporting TEM-LTSA agrees so closely with that of a plane-wave-supporting travelling wave antenna.

A similar analogy with a travelling wave antenna is meaningless in the E-plane, as a magnetic line source predicts an identically zero pattern in the E-plane.

#### 4.2. Dielectric Supported Antennas

Fig. 4.7a shows the geometry of the tapered slot antenna supported by a dielectric substrate having  $\epsilon_r > 1$ . The aperture distribution in the tapered slot is determined via the stepped approximation and by utilizing the transmission line data on a wide uniform slot line. The presence of the dielectric is accounted for in the determination of the aperture distribution but is ignored in the subsequent step that utilizes the half-plane Green's function to compute the far-fields from the tapered slot.

1. **Stepped Approximation.** Fig. 4.7b illustrates a stepped approximation to the continuous taper obtained by considering it to be made up of a number of sections of uniform width for which the impedance and slot wavelength vary from section to section in accordance with the slot width. For the purpose of radiation pattern calculations, it is further assumed that the step junctions do not generate

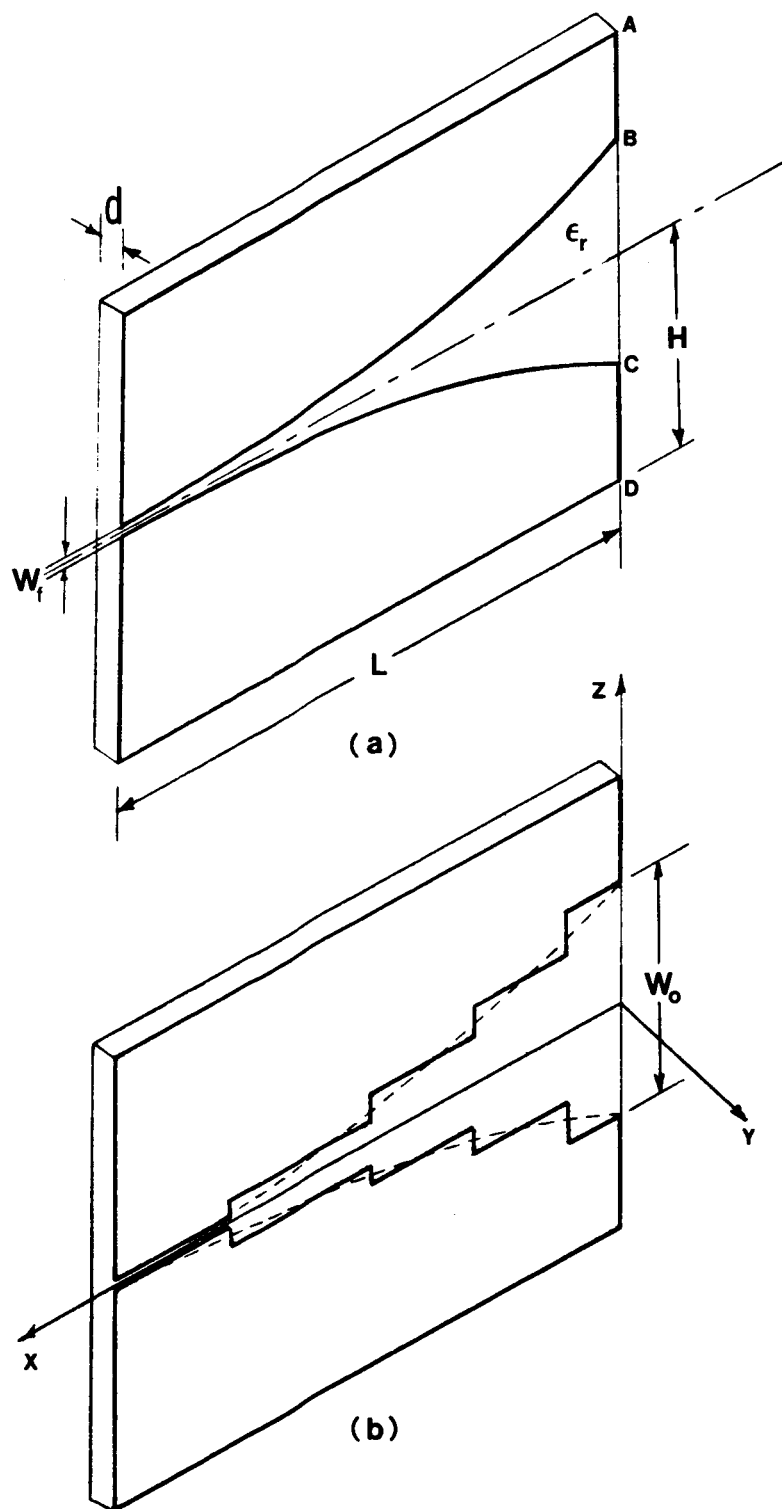


Fig. 4.7 Geometry of Tapered Slot Antenna. (a) Original problem (b) Stepped approximation.

any higher order modes. As the radiation pattern is stationary with respect to the aperture distribution [9], these approximations are not expected to result in noticable discrepancies in the pattern. That this is the actual case is shown in a later section by comparing with experiment.

The phase distribution in each uniform section is the same as that of an equivalent slot line having the same parameters. The slot wavelength  $\lambda'$ , the characteristic impedance  $Z_0$  and the slot electric field of a uniform wide slot line have been obtained in Chapter 3 by the spectral Galerkin's technique. The slot electric field is found up to a multiplicative constant. To account for the taper and to relate the fields from section to section, a power continuity criterion is enforced at the step junction of two adjacent slots. This criterion implies that there is no reflection or radiation at the step junction and, therefore, provides a field distribution corresponding to a purely propagating wave on the tapered structure. This constant power constraint determines the multiplicative constant in each uniform section. Other criteria such as constant voltage across each slot have also been tried (for the special case of air dielectric LTSA) but yielded results not differing much from the ones obtained with power conservation. The power conservation criteria is more physical in nature and suggests that the non-terminated tapered structure supports a purely propagating wave. It enables, in a very elegant manner, the use of transmission line properties viz.,  $\lambda'$ , and  $Z_0$  of the non-TEM slot line in the determination of the slot field distribution for the tapered structure. It recovers the field distribution approximately, but very closely, for the special case of a TEM-LTSA that can be solved more rigorously as in section 4.1.

The power  $P_f$ , the characteristic impedance  $Z_0$  and the slot electric field  $E_z^s$

are related in (3.4) and (3.5) and may be recast in the form

$$P_f = \frac{|\tilde{E}_z(0)|^2}{Z_o} \quad (4.6)$$

For the basis functions chosen in (3.3),  $\tilde{E}_z(0) = a_1$ , where  $a_1$  is the amplitude of the first transverse basis function. A constant power flow along the slot implies that

$$\dots = \frac{|a_1^{i-1}|}{\sqrt{Z_o^{i-1}}} = \frac{|a_1^i|}{\sqrt{Z_o^i}} = \frac{|a_1^{i+1}|}{\sqrt{Z_o^{i+1}}} = \dots = \sqrt{P_f} = \text{constant} \quad (4.7)$$

where the superscripts denote the section number. Renormalizing the mode coefficients in (3.3) as per (4.7) and inserting the phase factor of the propagating slot wave, the z-directed slot field  $E_z^i$  in the  $i^{\text{th}}$  section is given by

$$\begin{aligned} E_z^i(x', z') &= e^{jk_z^i z'} \left( \frac{2\sqrt{Z_o^i}}{\pi W^i} \right) \sum_{n=1}^{M_z^i} \frac{a_n^i T_{2(n-1)} \left( \frac{2z'}{W^i} \right)}{\sqrt{1 - \left( \frac{2z'}{W^i} \right)^2}} \\ &\triangleq e^{jk_z^i z'} E_a^i(z') \end{aligned} \quad (4.8)$$

The mode coefficients  $a_n^i$  in the  $i^{\text{th}}$  section are all normalized such that  $a_1^i = 1$  and all other mode coefficients are determined in terms of  $a_1^i$ . Equation (4.8) completely determines the aperture distribution in the stepped structure both in magnitude and in phase. The far-zone field  $E_\theta^i$  from the  $i^{\text{th}}$  section is obtained by integrating (4.8) over the  $i^{\text{th}}$  section with (4.3) as a kernel. Radiation from the antenna is obtained by adding up the contributions from all sections. It can be shown that the result for  $E_\theta^i$  can be obtained in a closed form. The result is

#### **E-Plane**

$$\begin{aligned} E_\theta^i(\theta) &= \tilde{E}_a^i(k_o W^i \cos \theta) \sqrt{\frac{2}{\sin \theta}} \left[ e^{-jk_o L c^i} \left\{ \frac{F^*(u_h^i) - F^*(u_l^i)}{\sqrt{c^i - \sin \theta}} \right\} \right. \\ &\quad \left. + \Gamma e^{jk_o L c^i} \left\{ \frac{F(\bar{u}_h^i) - F(\bar{u}_l^i)}{\sqrt{c^i + \sin \theta}} \right\} \right] \end{aligned} \quad (4.9)$$

H-Plane

$$\begin{aligned}
 E_{\theta}^i(\phi) = \tilde{E}_a^i(0) & \left[ \frac{e^{-jk_0 L c^i}}{(c^i + \cos \phi)} \left\{ \sin \phi \left[ F(p_h^i) e^{jv_h^i} - F(p_l^i) e^{jv_l^i} \right] \right. \right. \\
 & + \sin \left( \frac{\phi}{2} \right) \sqrt{2(c^i - 1)} \left[ F^*(q_h^i) - F^*(q_l^i) \right] \Big\} \\
 & - \Gamma \frac{e^{jk_0 L c^i}}{(c^i - \cos \phi)} \left\{ \sin \phi \left[ F(p_h^i) e^{-jv_h^i} - F(p_l^i) e^{-jv_l^i} \right] \right. \\
 & \left. \left. - \sin \left( \frac{\phi}{2} \right) \sqrt{2(c^i + 1)} \left[ F(\bar{q}_h^i) - F(\bar{q}_l^i) \right] \right\} \right] \quad (4.10)
 \end{aligned}$$

where,  $c^i = (\lambda_0/\lambda')_{i^{th} \text{ section}}$ ,  $k_0 = 2\pi/\lambda_0$

$$\begin{aligned}
 u_h^i &= k_0 x_h^i (c^i - \sin \theta), & \bar{u}_h^i &= k_0 x_h^i (c^i + \sin \theta) \\
 v_h^i &= k_0 x_h^i (c^i + \cos \phi), & \bar{v}_h^i &= k_0 x_h^i (c^i - \cos \phi) \\
 q_h^i &= k_0 x_h^i (c^i - 1), & \bar{q}_h^i &= k_0 x_h^i (c^i + 1) \\
 p_h^i &= k_0 x_h^i (1 + \cos \phi)
 \end{aligned}$$

and  $x_l^i, x_h^i$  are the lower and upper coordinates respectively of the  $i^{th}$  section.  $F(\cdot)$  is the Fresnel integral defined in (4.4) and  $*$  denotes complex conjugation. For the sake of generality, the contribution due to a backward travelling wave on the aperture with a relative amplitude  $\Gamma$  is also included in the above expressions.  $\tilde{E}_a^i(\cdot)$  is determined from (3.3), (3.7) and (3.8). Numerical studies have indicated that considering only the dominant term in (3.3) gives sufficiently accurate results for the pattern, in which case  $\tilde{E}_a^i(\cdot) = \sqrt{Z_0^i} J_0(\cdot)$ .

#### 4.3. Numerical Results and Discussion

The validity of the stepped approximation has been verified by comparing the radiation patterns of a *TEM-LTSA* obtained using the aperture distribution determined by (a) the stepped approximation, and (b) the more accurate method of conformal mapping employed in section 4.1. Fig. 4.8 shows the comparison

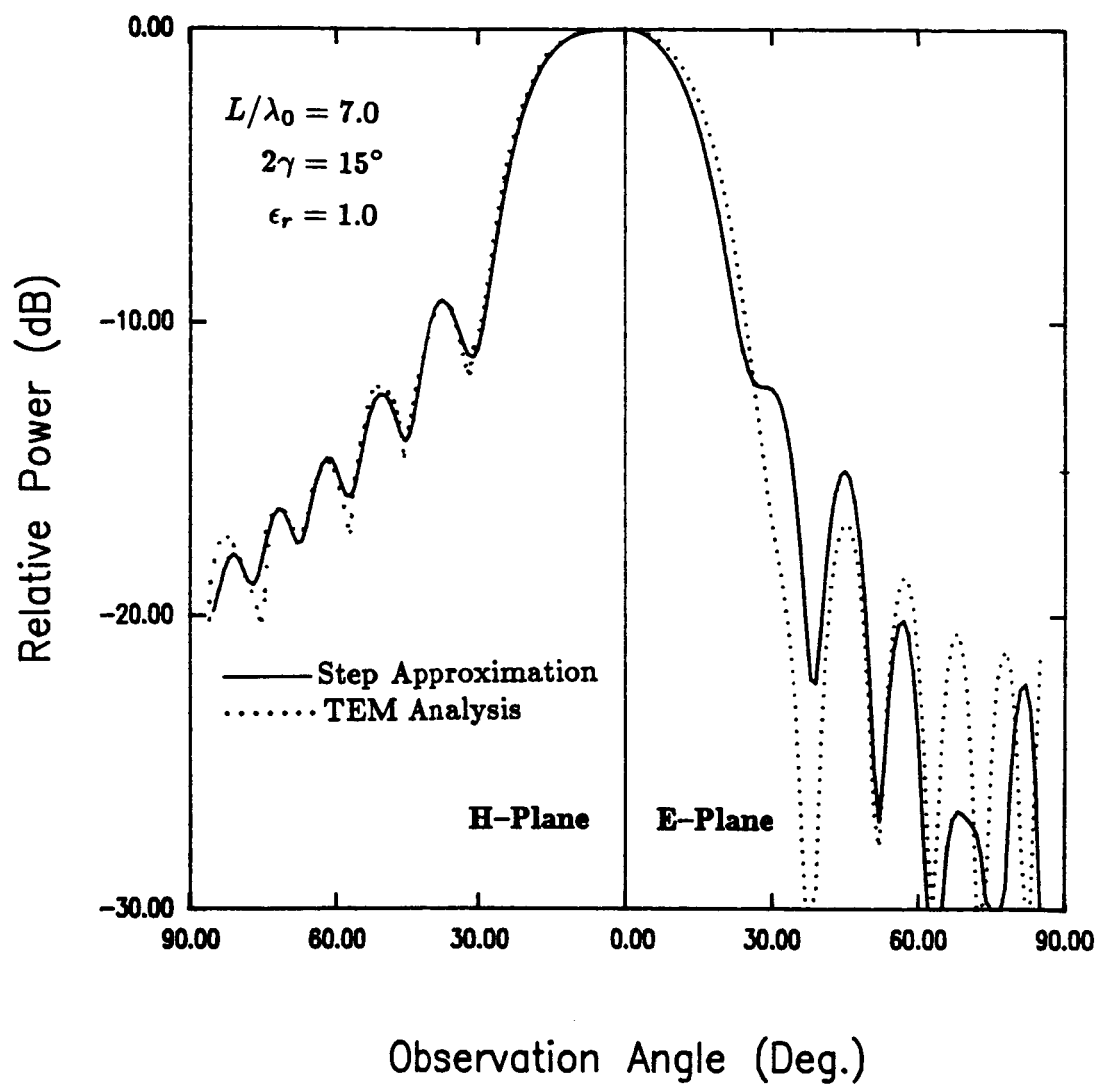


**Fig. 4.8** Radiation patterns of TEM-LTSA obtained using stepped approximation and exact aperture distribution.

between the two for an LTSA with  $2\gamma = 15^\circ$  and  $L = 7\lambda_0$ . Convergent results for the pattern in the stepped model were obtained with 5 steps/wavelength. The H-plane pattern is less sensitive to the exact shape of the aperture and the two cases are almost indistinguishable. The stepped model predicts a slightly narrower main beam in the E-plane compared to the TEM analysis case. However, the difference is not very significant. Favorable comparison between the two validates the stepped model for  $\epsilon_r = 1$  antenna. The model should also be valid for dielectric supported antennas when the substrate is electrically thin. In all the subsequent computations, 5 steps/wavelength are chosen in the stepped model.

All the pattern measurements reported in this section are done with the test antenna in a receiving mode. A microwave diode is connected across the feed gap to detect the RF signal. The diode may be biased or left unbiased depending on the dynamic range it provides. In most cases, linearity of the diode was checked (for faithful power level reproduction) before taking the actual measurements. Also, for the sake of clarity, results presented below are categorised according to the taper shape.

1. **LTSA.** Fig. 2.1 shows the geometry of a Linearly Tapered Slot Antenna (LTSA). Fig. 4.9 shows the comparison between theory and experiment for an LTSA built on a 20-mil,  $\epsilon_r = 2.22$  (Duroid) substrate. The flare angle  $2\gamma$  of the antenna was  $10^\circ$  and  $L = 4.2\lambda_0$  as measured at 10.0 GHz. A good agreement between the two is seen. The slight ripple seen in the experimental E-plane main lobe is due to the finite height  $2H$  of the antenna. Table 4.2 summarizes the comparison between the two. Dispersion data on the slot wavelength  $\lambda'$  needed in the pattern calculations were obtained using the spectral Galerkin's technique of Chapter 3. However,



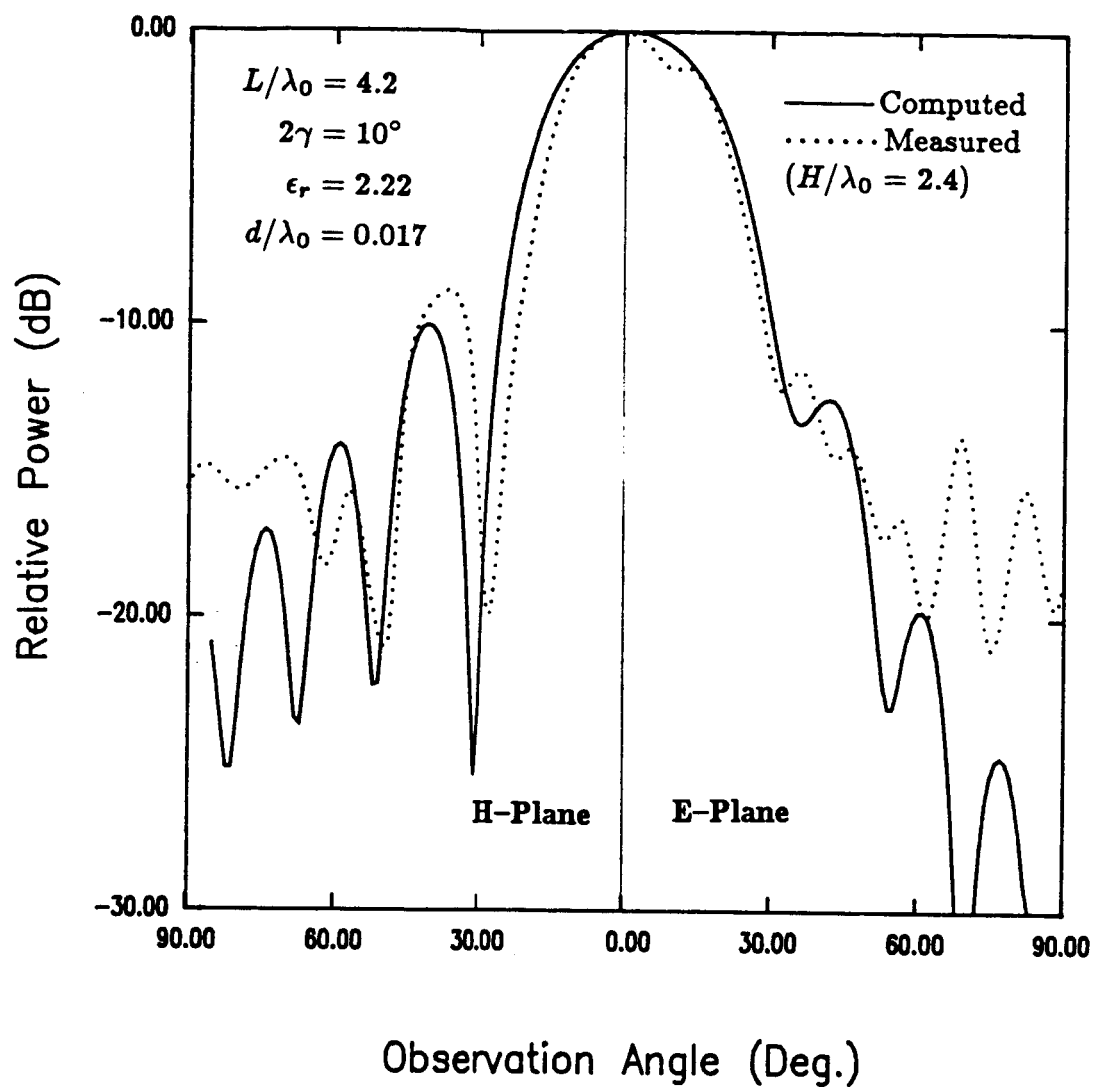


**Fig. 4.9** Measured and computed radiation patterns of LTSA on thin substrate.

**TABLE 4.1**  
**PATTERN COMPARISON FOR TEM-LTSA**

	3 dB Beamwidth ( ° )		10 dB Beamwidth ( ° )		First SLL (dB)	
	Theory	Measured	Theory	Measured	Theory	Measured
E-plane	31.8	34.3	47.8	44.1	-14.5	—
H-plane	42.2	39.0	57.6	60.0	-9.2	-8.6

$L/\lambda_o = 6.3, 2\gamma = 15^\circ$

**TABLE 4.2**  
**PATTERN COMPARISON FOR  $\epsilon_r = 2.22$  LTSA**

	3 dB Beamwidth ( ° )		10 dB Beamwidth ( ° )		First SLL (dB)	
	Theory	Measured	Theory	Measured	Theory	Measured
E-plane	39.8	38.3	61.0	57.0	-12.4	-11.5
H-plane	33.7	28.8	50.5	44.4	-10.0	-8.8

$d/\lambda_o = 0.017, L/\lambda_o = 4.2, 2\gamma = 10^\circ$

measurements done on  $\lambda'$  on this particular substrate indicated that the calculated slot wavelength was systematically displaced above the measured value by about +2.5%. Measurements were done up to a slot width of  $0.8\lambda_0$ . For a travelling wave antenna, this slight change in the wavelength (or equivalently, phase velocity) can have dramatic effects in the pattern beamwidths. Typically the 3 dB beamwidth changes by about 20% for a 2-3% change in the phase velocity [4] (the change being effected at the freespace velocity) for an antenna that is four freespace wavelengths long. At a slot width of  $0.74\lambda_0$  (that corresponds to the width of the slot at the termination for the antenna above) the calculated wavelength was +2.7% above the measured one. The normalized slot wavelength at the feed point of the LTSA for the above set of parameters is 0.892 and that at the termination is approximately 0.98. A correction factor of -2.7% for  $\lambda'$  was used all along the slot aperture in the computed patterns displayed in Fig. 4.9. Good agreement with experiment is obtained as seen in Fig. 4.9. If on the otherhand, the uncorrected slot wavelength were used in the computed patterns, a poorer agreement with experiment is expected. Fig. 4.10 shows the comparison between the computations based on corrected and uncorrected slot wavelengths. The corrected slot wavelength results in a pattern whose H-plane beamwidth at the 3 dB point is about 18.5% narrower compared to the one obtained using the uncorrected slot wavelength. It is clear that the slot wavelength must be found very accurately in order to predict an accurate beamwidth. The effect of this slight discrepancy in  $\lambda'$  on the pattern calculations becomes increasingly significant as the antenna length is increased (due to the accumulated phase shift the wave gathers as it progresses along the tapered slot). Furthermore, the slot wavelength has a more pronounced effect in the H-plane than

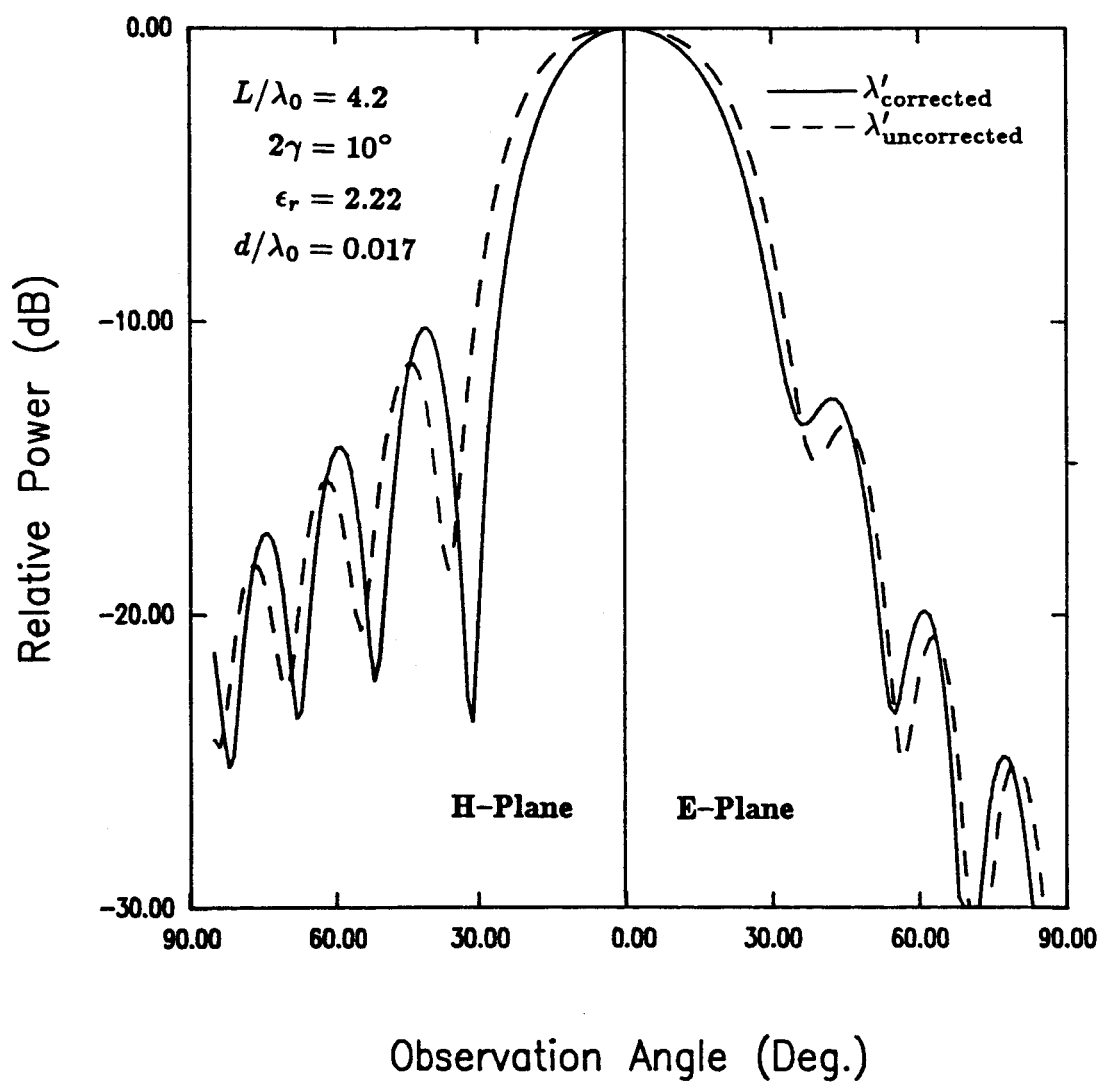


**Fig. 4.10** Radiation patterns of LTSA on thin substrate obtained using *corrected* and *uncorrected* slot wavelengths.

in the E-plane. This is because the H-plane pattern depends only on the phase velocity of the travelling wave (i.e.,  $\lambda'$ ) and the antenna length, whereas the E-plane pattern has additional dependence on the slot taper shape.

Patterns are shown only in the forward hemisphere ( $x < 0$ , cf. Fig. 4.7) where the theory is valid. Full experimental patterns covering the entire space are included in Appendix B both for the E- and the H-planes. The cross polar patterns for the antenna in the two principal planes were also measured and were found to be  $-19$  dB below the maximum of the copolar pattern.

The slot line data needed in the pattern computation in Fig. 4.9 were generated by running the slot line program for each uniform slot section. However, data could also have been obtained from the curve-fitted equations provided in Chapter 3. Fig. 4.11. shows the comparison of the patterns obtained using actual data (i.e., the computed slot wavelength without any correction factor) and the fitted data. The two agree very well indicating that curve fitted data can be readily used in the pattern computations.

Fig. 4.12 shows experimental confirmation of the pattern for an antenna with a larger taper angle of  $16^\circ$ . Other parameters of the antenna are  $\epsilon_r = 2.22$ ,  $d/\lambda_0 = 0.014$  and  $L/\lambda_0 = 4.0$ . The slot width  $W_0$  at the termination is  $1.124\lambda_0$ . The correction factor for  $\lambda'$  for this case was found to be  $-2.15\%$ . A very good agreement between the theoretical and experimental is seen. The computed pattern is calculated with the corrected slot wavelength. Fig. 4.13 illustrates the effect of the correction factor on the pattern. Computed patterns are shown with the uncorrected and the corrected slot wavelength. The 3 dB beamwidth in the H-plane for two cases differ by about 14%.

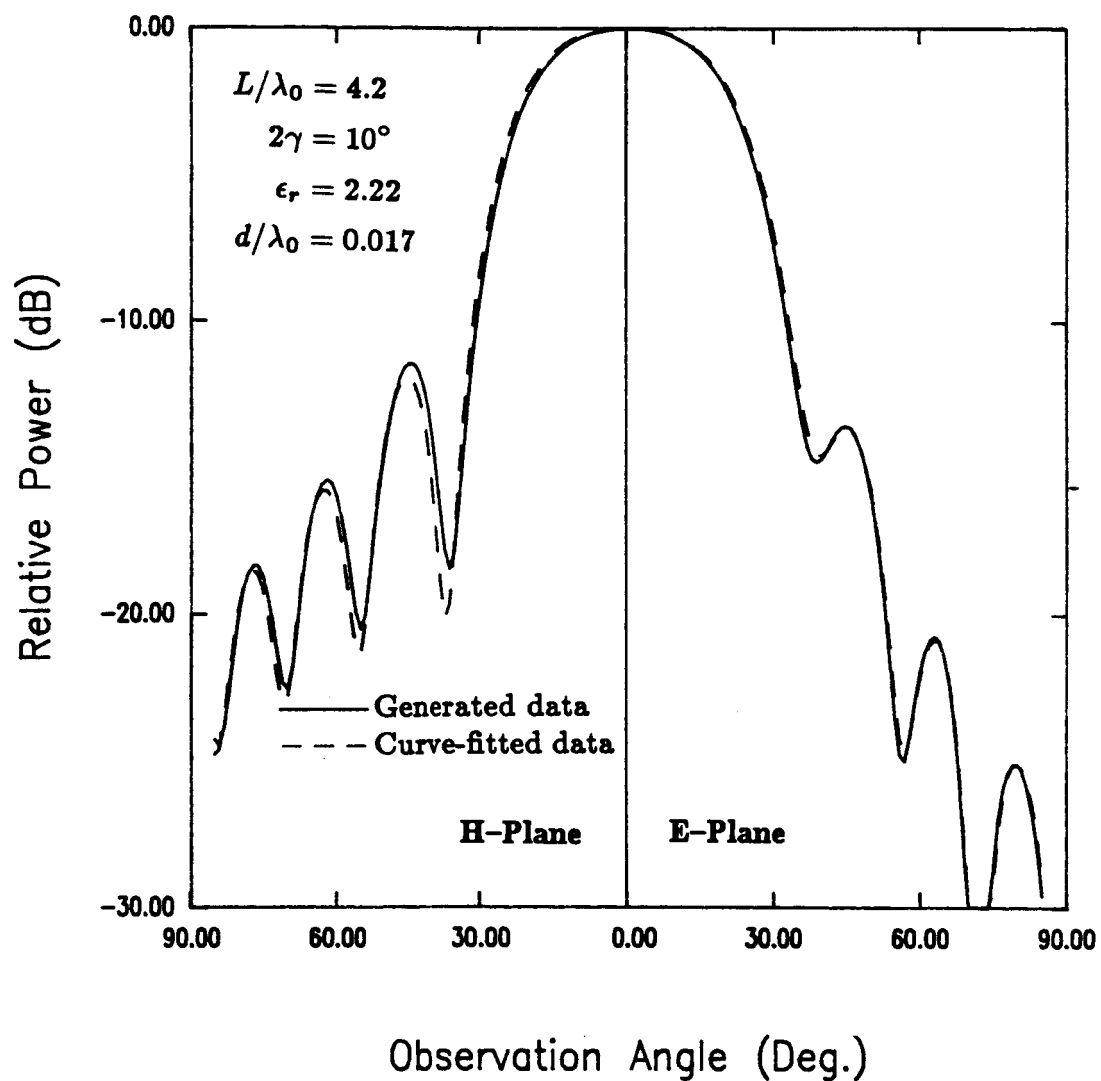


**Fig. 4.11** Computed radiation patterns of LTSA on thin substrate, obtained using *generated* slot line data and *curve-fitted* slot line data.

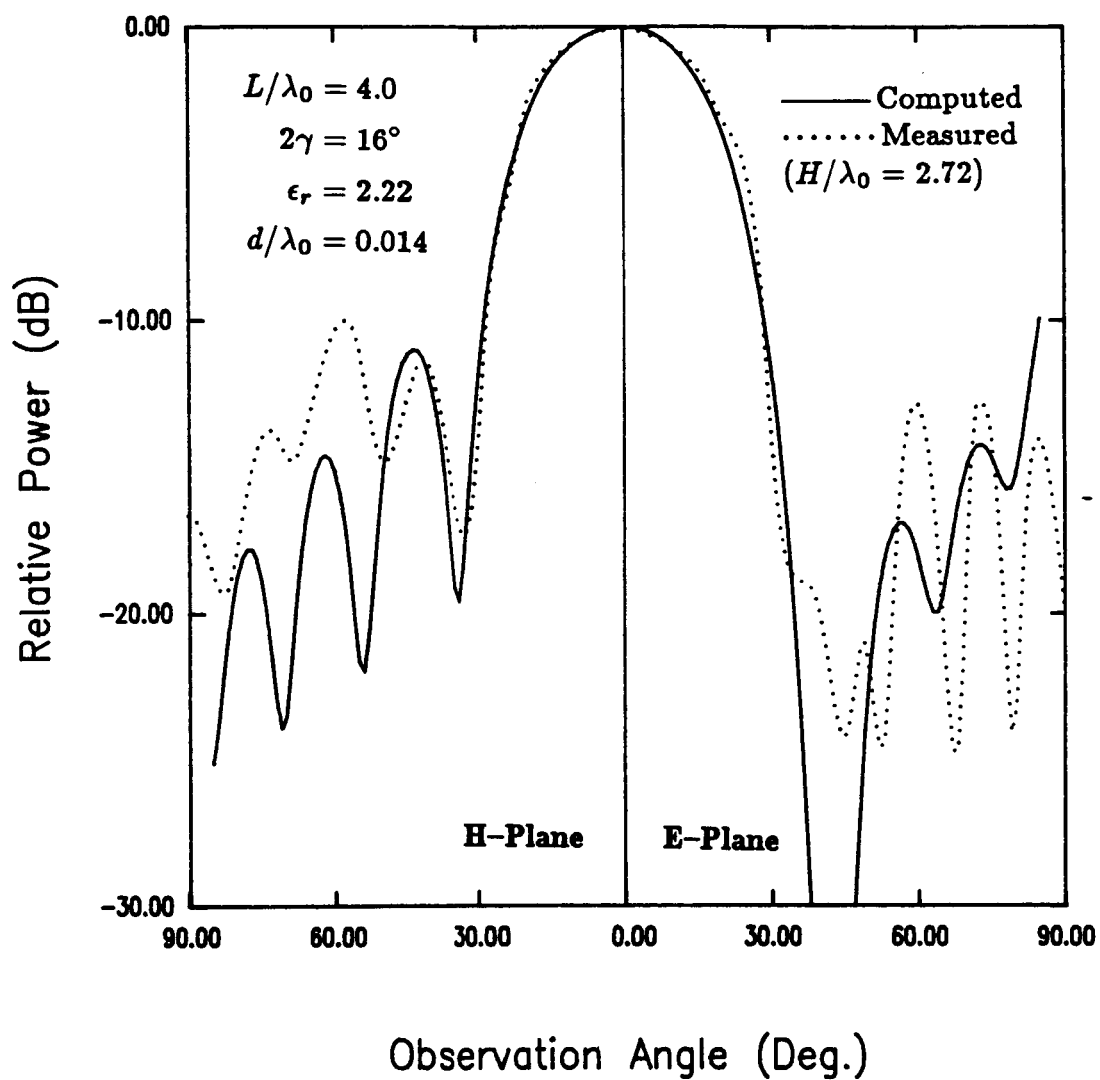


**Fig. 4.12** Measured and computed radiation patterns of a wide-flare-angle LTSA on thin substrate.

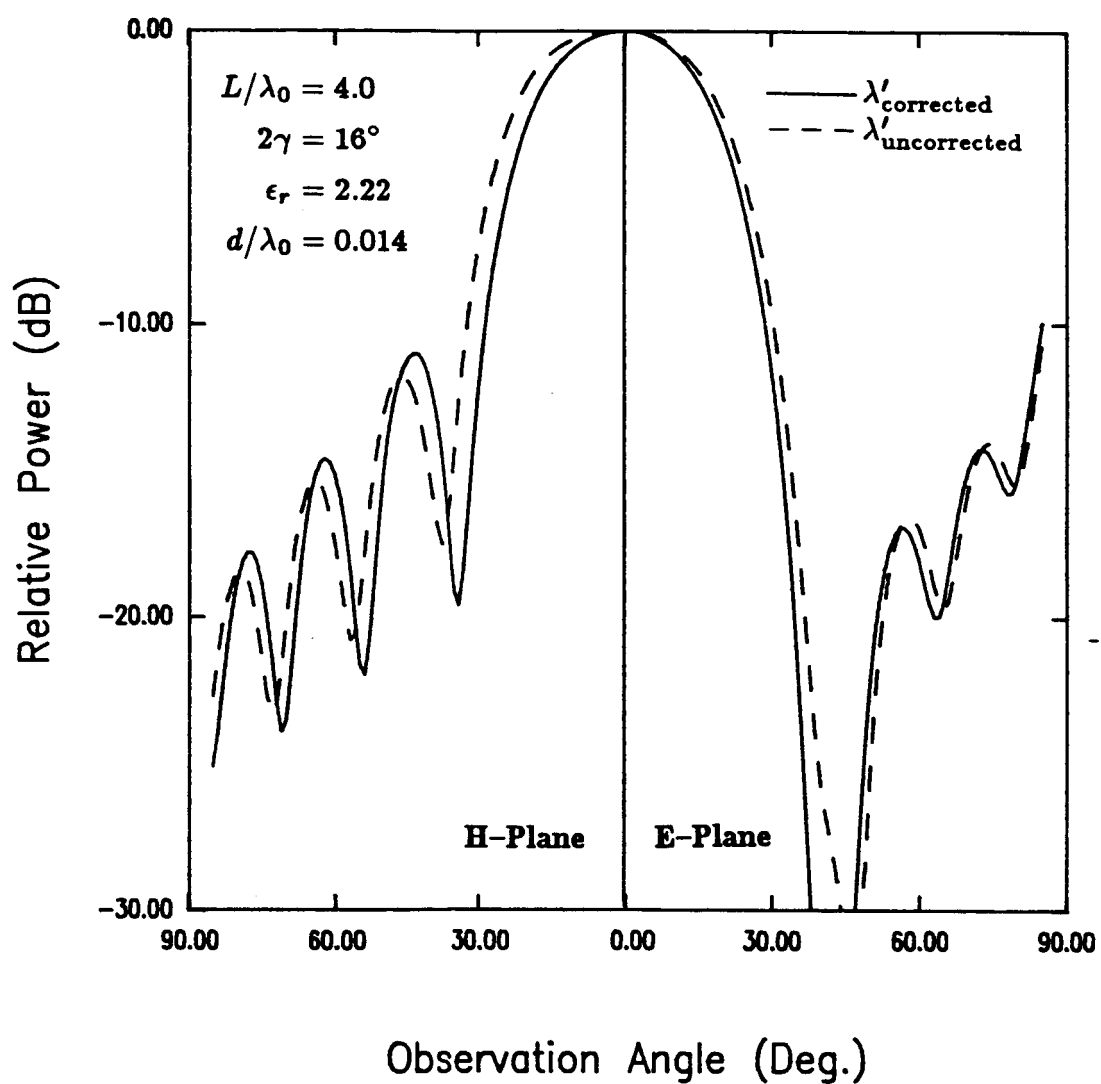


**Fig. 4.13** Computed radiation patterns of wide-flare-angle LTSA obtained using *corrected* and *uncorrected* slot wavelengths.



Results presented above for the two antennas are for a thin substrate ( $d/\lambda_0 < 0.02$ ). It is interesting to note that a nearly circular main lobe is obtained in both cases. Fig. 4.14a shows the patterns for a thick substrate case. The antenna was built on a 59-mil Duroid substrate (RT/Duroid 5880,  $\epsilon_r = 2.22$ ) corresponding to  $d/\lambda_0 = 0.06$  at 12.0 GHz.  $L = 6.1\lambda_0$  and  $2\gamma = 14.25^\circ$ . For this set of parameters, the slot width  $W_0$  at the termination is approximately  $1.5\lambda_0$ . The normalized slot wavelength increases from 0.83 at the feed gap to 0.92 at the termination. The experimental model had a half-height of 12.7 cm corresponding to  $H/\lambda_0 = 5.1$ . Fig. 4.14a shows a very good agreement between the experimental and theoretical results. The theory very accurately predicts the main lobe in both the principal planes and the first side lobe level in the H-plane. No correction factor for the slot wavelength was used in the computed patterns as measurements for the slot wavelength for a wide slot on a thick substrate were not performed. However, for the sake of comparing with the thin substrate case, patterns have been computed with and without a hypothetical correction factor of  $-2.5\%$  in the slot wavelength and are plotted in Fig. 4.14b. It is seen that, unlike the thin substrate case (cf. Fig. 4.10), correction does not change the main lobe beamwidth, although it appreciably changes the side lobe level in the H-plane. Computation done without any hypothetical correction factor agrees better with experiment as is seen in Fig. 4.14a. It appears that the normalized slot wavelength calculated by the spectral Galerkin's technique is quite accurate when it is not close to unity (as in the thin substrate case.) This corresponds to using an electrically thick substrate or one with a high relative permittivity. The experimental E-plane pattern had a slight dip of about 0.3 dB at the boresight (this and the slight ripple in the E-plane main

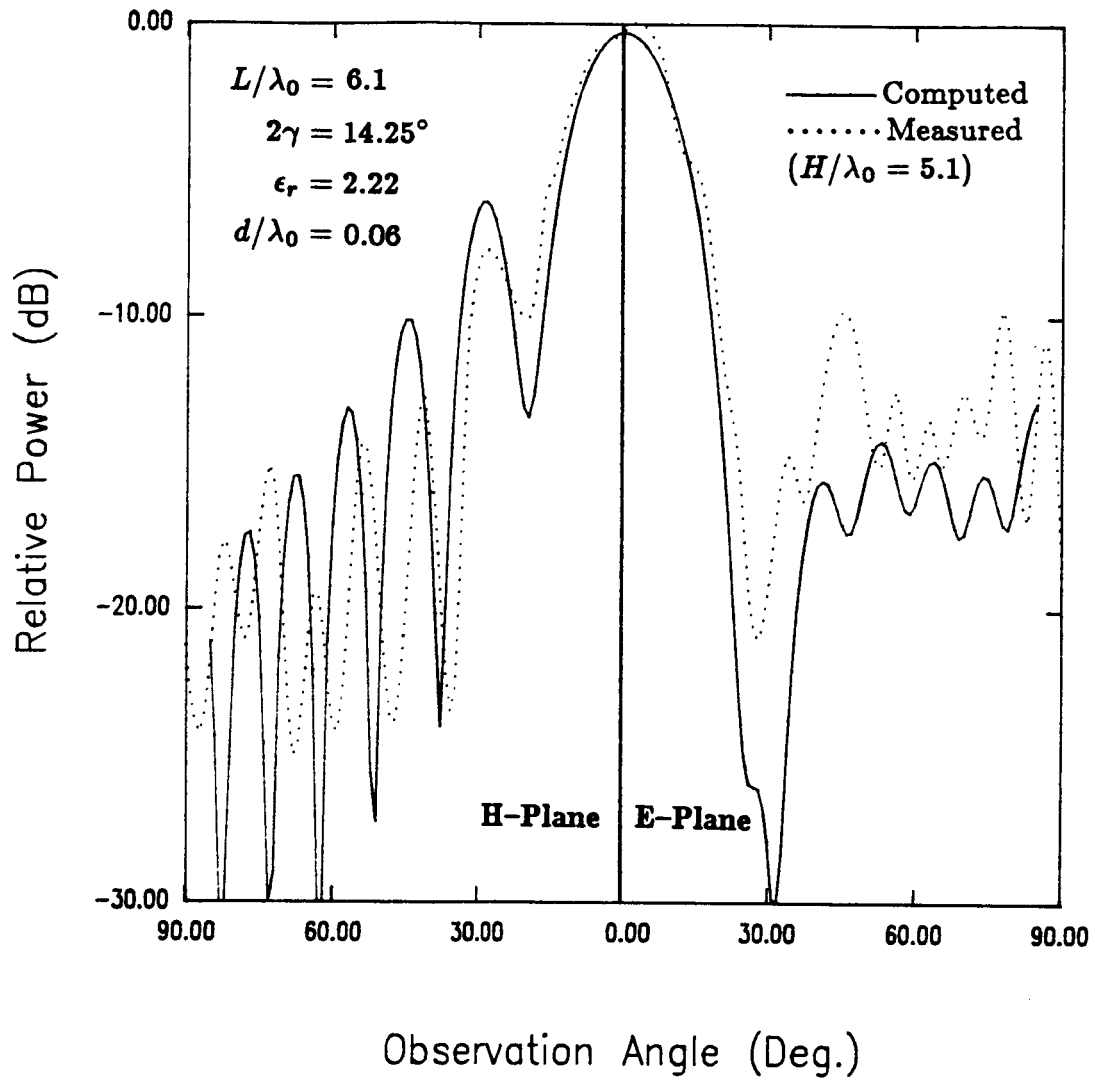


**Fig. 4.14a** Measured and computed radiation patterns of LTSA on thick substrate. Frequency = 12 GHz

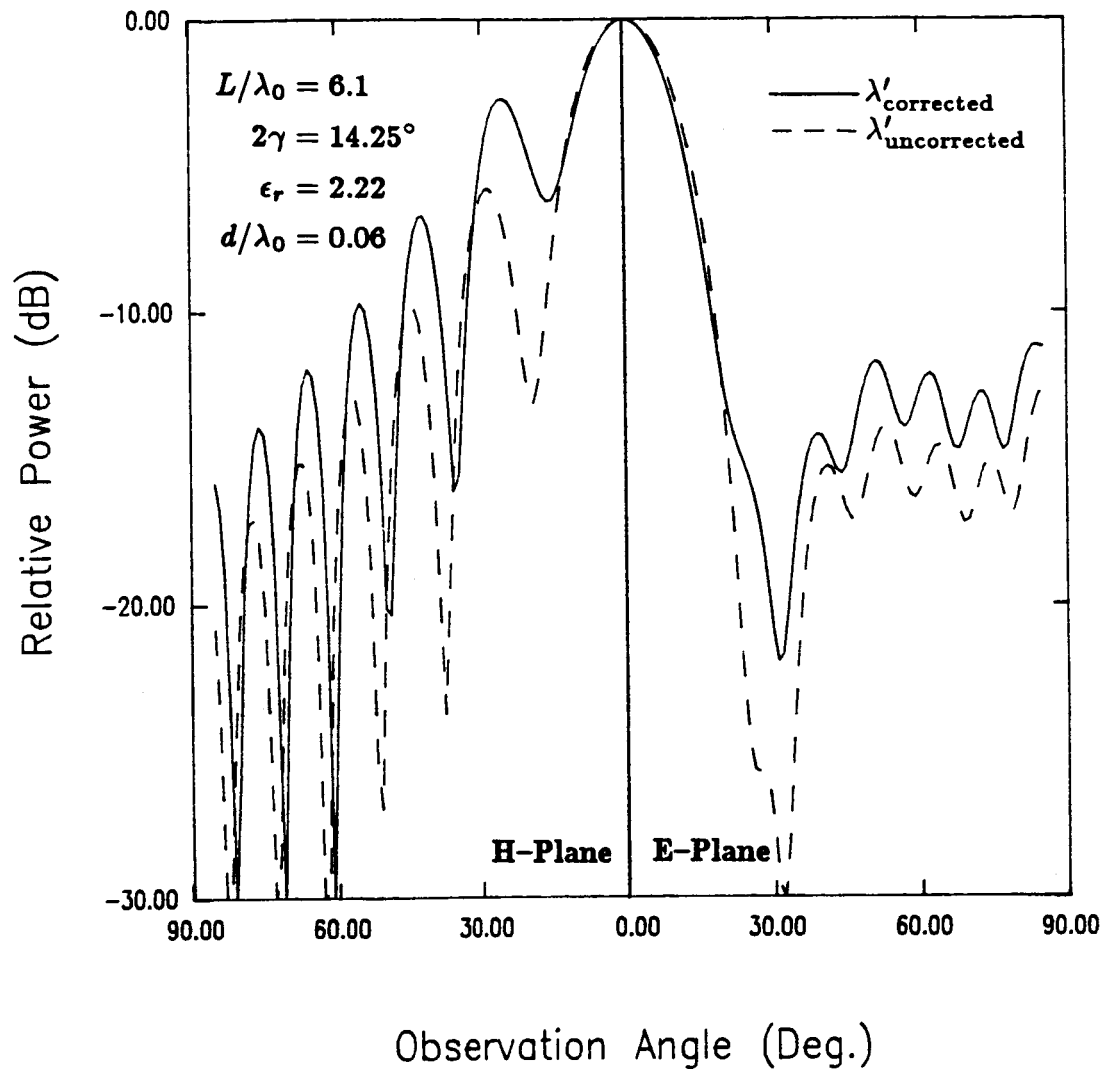


**Fig. 4.14b** Effect of wavelength correction on the radiation pattern of LTSA on thick substrate.

lobe could have been caused by the lateral truncation of the experimental model). This can be seen more clearly in Fig. B3. For proper comparison, the computed pattern is normalized so that the two patterns have the same value at the boresight. Fig. 4.15 shows the comparison for the antenna at 8 GHz. The dip at boresight at this frequency was around 1.5 dB and is rather high. Full experimental patterns are shown in Fig. B4. The patterns differ considerably in the E-plane, which is more sensitive to the lateral dimensions of the antenna. The 3 dB beamwidths in the H-plane for the two patterns differ by about 30%.

Comparison for the pattern was also done for a high- $\epsilon_r$  substrate. Fig. 4.16a shows the comparison for an LTSA built on a 10-mil RT/Duroid 6010.5 substrate. The antenna was made 15.0 cm long (corresponding to  $L/\lambda_0 = 4.0$  at 8.0 GHz) with a flare angle of  $14^\circ$ . For this set of parameters,  $d/\lambda_0 = 0.0068$ ,  $W_0 \approx 1\lambda_0$ . The experimental model had  $H = 12.7$  cm, the same value as in the previous antenna. It is seen from Fig. 4.16a that a good agreement is obtained between the experiment and theory. No correction factor for  $\lambda'$  was introduced in the computations. The normalized slot wavelength increases from a value 0.582 at the feed gap to about 0.91 at the termination. Again, for the sake of comparing with the low- $\epsilon_r$ , and thin substrate case, patterns are compared with and without a hypothetical correction factor of  $-2.5\%$  in the slot wavelength and the results plotted in Fig. 4.16b. This hypothetical correction factor results in a H-plane 3-dB beamwidth that is about 10% narrower than the one obtained without any correction. This is in contrast to 18.5% for the thin substrate case. Pattern computed without any correction factor agrees fairly well with experiment, although a slightly better agreement could be obtained (especially the matching of minima in the H-plane) with some correction.

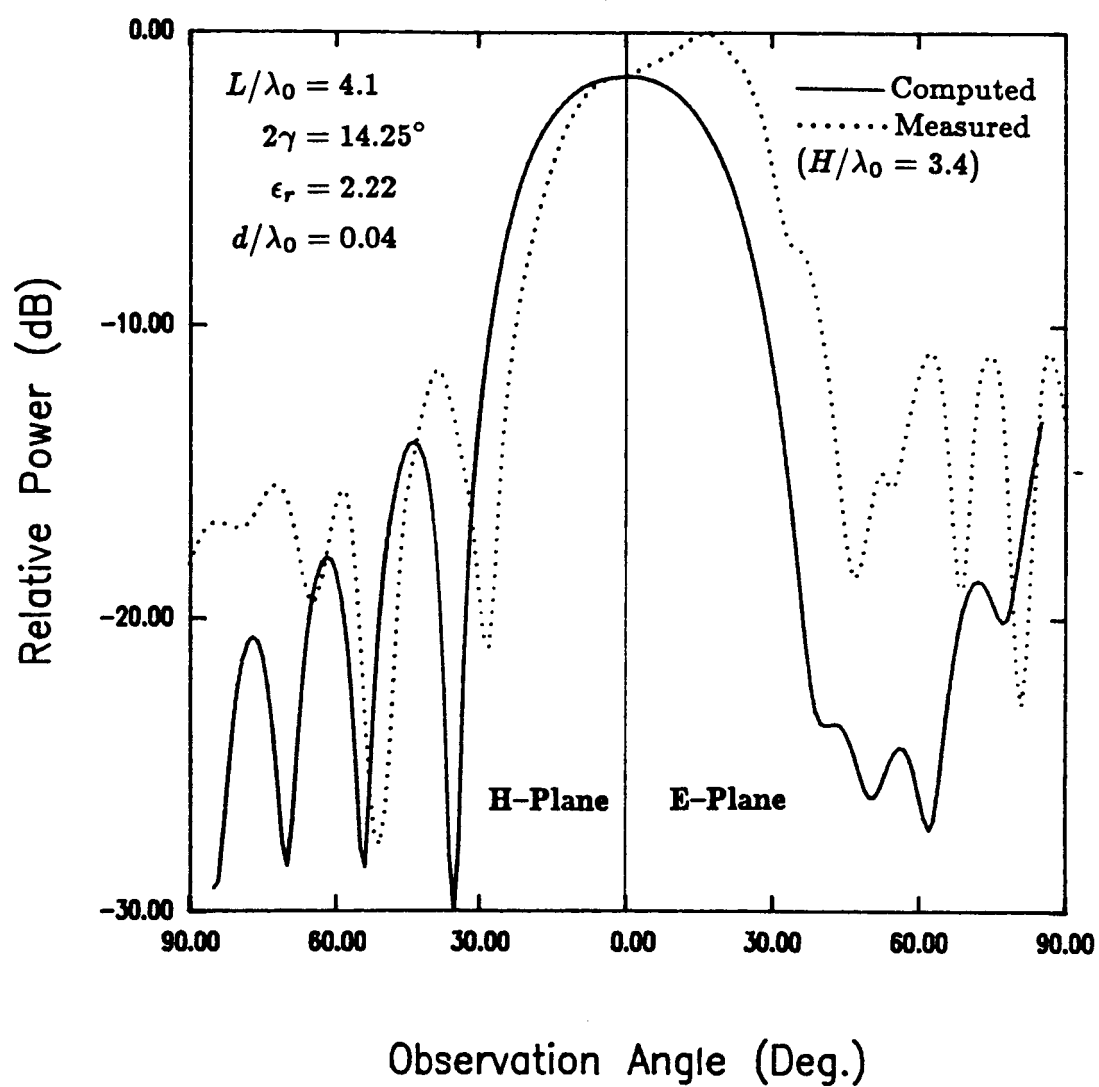


**Fig. 4.15** Measured and computed radiation patterns of LTSA on thick substrate. Frequency = 8 GHz.

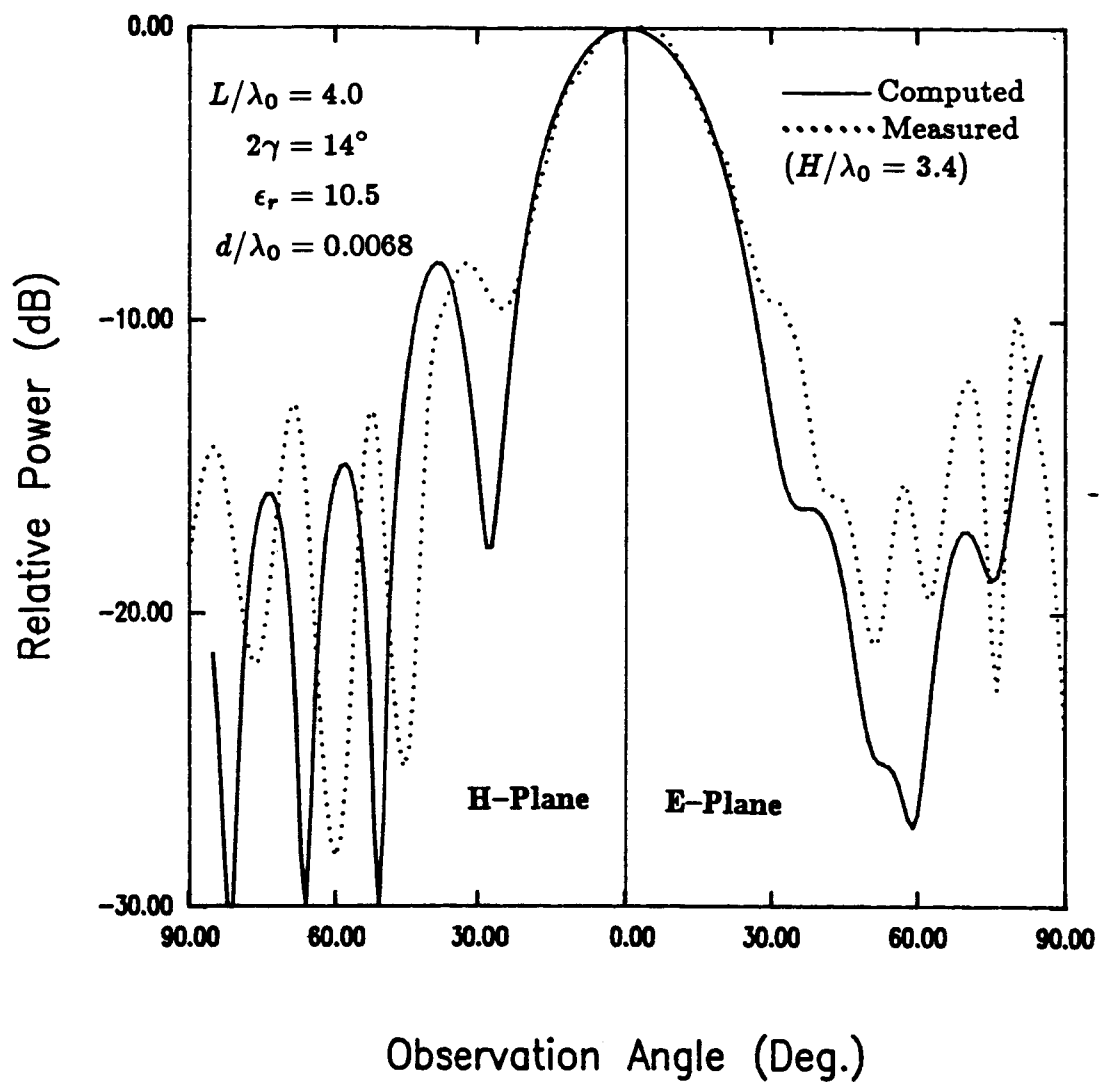


**Fig. 4.16a** Measured and computed radiation patterns of LTSA on high- $\epsilon_r$  substrate. Frequency = 8 GHz

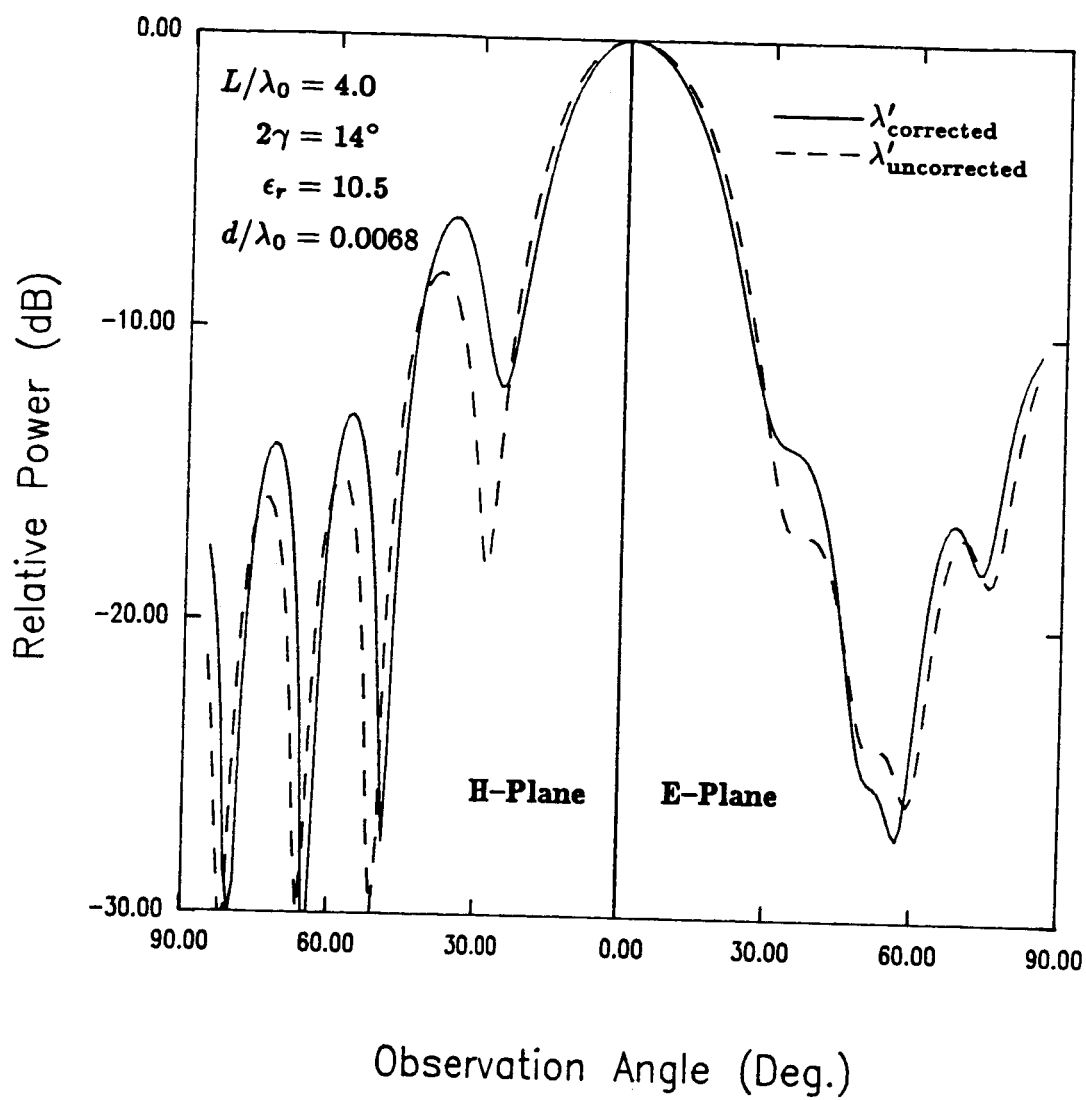


**Fig. 4.16b** Effect of wavelength correction on the radiation pattern of LTSA on high- $\epsilon_r$  substrate.

However, the change obtained is not as noticable as in the low- $\epsilon_r$ , and thin substrate case of Fig. 4.10. Also, no noticable dip is observed in the experimental E-plane pattern, as can be seen from Fig. B5. This is in contrast to Fig. B4 where a large dip is noticed in the E-plane, despite the fact that both the antennas have the same dimension  $H = 12.7$  cm. Clearly, the lateral truncation is affecting these two cases quite differently.

Fig. 4.17 illustrates the comparison for the high- $\epsilon_r$  substrate at 10 GHz. At this frequency,  $d/\lambda_0 = 0.0085$ ,  $L/\lambda_0 = 5.0$ , and  $W_0 = 1.25\lambda_0$ . No correction factor for  $\lambda'$  was introduced in the computed pattern. The computed pattern exhibits splitting in the H-plane main beam, typical of a long travelling wave antenna that supports a very slow wave. The measured pattern, however, does not exhibit this phenomenon. Also, the measured pattern was to some extent unsymmetric in both principal planes as can be seen from Fig. B6. This is possibly caused by the styrofoam mount that was used to support the thin substrate. It is seen from Fig. 4.17, that except for the splitting of the H-plane main beam, the theoretical predictions agree reasonably well with experiment.

It is interesting to compare the experimental 3 dB beamwidths in the H-plane for the LTSA's considered in Figs. 4.9, 4.12, 4.15, and 4.16a. All have approximately the same length ( $= 4\lambda_0$ ) but different substrates and their thicknesses. The flare angles of the above antennas are  $10^\circ$ ,  $16^\circ$ ,  $14.25^\circ$ , and  $14^\circ$  respectively and the H-plane beamwidths— $28^\circ$ ,  $40^\circ$ ,  $30^\circ$ , and  $30^\circ$  respectively. In contrast to the TEM-LTSA (cf. Fig. 4.4), the beamwidth for the dielectric supported antennas is not independent of the flare angle. This is because the antennas above have different slow wave factors ( $\propto \lambda_0/\lambda'$ ) owing to their different substrate parameters. Given the same substrate



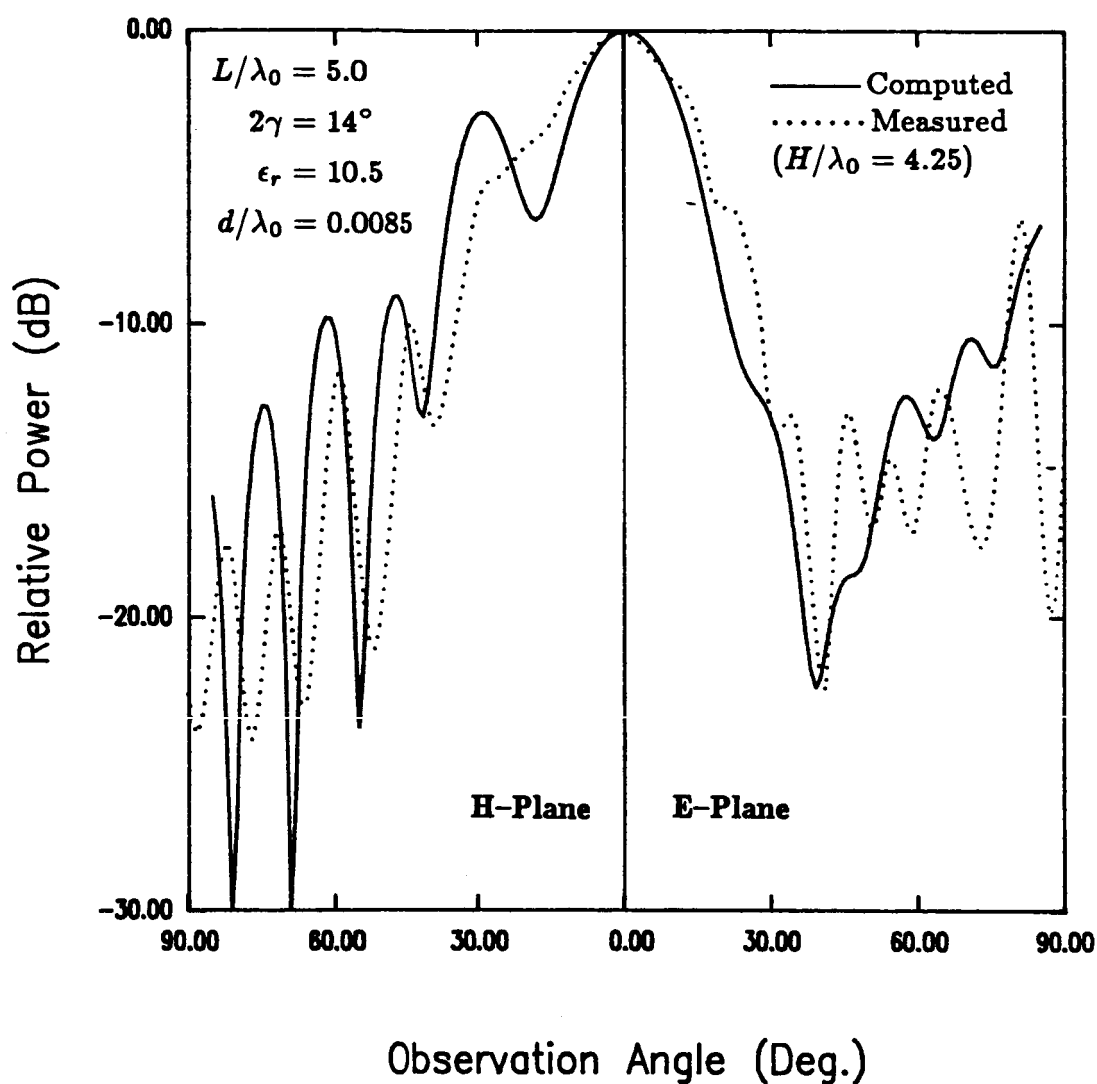


**Fig. 4.17** Measured and computed radiation patterns of LTSA on high- $\epsilon_r$  substrate. Frequency = 10 GHz.

parameters ( $\epsilon_r > 1$ ) and the length, an LTSA with a smaller flare angle supports a slower wave and has, consequently, a narrower H-plane beamwidth. This can be seen by comparing the beamwidth data from Figs. 4.9, and 4.10. The former has a beamwidth of  $28^\circ$  and the latter  $40^\circ$ . The experimental patterns presented in this dissertation could not be compared with those presented in literature [19, 26], as the latter made no mention of the height  $H$  that was used in the experimental model and knowledge of which is required for proper comparison. It is shown in Chapter 5 that the beamwidths are sensitive to the height  $H$  when it is small.

2. CWSA. Fig. 4.18 shows the geometry of a Constant Width Slot Antenna (CWSA). A short taper is included to form a transition between the narrow feed gap and the wide constant width slot. Fig. 4.19a shows the comparison between theory and experiment for a CWSA built on a 20-mil RT/Duroid 5880 ( $\epsilon_r = 2.22$ ) substrate. This substrate is the same as the one used for the LTSA in Figs. 4.9, and 4.12. Results are shown at 10 GHz and for  $L_f = 2.5$  cm,  $L_a = 14.8$  cm and  $W_o = 2.95$  cm. The short taper was modeled by the stepped approximation. The experimental model had a half-height  $H = 12.7$  cm. Fig. 4.19a illustrates a favorable comparison between the two. A correction factor of  $-2.7\%$  was used for  $\lambda'$  in the computed pattern. It is, however, seen that the experimental pattern exhibits higher far-out sidelobes than the computed one. It is felt that this could be due to the presence of a stronger backward wave on the aperture, and also (possibly) due to scattering by the metallic edge that is parallel to the edge ABCD and located at the feed gap (cf. Fig. 4.18). All the theoretical patterns computed in the present work have been obtained by using  $\Gamma = 0$  (i.e., magnitude of the backward wave) in (4.9) and (4.10), as indicated at the beginning of this discussion. To verify the first of the

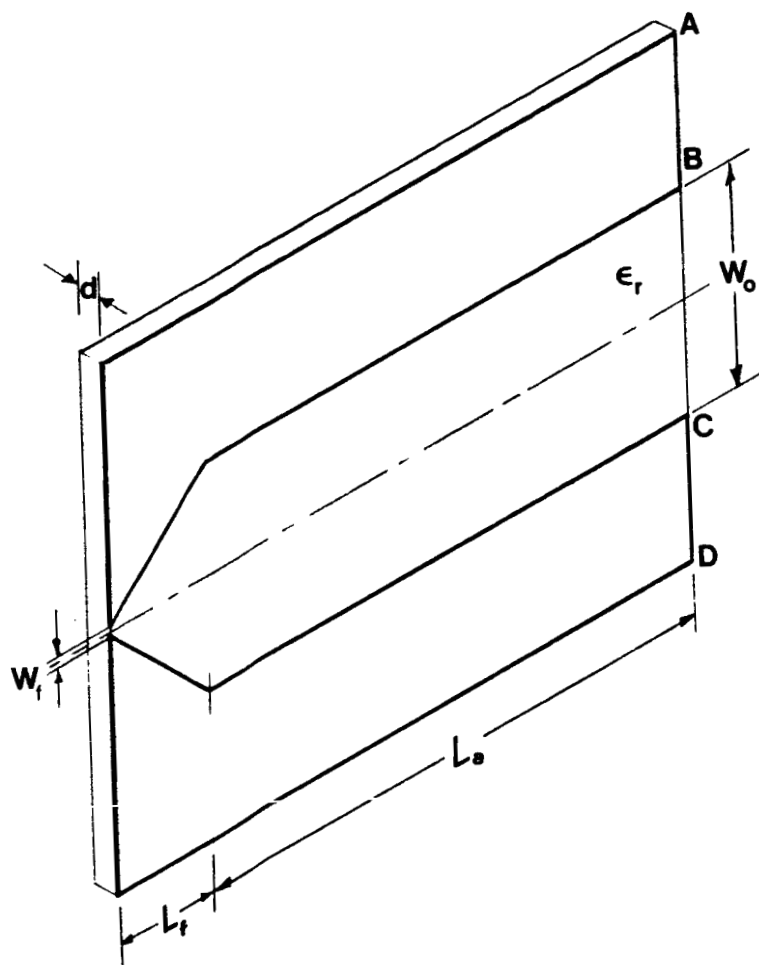


**Fig. 4.18 Geometry of CWSA.**

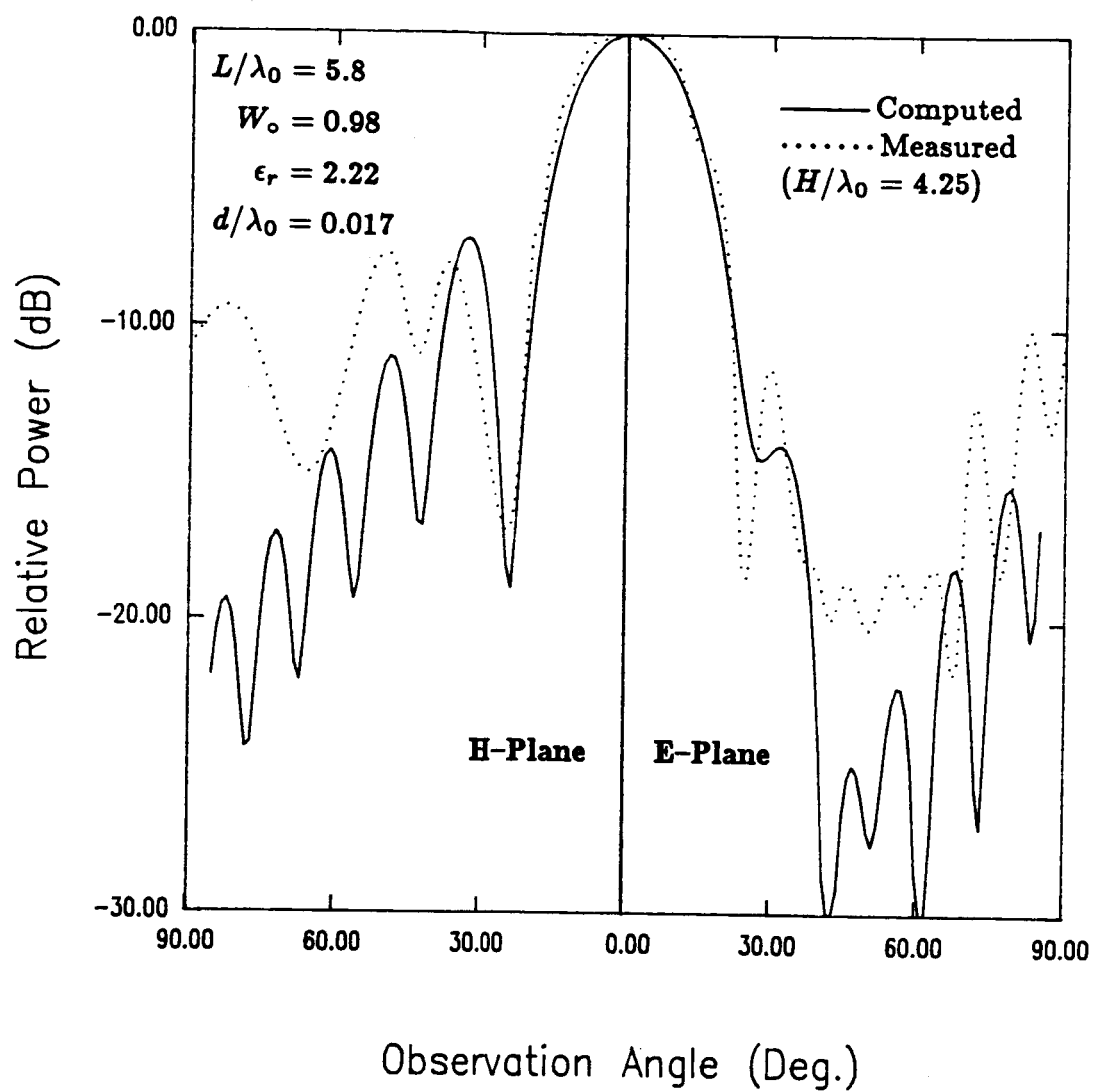


**Fig. 4.19a** Measured and computed radiation patterns of CWSA on thin substrate. Frequency = 10 GHz

above notions, patterns have been computed for the above CWSA using a different value of  $\Gamma$ . Fig. 4.19b compares the patterns obtained with  $\Gamma = -1, 0$ , and  $1$ . It is seen that higher far-out side lobes are obtained by including a backward wave in the aperture distribution. The main beam in either principal plane is, however, not effected much. This is in compliance with an earlier claim that the backward wave does not contribute much to the front lobe of the antenna.

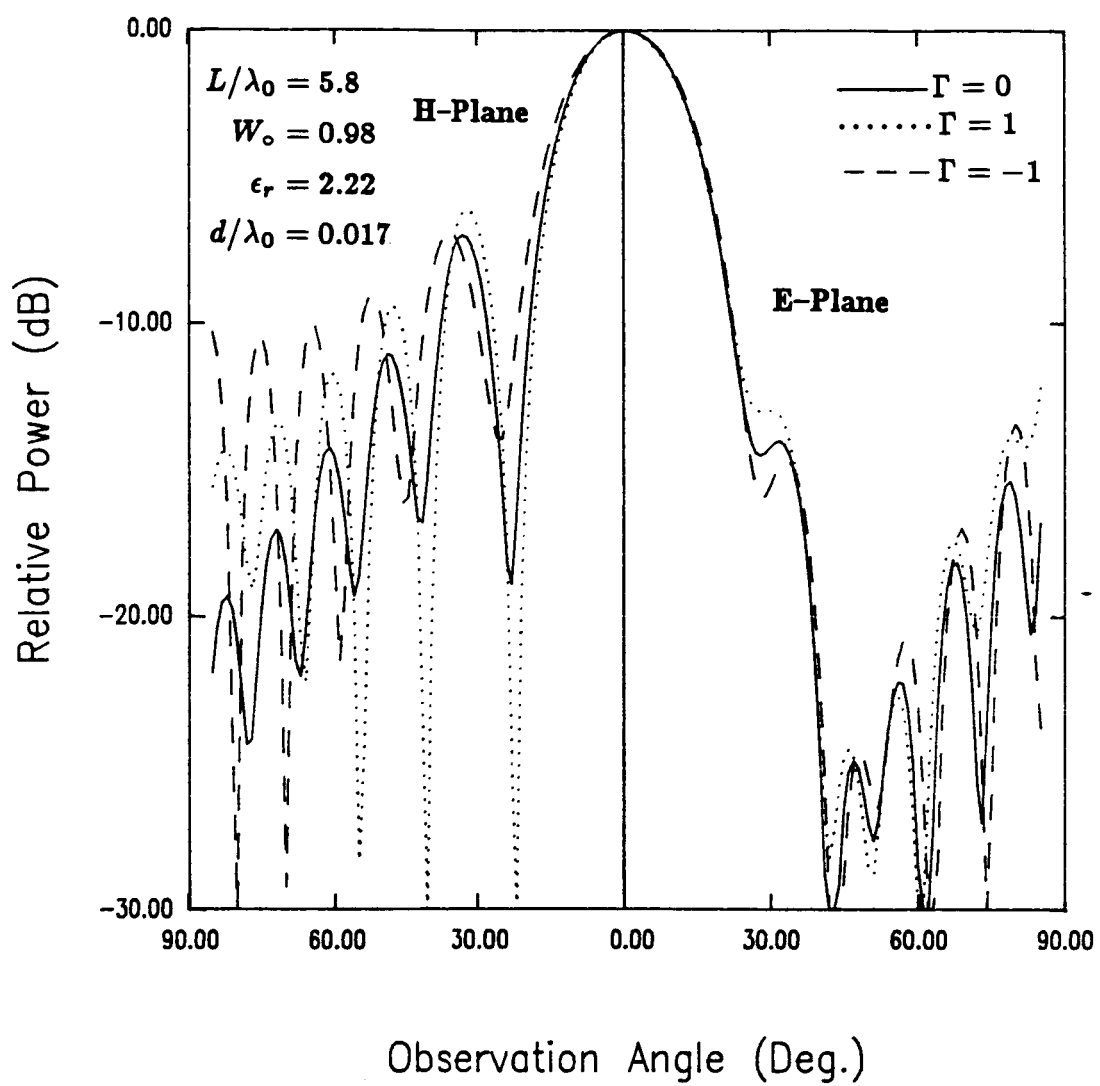
Fig. 4.20 shows the effect of the correction in  $\lambda'$  on the radiation pattern. Patterns are compared with and without the correction factor. The  $-2.7\%$  correction factor results in a 3 dB beamwidth in the H-plane that is about 30% less than the pattern obtained using the uncorrected slot wavelength.

Fig. 4.21. shows the pattern comparison for the CWSA at 8.0 GHz. Corrected slot wavelength was used in the computed pattern. The theory predicts a side lobe level in the H-plane that is about 4 dB below the experimental one. Complete experimental patterns corresponding to Figs. 4.19, and 4.21 are included in Figs. B7, B8 respectively.

**3. Vivaldi.** A Vivaldi antenna is built with an exponential slot taper. The generating equation for the slot width  $W(\zeta)$  is given by

$$W(\zeta) = W_f e^{T\zeta}$$

where  $W_f$  is the slot width at the feed gap,  $\zeta$  is the distance variable measured from the feed gap along the antenna length and  $T$  is the rate at which the exponential curve grows. A Vivaldi antenna was built on a 1.27 cm (1/2-inch) thick styrofoam sheet ( $\epsilon_r \approx 1.05$ ) and using  $W_f = 0.06$  cm,  $T = 0.2$  cm $^{-1}$  and  $L = 19.0$  cm. For this set of parameters,  $W_o = 5.3$  cm. Fig. 4.22 shows the radiation patterns at 10 GHz. At this frequency,  $L = 6.3\lambda_o$  and  $W_o = 1.77\lambda_o$ . For the experimental case,



**Fig. 4.19b** Effect of backward wave on CWSA pattern.

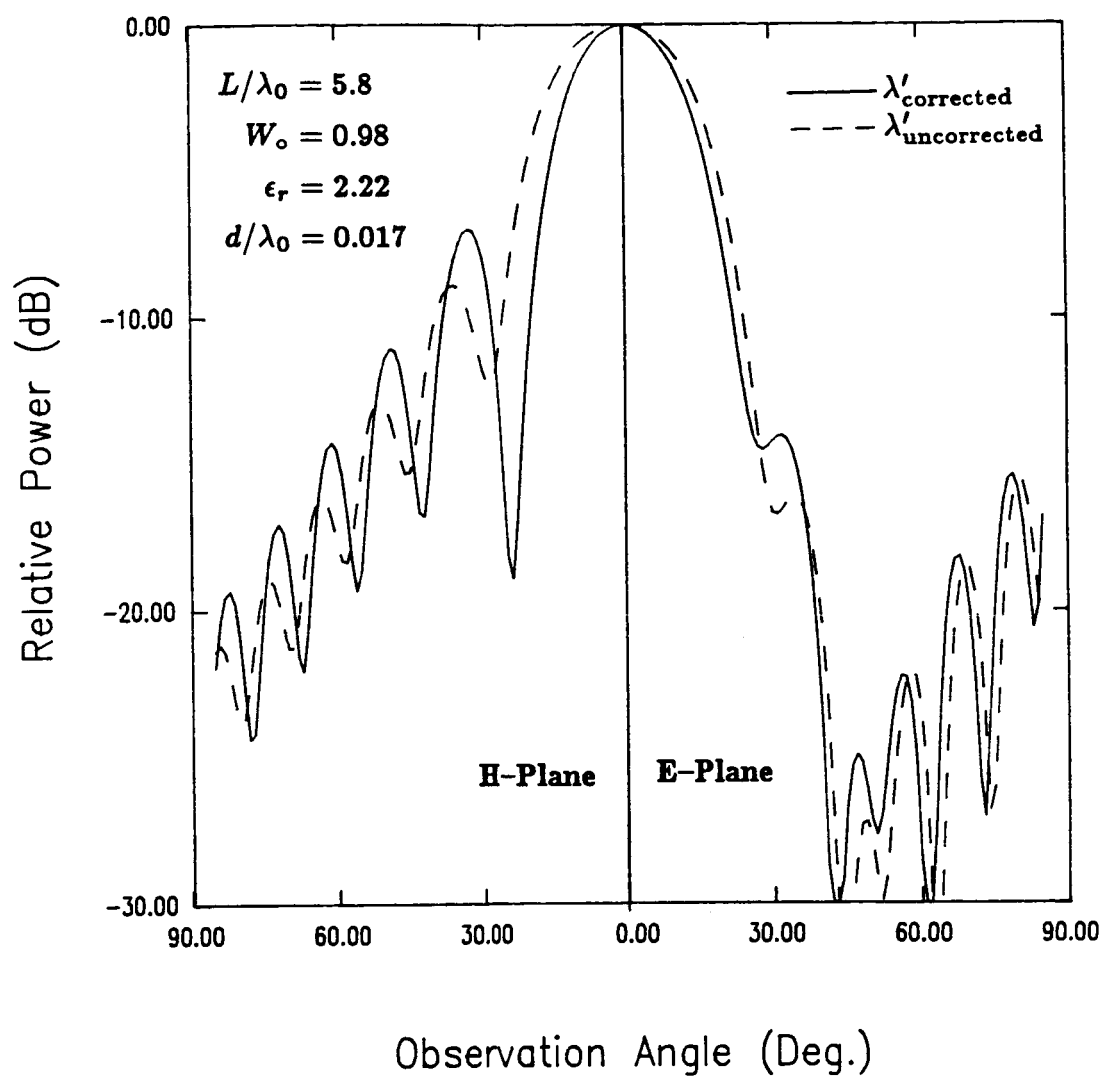


**Fig. 4.20** Computed radiation patterns of CWSA on thin substrate obtained using *corrected* and *uncorrected* slot wavelengths.

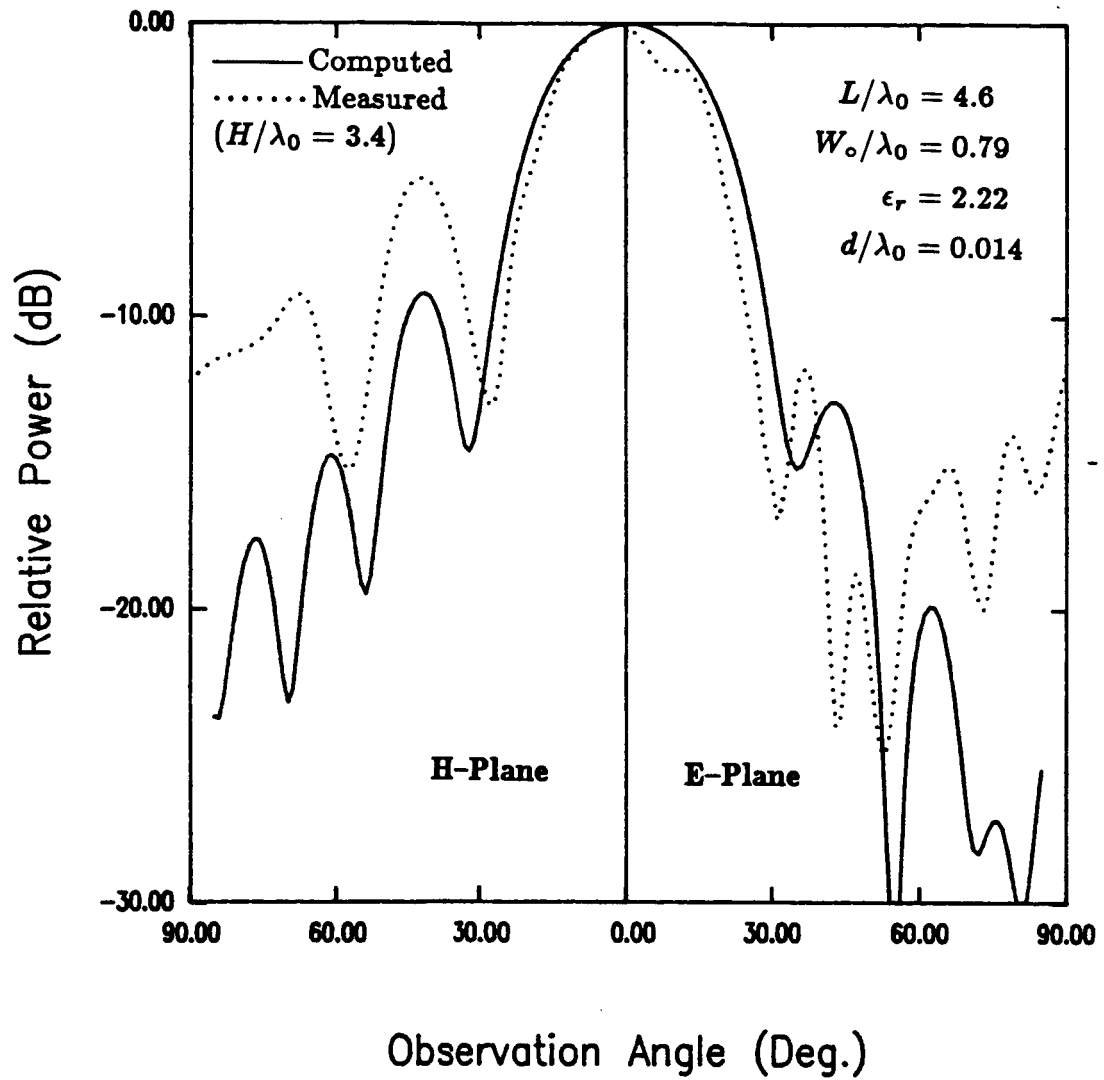


**Fig. 4.21** Measured and computed radiation patterns of CWSA on thin substrate. Frequency = 8 GHz.



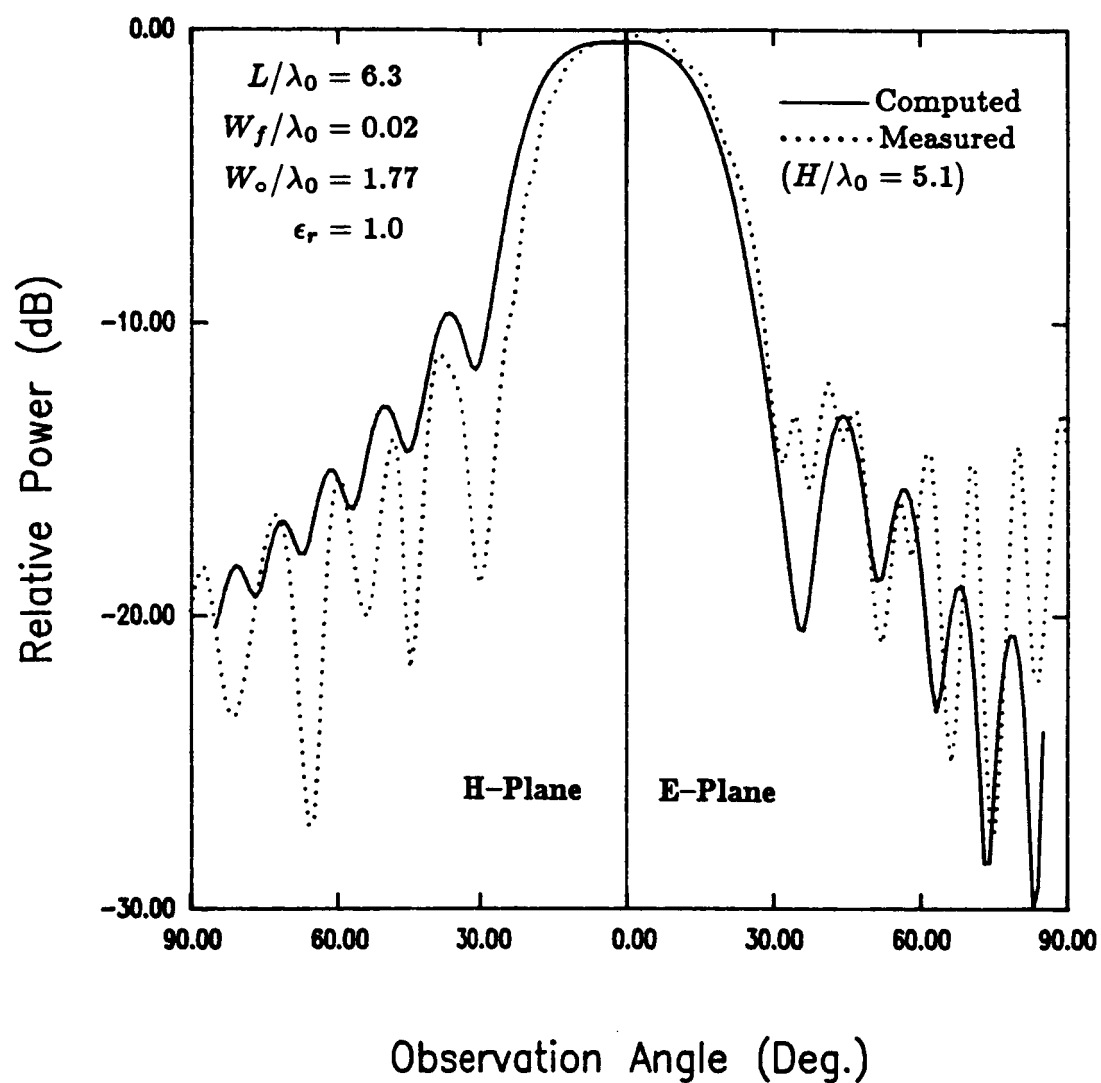


**Fig. 4.22** Measured and computed radiation patterns of Vivaldi antenna on a 1/2-inch styrofoam sheet.

$H = 15.24$  cm. The exponential taper was modeled by the stepped approximation. A value 0.9999 was *assumed* for the slot wavelength in each step and the characteristic impedance was taken to be constant for all the uniform sections. This was done so as to avoid the numerical instability that may have to be incurred if the slot line program is used to compute these parameters. The agreement between the theory and experiment in Fig. 4.22. is fairly good. The main beam as well as the sidelobes are adequately modeled. Complete experimental patterns are shown in Fig. B9.

**4. Use of Curve-Fitted Slot Line Data.** All the patterns in the previous sections were computed using separately generated slot line data. In this section, use of the curve-fitted data, provided in Chapter 3, as an alternative in calculating the patterns is demonstrated. The substrate dielectric constants and their thicknesses are chosen randomly so as to make this numerical experiment unbiased. In each case, pattern computations based on generated slot line data and its curve-fitted counterpart are compared. For the sake of brevity, the former is referred to as computation # 1 and the latter computation # 2.

Figs. 4.23–25 show the computed patterns of CWSA, LTSA and Vivaldi antennas, all having a total length of  $6\lambda_0$  and  $\epsilon_r = 3.5$ ,  $d/\lambda_0 = 0.02$ ,  $W_f = 0.02\lambda_0$ ,  $W_0 = 1\lambda_0$ . In the case of the CWSA,  $L_f = 0.5\lambda_0$ . Each of the three antennas has a different distribution of  $\lambda'$  and  $Z_0$  along the antenna length, owing to the different taper shape. It is seen that computation #1 and computation #2 are indistinguishable in the of CWSA, but slightly displaced in LTSA and Vivaldi. However, the difference between the two is not very appreciable. For this choice of parameters, computation #2 predicts a slightly wider main beam in the latter two. It is interesting to note

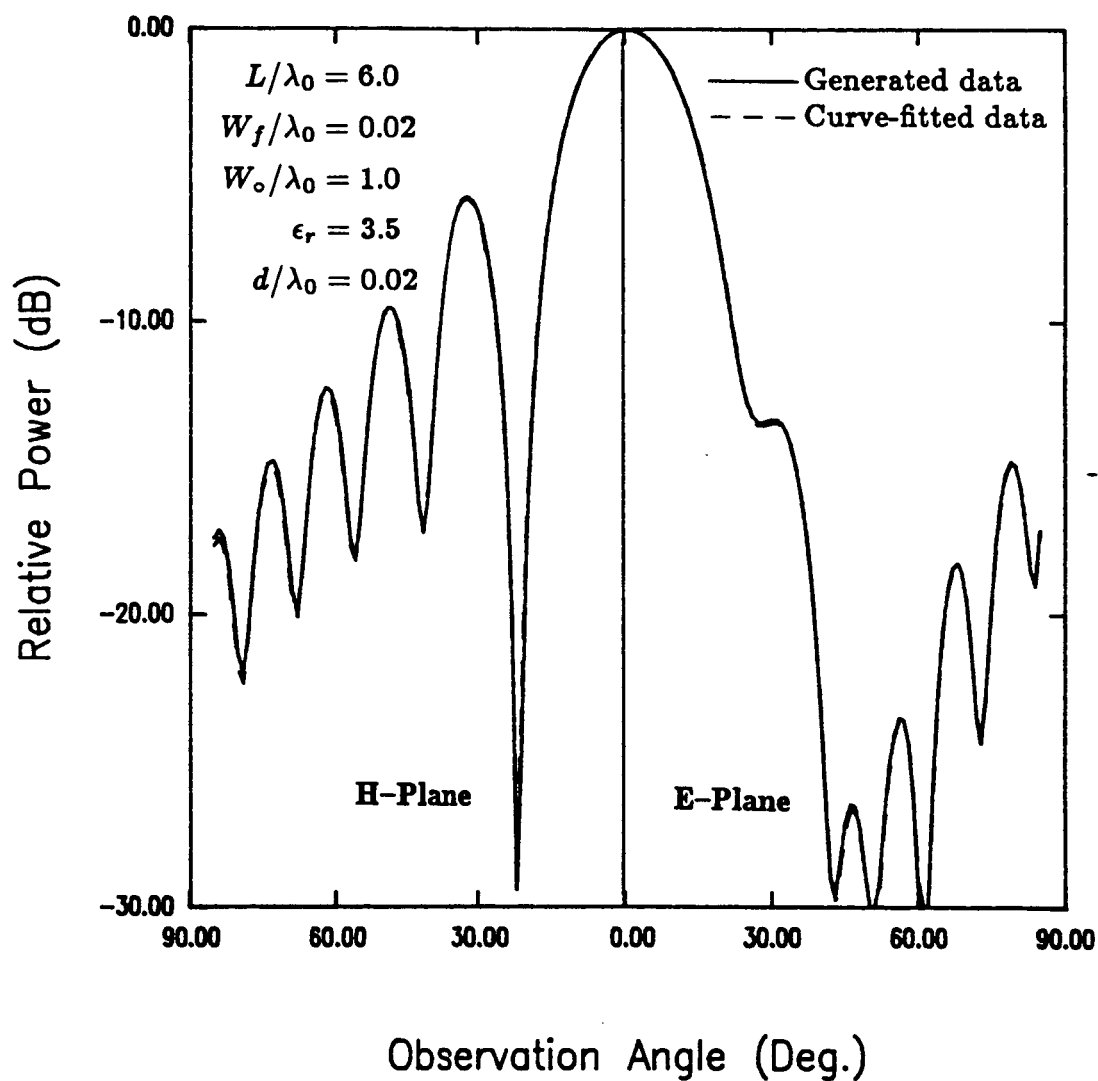


**Fig. 4.23** Computed radiation patterns of CWSA—*generated and curve-fitted* slot line data.

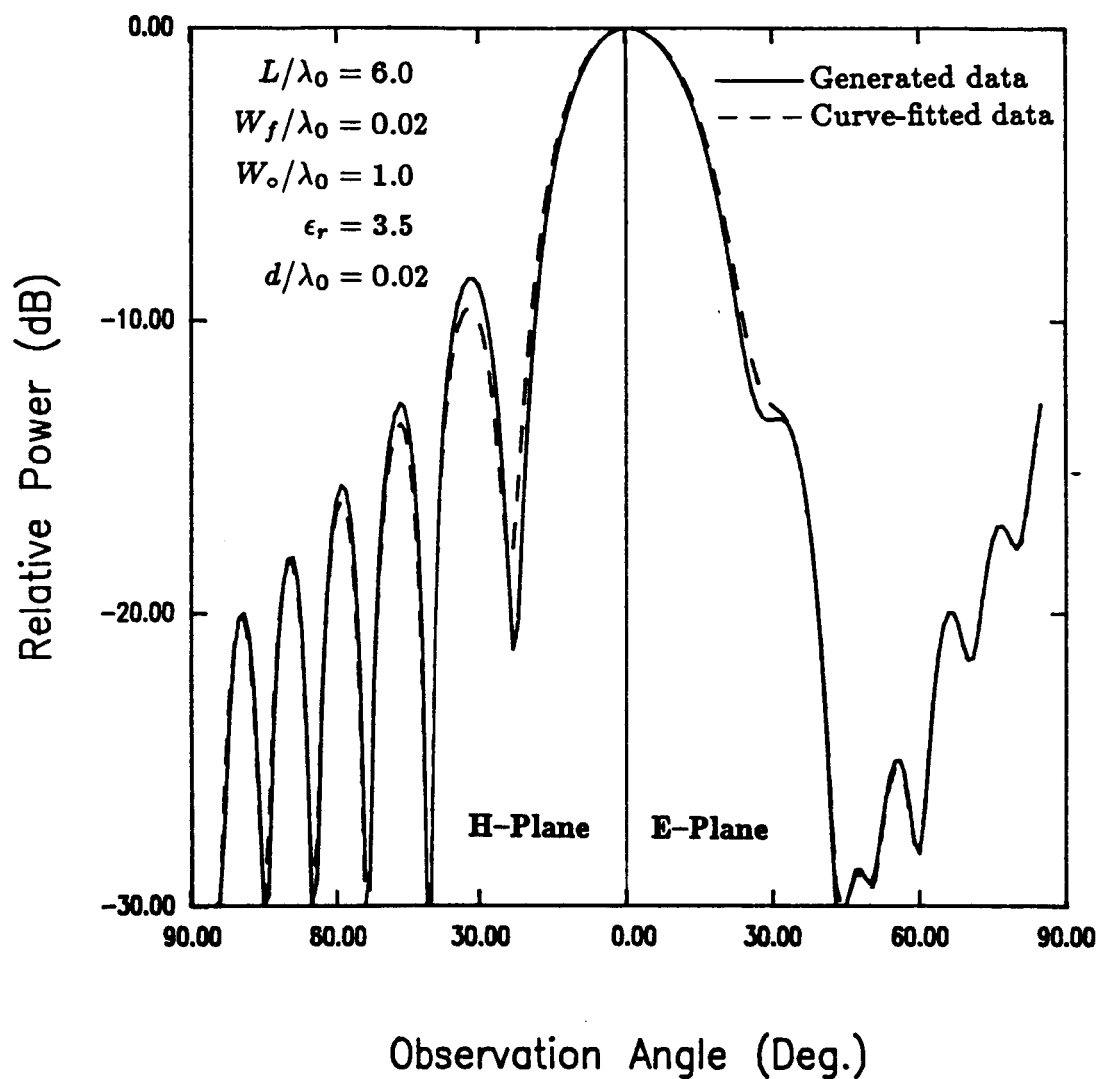


**Fig. 4.24** Computed radiation patterns of LTSA—*generated* and *curve-fitted* slot line data.

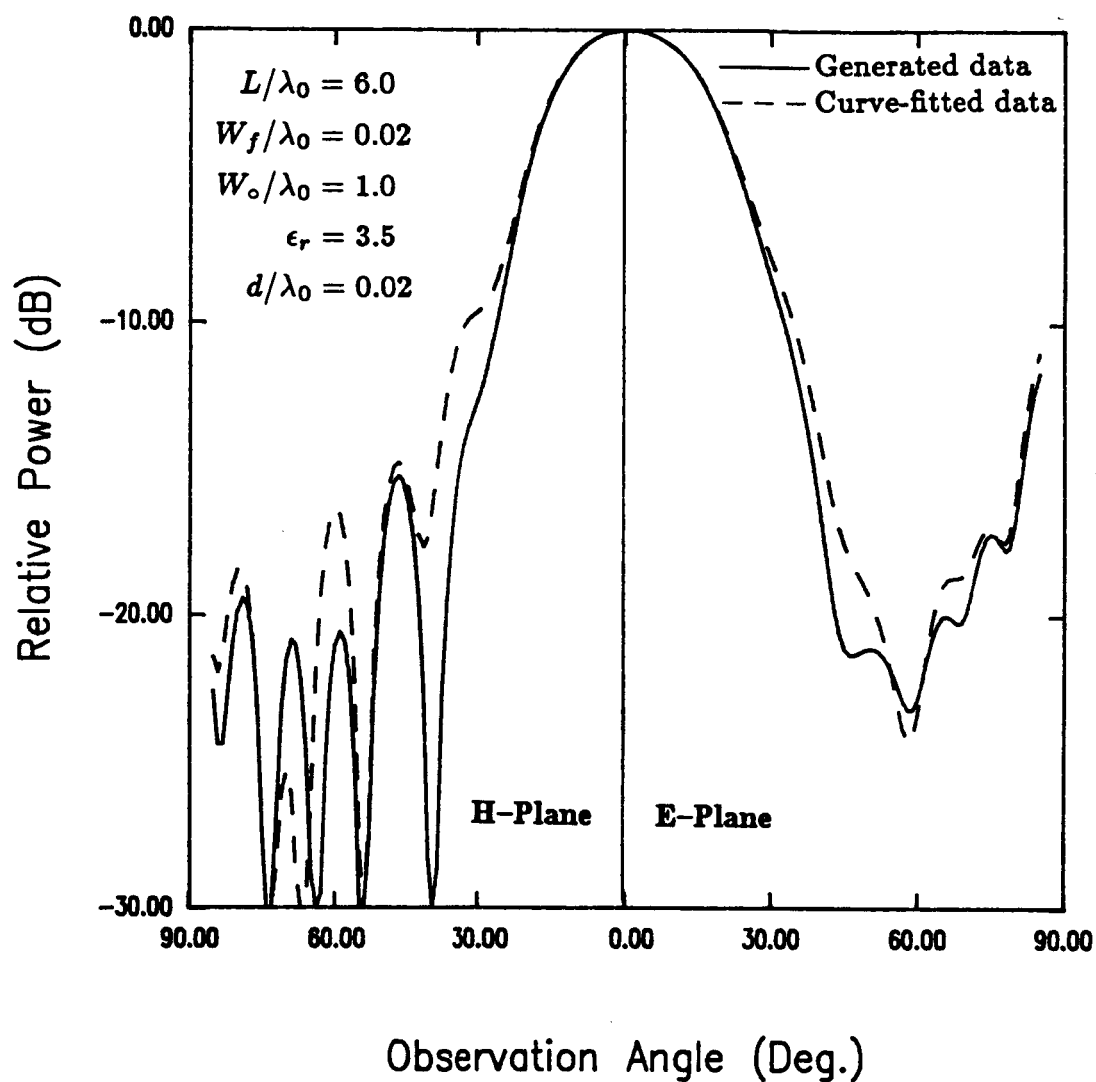


**Fig. 4.25** Computed radiation patterns of Vivaldi—*generated* and *curve-fitted* slot line data.

that the for the same set of physical parameters, the CWSA, LTSA and the Vivaldi have progressively increasing beamwidths and progressively decreasingly sidelobes.

Figs. 4.26–28 show the computed radiation patterns of CWSA, LTSA and Vivaldi antenna, all having a total length of  $50\lambda_0$  and  $\epsilon_r = 5.0$ ,  $d/\lambda_0 = 0.008$ ,  $W_f = 0.02\lambda_0$ ,  $W_0 = 0.9\lambda_0$ .  $L_f = 0.5\lambda_0$  in the case of CWSA. It is seen that computation #2 agrees very closely with computation #1.

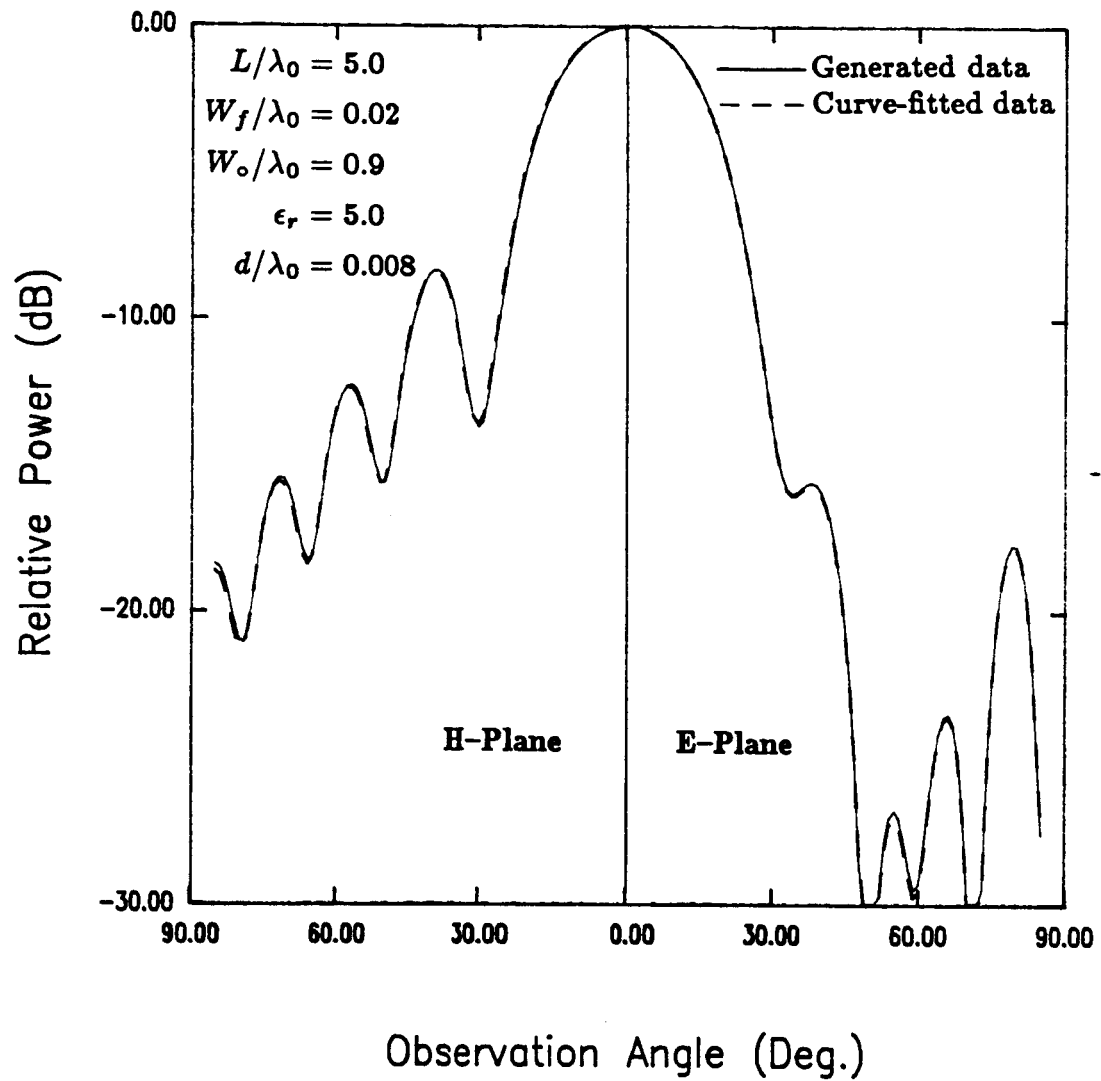


**Fig. 4.26** Computed radiation patterns of CWSA—*generated* and *curve-fitted* slot line data.

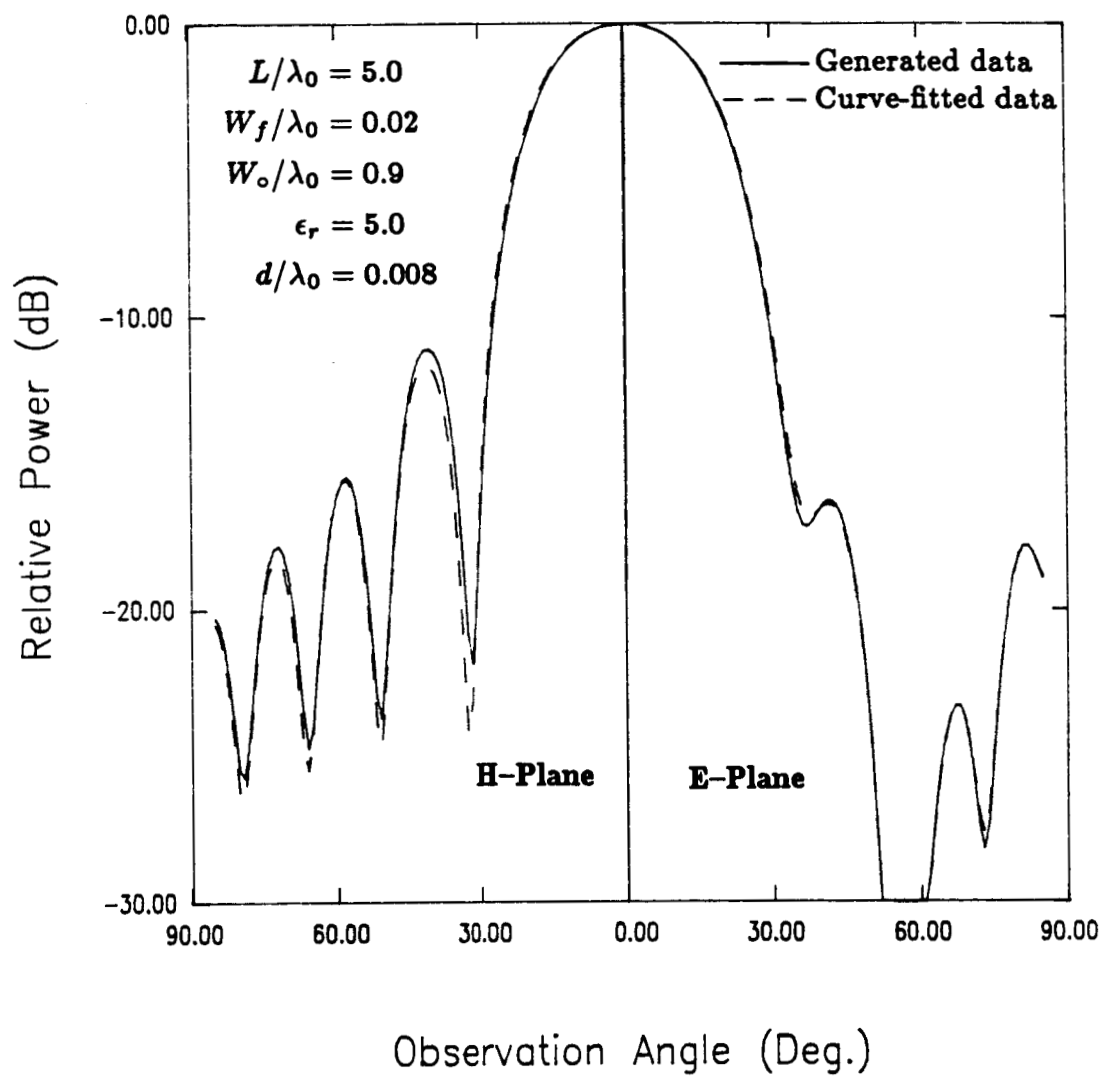


**Fig. 4.27** Computed radiation patterns of LTSA—*generated* and *curve-fitted* slot line data.



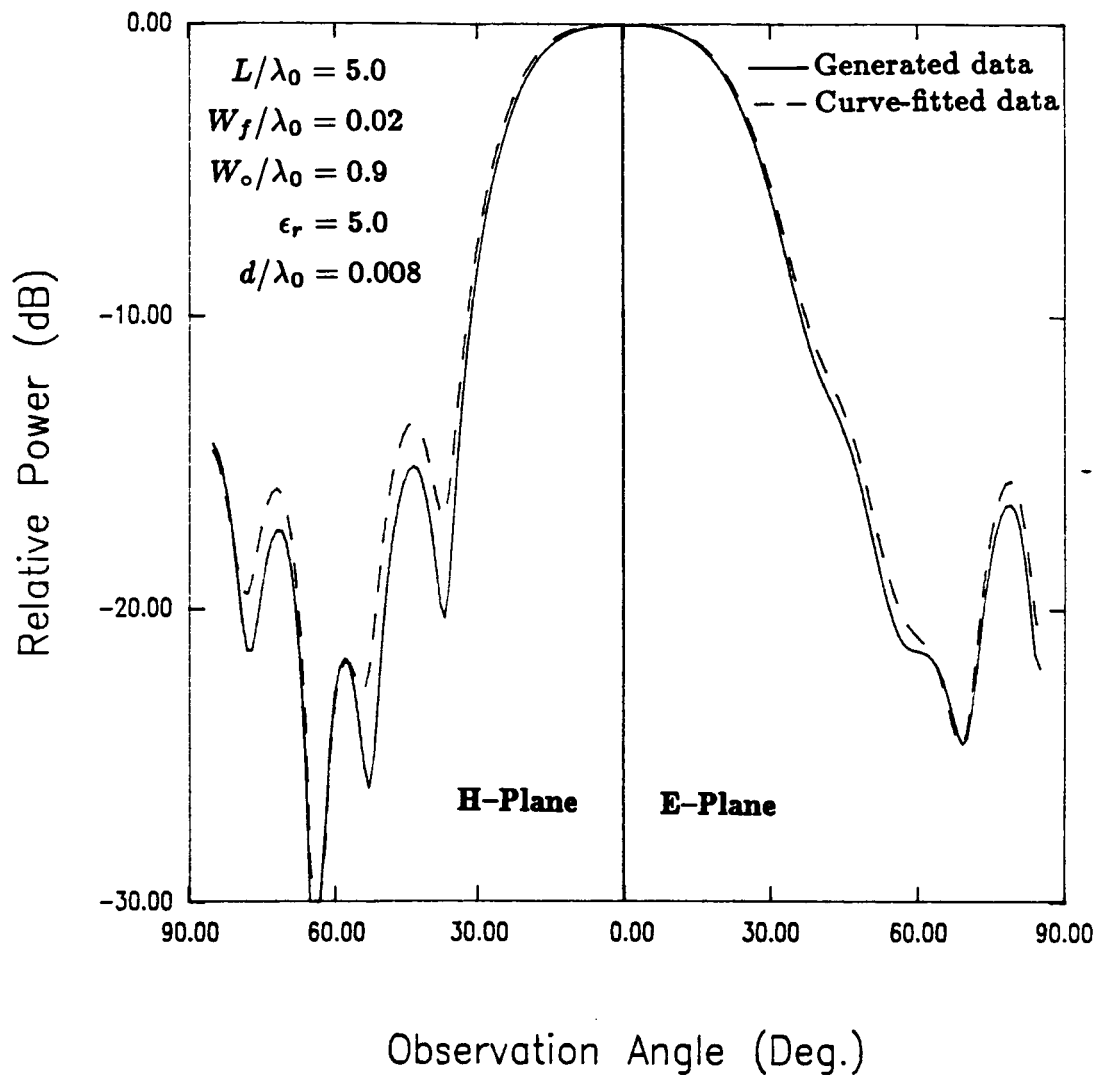


**Fig. 4.28** Computed radiation patterns of Vivaldi—*generated* and *curve-fitted* slot line data.

## CHAPTER 5

### EFFECT OF LATERAL TRUNCATION ON THE ANTENNA PATTERN

The foregoing theory presented in Chapter 4 is valid for antennas with an electrically large  $H$ . Ideally the theory is applicable when  $H \rightarrow \infty$ . It has been shown in the previous chapter by comparing with experiment that the theory predicts reasonably well for cases with  $H$  greater than approximately  $3\lambda_0$ . However, it has been observed experimentally that the pattern exhibits some interesting features as the antenna is truncated laterally (i.e.,  $H$  made electrically small). In particular, lateral truncation results in an E-plane beamwidth that is, in most cases, considerably narrower than the one obtained using an antenna with a large  $H$ . In this chapter, results are presented for the pattern dependence on the lateral dimension  $H$  of the antenna. Results presented are mostly experimental. However, preliminary theoretical results for treating the truncation effects for the special case of an air-dielectric LTSA are also presented.

#### 5.1 Experimental Results

Figs. 5.1–5.3 show the radiation patterns of an LTSA built on a 1-inch styrofoam sheet, and with  $L = 24$  cm,  $W_f = 1.5$  mm,  $W_o = 5.1$  cm ( $= 2''$ ), and  $f = 9$  GHz. At this frequency,  $L = 7.2\lambda_0$ , and  $W_o = 1.53\lambda_0$ . The lateral dimension  $H$  of the antenna was successively decreased over the range  $4.6 \geq H/\lambda_0 \geq 0.76 (= 0.5W_o/\lambda_0)$  and in each case the pattern measured. It is seen from the plots that beam shape is being affected considerably as the height is varied. In particular, a very narrow E-plane main beam is obtained when  $H = 5.1$  cm. There is, however, a slight broadening of the H-plane beam (compared to the one obtained with a larger  $H$ ).

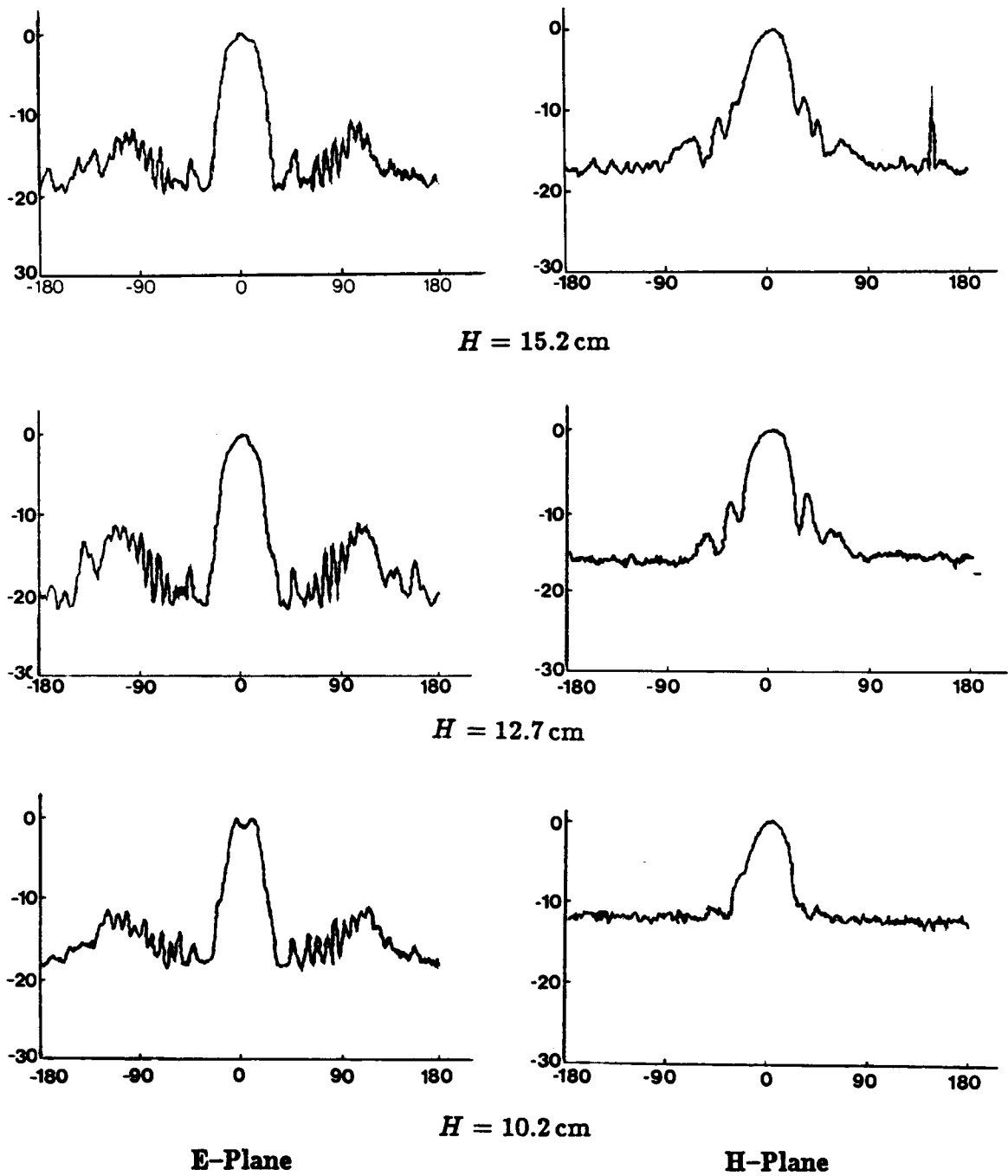


**Fig. 5.1** Measured radiation pattern of LTSA on a 1-inch styrofoam sheet as a function of  $H$ . ( $L = 24 \text{ cm}$ ,  $W_f = 1.5 \text{ mm}$ ,  $W_o = 5.1 \text{ cm}$ ,  $f = 9 \text{ GHz}$ )

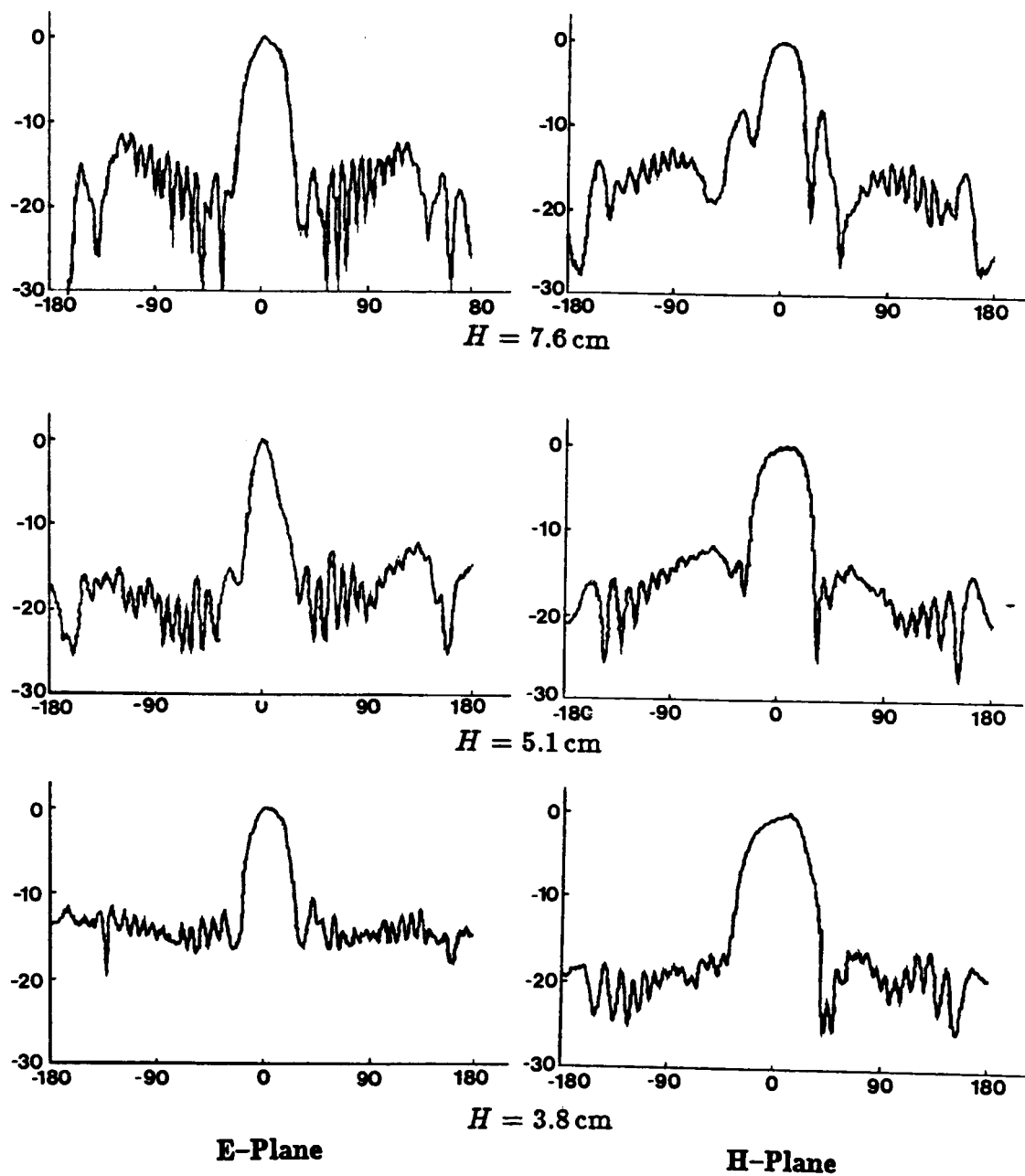


**Fig. 5.2** Measured radiation pattern of LTSA on a 1-inch styrofoam sheet as a function of  $H$ . ( $L = 24$  cm,  $W_f = 1.5$  mm,  $W_o = 5.1$  cm,  $f = 9$  GHz)

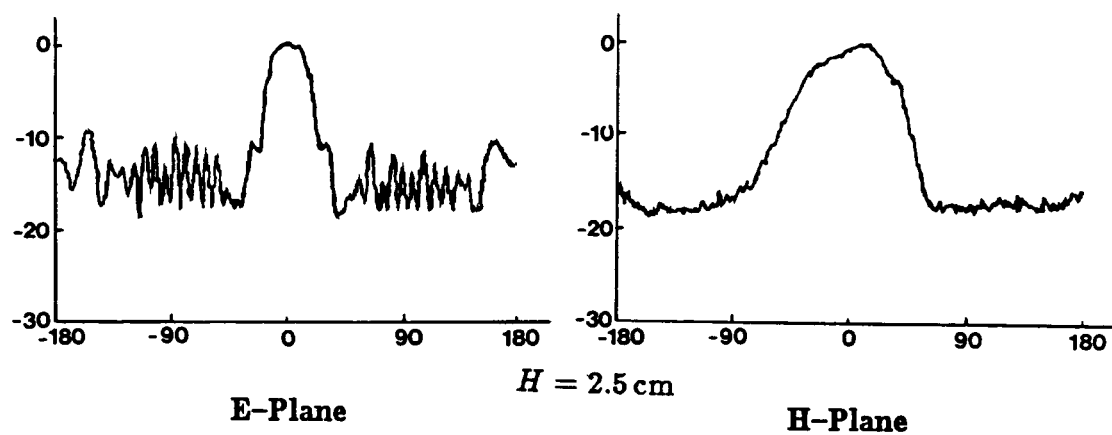


**Fig. 5.3** Measured radiation pattern of LTSA on a 1-inch styrofoam sheet as a function of  $H$ . ( $L = 24 \text{ cm}$ ,  $W_f = 1.5 \text{ mm}$ ,  $W_o = 5.1 \text{ cm}$ ,  $f = 9 \text{ GHz}$ )

Figs. 5.4–5.6 illustrate the truncation effects for a  $\epsilon_r = 2.22$  antenna. Patterns are shown for an LTSA with  $L = 12.6$  cm,  $W_f = 1$  mm,  $W_o = 2.2$  cm,  $d = 20$  mils, and  $f = 8$  GHz. Once again it is seen that the beam shape changes significantly as  $H$  is varied.

Experiments performed on other LTSAs and CWSAs by varying the antenna height and keeping all other parameters fixed have indicated the same trend. It is clear that the theory presented in Chapter 4 is not adequate to predict the pattern dependence on the lateral dimension of the antenna. To study these effects, the simpler case of an air-dielectric LTSA is presently being explored.

## 5.2 Theoretical Studies

This section presents results on the theoretical studies performed so far to account for the pattern dependence on the lateral dimension  $H$  of an air-dielectric LTSA. The problem is formulated using the well known moment-method and solution is sought for the total electric surface current flowing on the metal plates that constitute the antenna.

At a first glance, it may appear that a high-frequency ray theory such as GTD [8] may be used in conjunction with the aperture-field modeled in Chapter 4. However, a closer look would indicate that the ray-theory is not adequate to explain the severe changes that occur in the main-beam region as  $H$  is decreased. High frequency diffraction caused by the edges that are formed as a result of lateral truncation do not influence the main beam region as would be clear from a simple ray tracing. It is felt at this stage that the truncation effect is more of a resonance phenomenon occurring in the lateral direction and may be modeled by the moment-method.

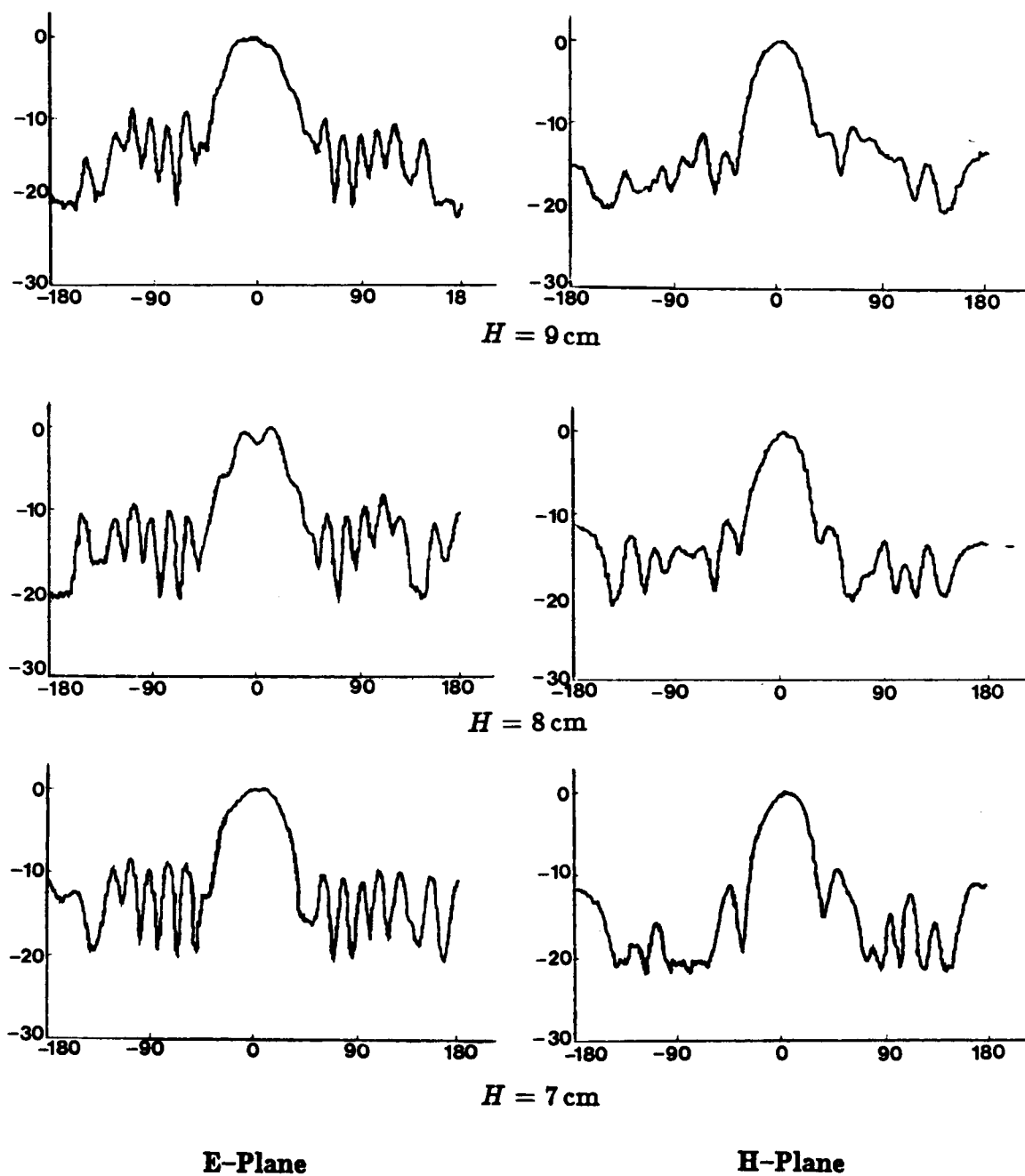


**Fig. 5.4** Measured radiation pattern of LTSA on Duroid substrate as a function of  $H$ . ( $L = 12.6 \text{ cm}$ ,  $W_f = 1 \text{ mm}$ ,  $W_o = 2.2 \text{ cm}$ ,  $\epsilon_r = 2.22$ ,  $d = 20 \text{ mils}$ ,  $f = 8 \text{ GHz}$ )

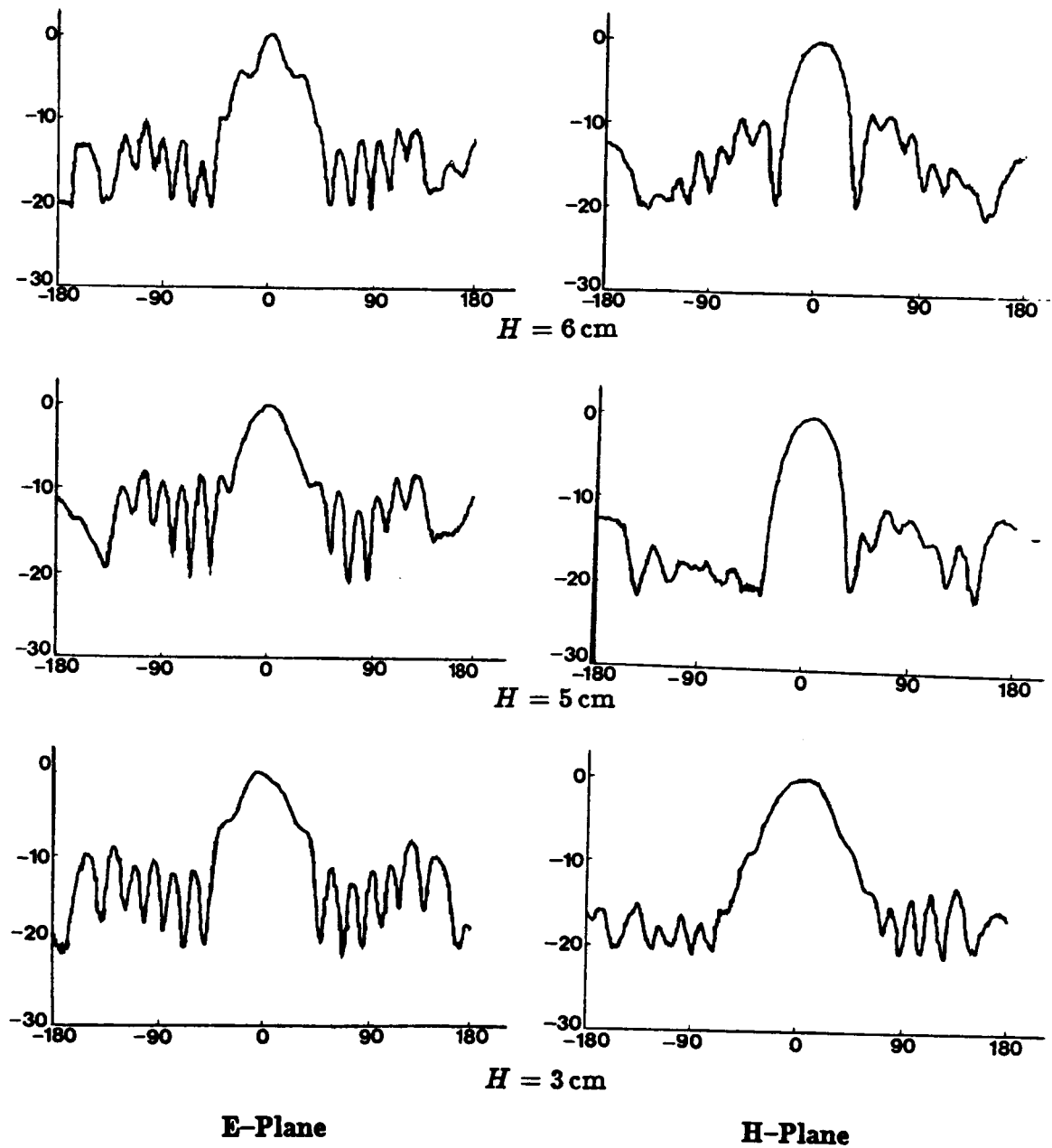


**Fig. 5.5** Measured radiation pattern of LTSA on Duroid substrate as a function of  $H$ . ( $L = 12.6 \text{ cm}$ ,  $W_f = 1 \text{ mm}$ ,  $W_o = 2.2 \text{ cm}$ ,  $\epsilon_r = 2.22$ ,  $d = 20 \text{ mils}$ ,  $f = 8 \text{ GHz}$ )



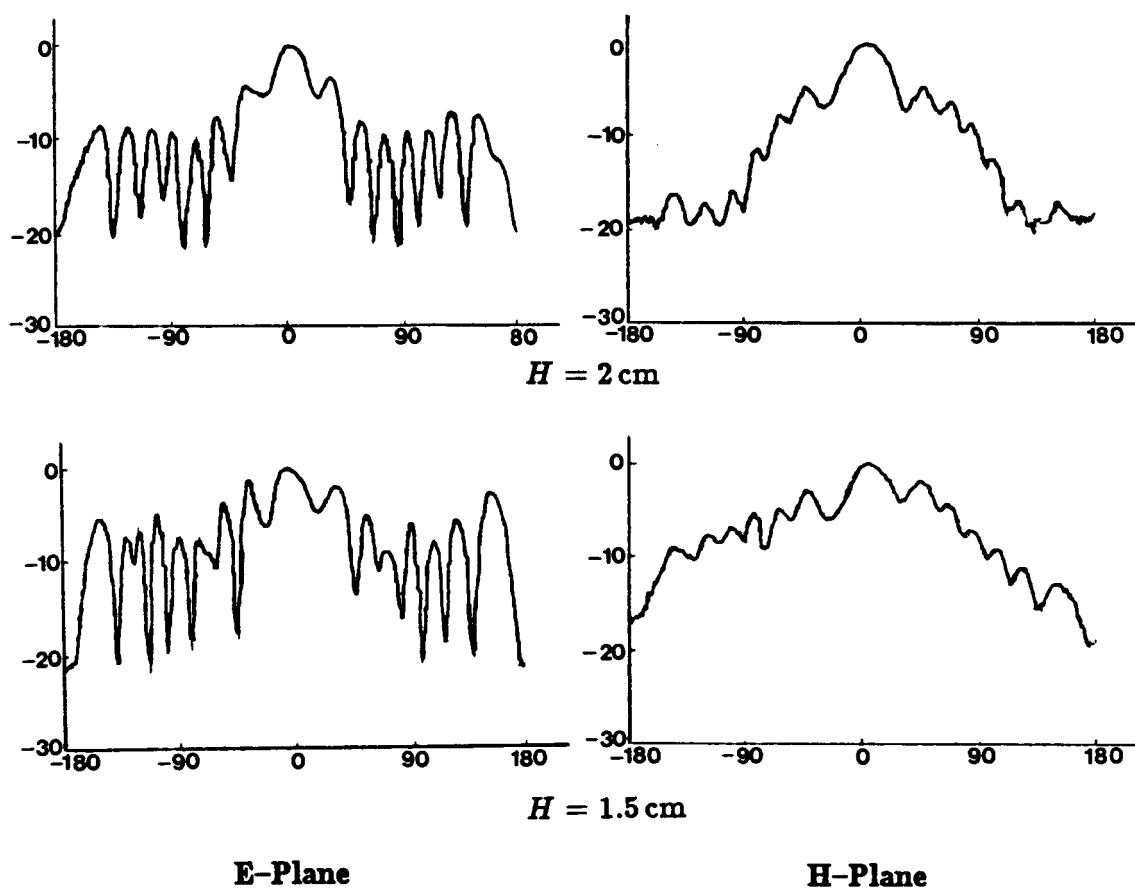


**Fig. 5.6** Measured radiation pattern of LTSA on Duroid substrate as a function of  $H$ . ( $L = 12.6 \text{ cm}$ ,  $W_f = 1 \text{ mm}$ ,  $W_o = 2.2 \text{ cm}$ ,  $\epsilon_r = 2.22$ ,  $d = 20 \text{ mils}$ ,  $f = 8 \text{ GHz}$ )

C-2.

To study the problem using the moment-method, a slightly different geometry as shown in Fig. 5.7 is considered. As opposed to the trapezoidal plates present in a regular LTSA shown in Fig. 2.1, the modified geometry consists of two skewed rectangular plates. This geometry facilitates the use of rectangular subsectioning, the theory for which is well developed in [23] and is shown to result in a computationally efficient moment-method matrix. This is particularly useful in view of the fact that large matrices are expected to result during the moment-method modeling of the LTSA. The computer program developed in [23] is used here to compute the elements of the impedance matrix. The source was modeled by means of an infinitesimal current source placed at the antenna apex as shown in Fig. 5.7. This simple source model should be adequate as far as the radiation patterns are concerned. An alternate source model consisting of an ideal voltage source connected across the two plates by means of bent short-wire segments was also tried and found to yield identical pattern results as the former.

Fig. 5.8 shows the computed pattern of a modified air-dielectric LTSA with  $L = 3\lambda_0$ ,  $H' = 0.75\lambda_0$ , and  $2\gamma = 11.5^\circ$ . Four segments along the height and fifteen segments along the length were chosen on each plate for the computations. Both  $J_x$  and  $J_y$  were included in the calculations. As a comparison, the measured pattern for the same geometry is shown in Fig. 5.9. It is seen the two differ considerably in the H-plane. The maximum in the H-plane in the computed pattern occurs at an angle other than the end-fire direction. Such a large offset is not observed in the measured pattern. It was found that in a number of other computations, the computed pattern always yielded a H-plane beam that was skewed off the end-fire direction that has not been noticed in the measured pattern. It was found that

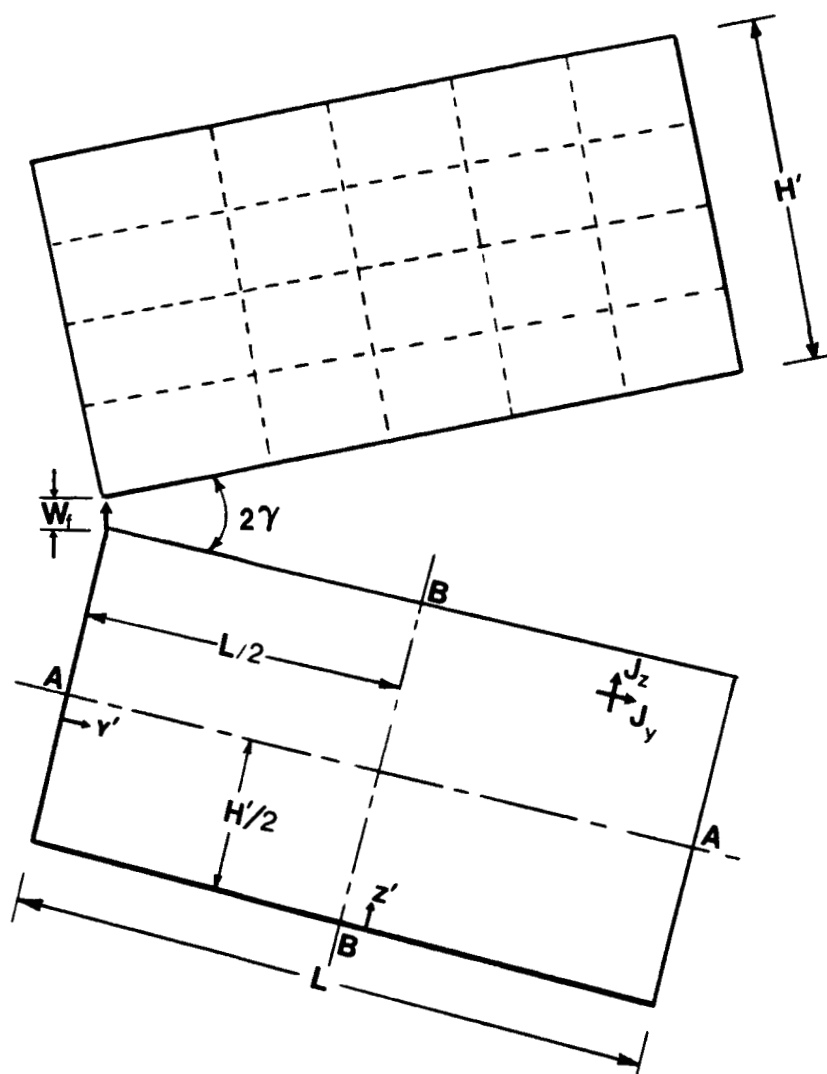
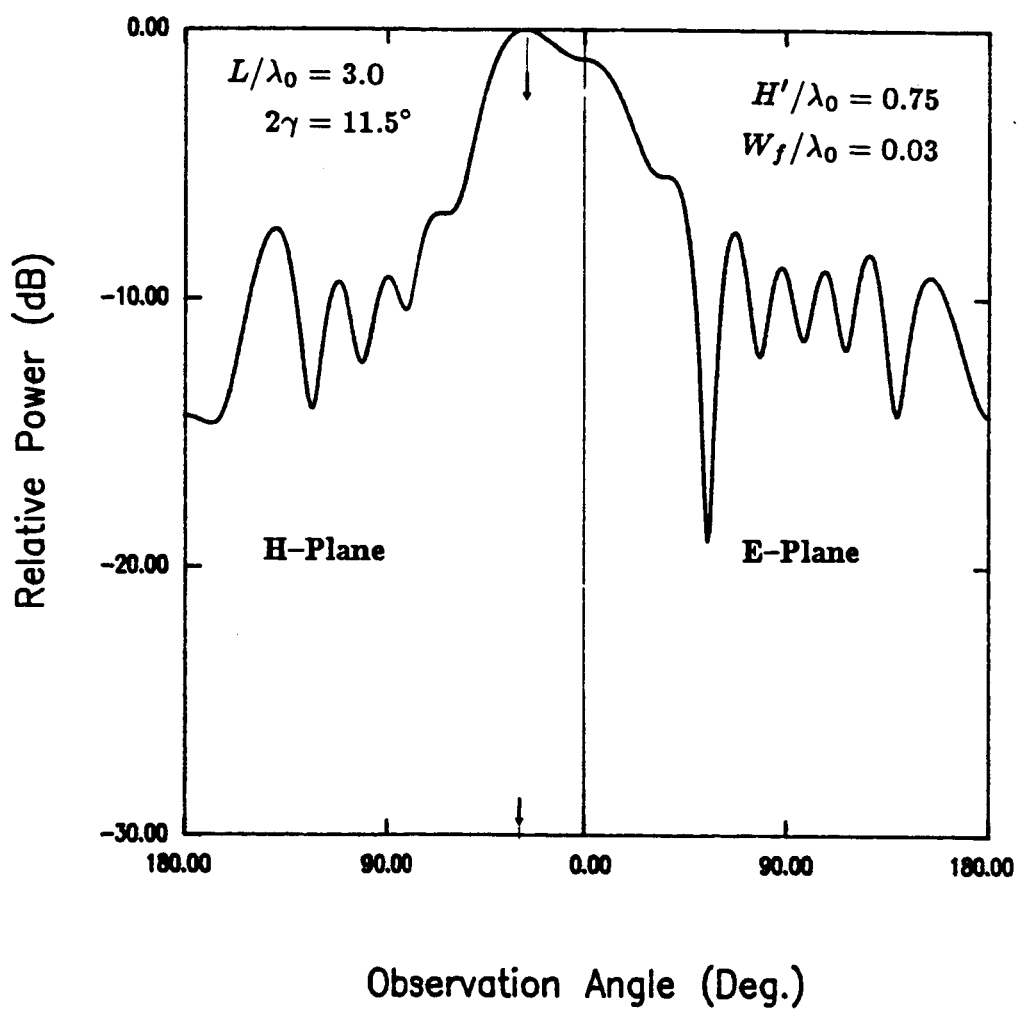
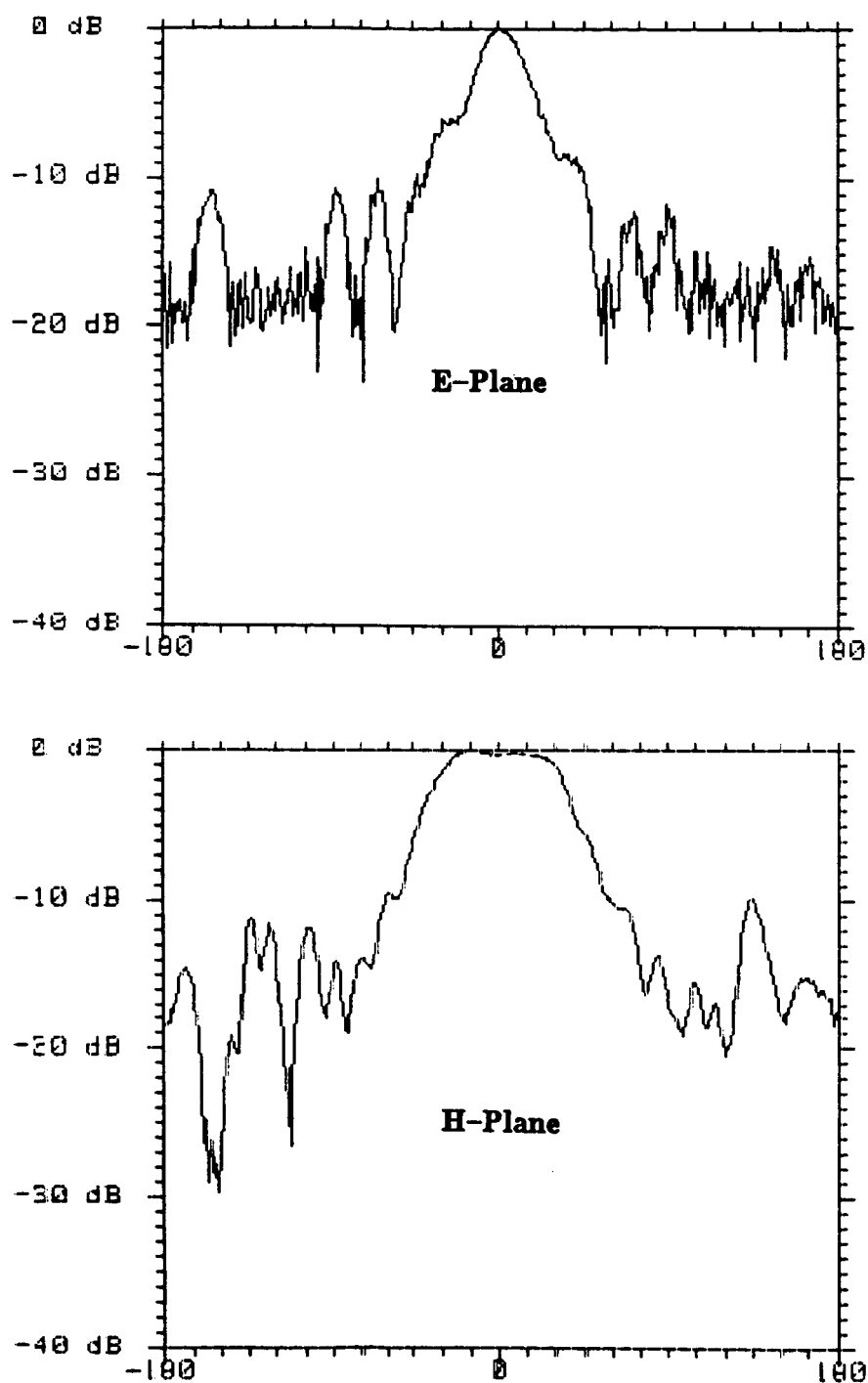


Fig. 5.7 Geometry of rectangular plates.



**Fig. 5.8** Computed radiation pattern of antenna.



**Fig. 5.9** Measured radiation pattern of antenna.  
 ( $L = 15$  cm,  $H' = 3.75$  cm,  $2\gamma = 11.5^\circ$ ,  $W_f = 1.3$  mm)

the cause of this is due to a phase error in the current distribution that incorrectly results in a fast wave flowing along the plates.

Figs. 5.10 and 5.11 show the current distributions along the two principal cuts (cf. Fig. 5.7) of the rectangular plate. The phase of  $J_x$  is in steps because the phase is constant across the basis functions. It is seen from Fig. 5.10 that the code incorrectly predicts a fast wave along the plate and one that is nonlinear (i.e., variable wavelength). This phase error makes the antenna look like a leaky-wave antenna, resulting in a non-end-fire main beam in the H-plane. The impedance matrix in the moment method calculations should yield a Toeplitz symmetric matrix when structure is segmented uniformly and when the same type of basis functions are employed in each subsection. Uniform segmentation and the same type of basis functions in each subsection were employed in the present computations. However, the code failed to yield toeplitz matrix. In particular, the code was tested to compute the impedance elements of a  $0.5\lambda_0 \times 0.5\lambda_0$  square plate. The plate was subdivided into 3 subsections along the length and 3 subsections along the breadth. The mode layout is shown in Fig. 5.12. The total number of plate modes are 12 as indicated in the figure. It was found that  $|Z_{8,1}|$  and  $|Z_{10,1}|$  differed by as much as 6%. Some more elements exhibited the same unsymmetry, although the magnitude of the difference was not as high. It is not yet known whether this could result in the phase error observed in the current distribution. Further studies are needed to explain the cause of this error.

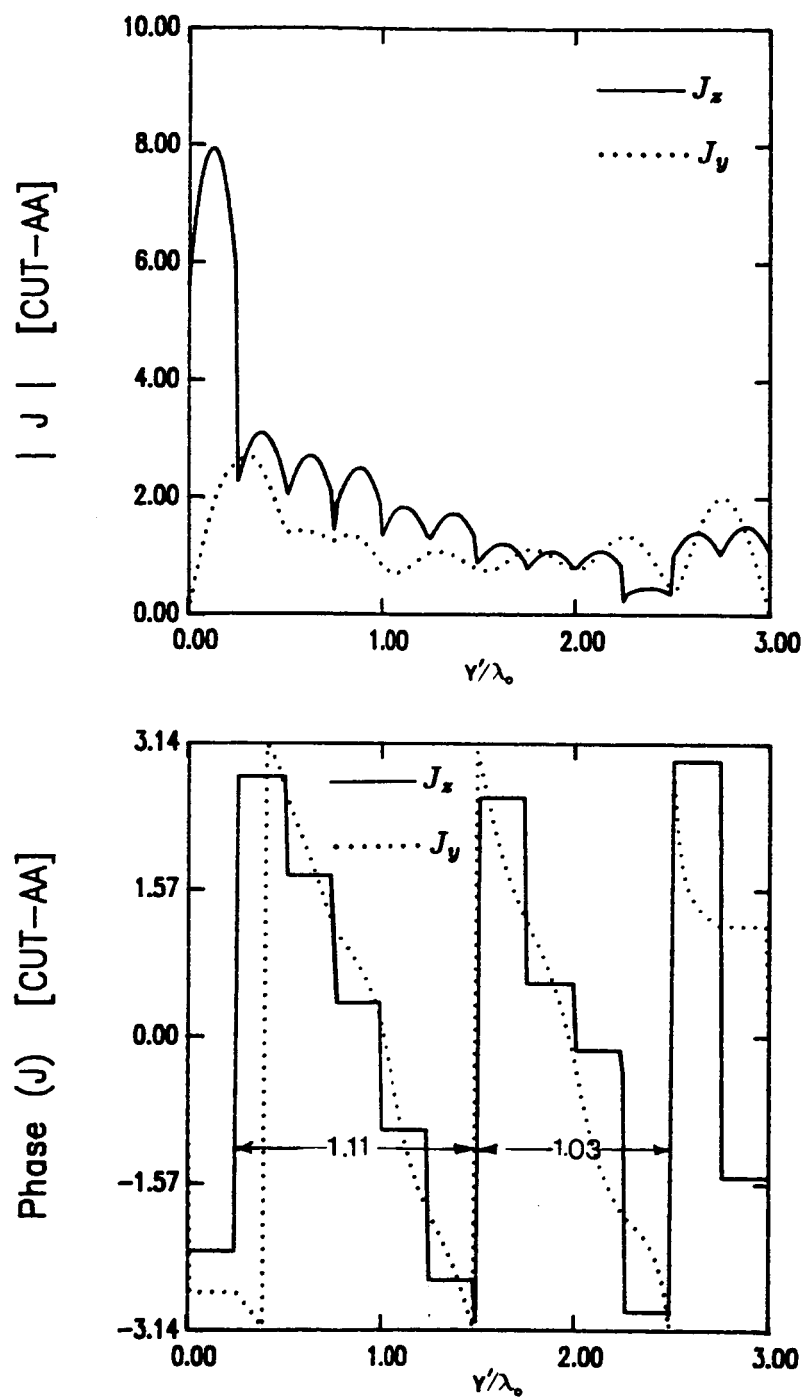


Fig. 5.10 Magnitude and Phase of current (*cut-AA*).

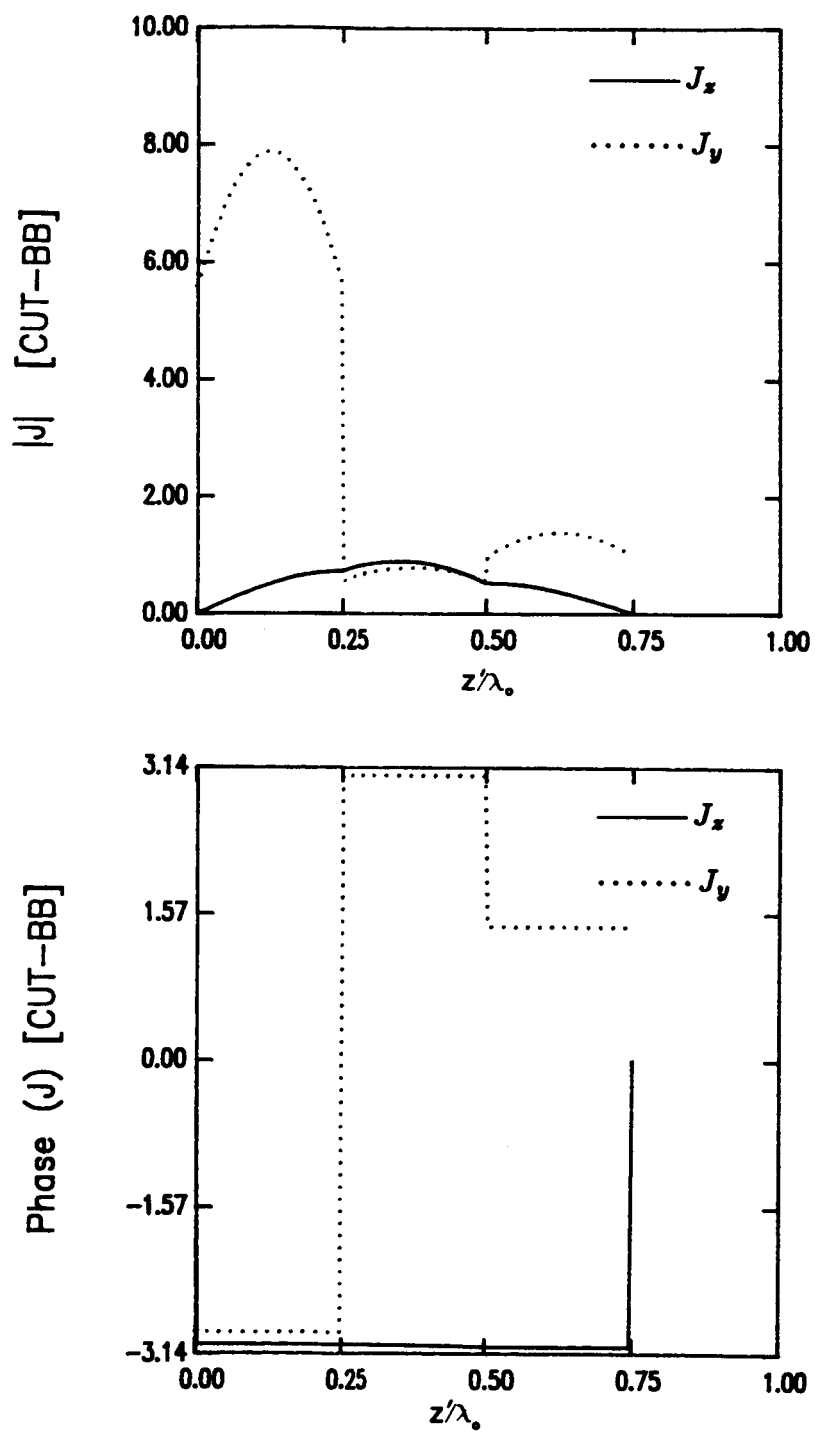
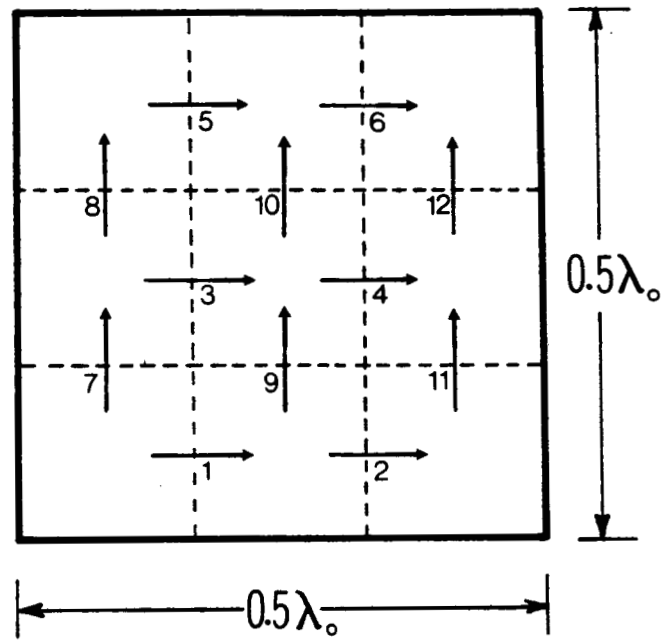


Fig. 5.11 Magnitude and Phase of current (*cut-BB*).





**Fig. 5.12** Mode Layout on  $0.5\lambda_0 \times 0.5\lambda_0$  square conducting plate.

## CHAPTER 6

### CONCLUSION

A theoretical model for the tapered slot antenna is presented. The model is valid for any smooth taper of the slot. The problem is solved by modeling the slot electric field and using the half-plane Green's function to compute the far-fields. The aperture field is obtained by affecting a stepped approximation to the continuous taper and utilizing the uniform wide slot line data. The uniform wide slot line is solved by the spectral Galerkin's technique and closed form expressions are developed for the slot wave length and the slot characteristic impedance.

Numerous comparisons with measurement are made to demonstrate the versatility of the model in treating an arbitrary slot taper. In particular, results are presented for a Linearly Tapered Slot Antenna (LTSA), Constant Width Slot Antenna (CWSA), and an exponentially tapered slot antenna (the Vivaldi). The stepped approximation is validated for the special case of an air dielectric LTSA (TEM-LTSA) by comparing the patterns against a more rigorous model.

The model predicts reasonably good results for thin as well as thick low- $\epsilon_r$  substrates. The model also gives sufficiently accurate results for thin and high- $\epsilon_r$  substrates. It is shown that to predict accurate pattern results, the slot wavelength for thin and low- $\epsilon_r$  substrates must be found with an accuracy better than 2.5% presently obtainable with the spectral Galerkin's technique. Comparison with experiment have been shown for substrate thicknesses up to  $0.06\lambda_0$  for the low- $\epsilon_r$  case. The highest  $\epsilon_r$  for which results are presented was  $\epsilon_r = 10.5$ . The maximum substrate thickness considered for this case was  $0.0085\lambda_0$ . Favorable comparison with experiment has been shown for antenna lengths between  $3.4 \leq L/\lambda_0 \leq 6.1$  and for

flare angles between  $8^\circ \leq 2\gamma \leq 21^\circ$  (in the case of LTSAs). It is however felt that the model could also be used for longer antenna lengths, although slight errors in the slot wavelength could result in larger errors in the pattern shapes. It is shown that the model successfully treats various slot taper shapes such as constant width, linear taper, and exponential taper. It is shown that curve-fitted slot line data could be used in the pattern computations as an alternative to the time-consuming process of generating the data in each uniform section in the stepped approximation. The model is ideally valid for an antenna with an infinite lateral extent. Good results are, however, obtained when the lateral dimension (i.e., height) of the antenna is at least 3 wavelengths long. It is, however, shown experimentally that narrower E-plane beamwidths are obtainable when an antenna having a smaller height is used. Theoretical efforts to treat the special case of air-dielectric, finite-height LTSA are presented. Further studies in this regard are needed.

## APPENDIX A

### EFFECT OF ADHESIVE ON SLOT WAVELENGTH

In this section, an expression is given for the change in slot wavelength due to the presence of a thin layer of adhesive (assumed to be a lossless dielectric) between the metal and the dielectric substrate of a uniform slot line. The expression given is based on a perturbation analysis, similar to the one performed in [17].

Notation:

$\lambda_0$  = free space wavelength.

$$k_0 = \frac{2\pi}{\lambda_0}$$

$\lambda'$  = guide wavelength of slot line.

$$k_s = \frac{2\pi}{\lambda'}$$

$\Delta\lambda'$  = change in slot wavelength due to the presence of adhesive.

$\epsilon_r^s$  = dielectric constant of substrate.

$\epsilon_r^a$  = dielectric constant of adhesive.

$$\delta\epsilon_r = \epsilon_r^a - \epsilon_r^s$$

$d$  = thickness of substrate.

$t$  = thickness of adhesive.

$W$  = slot width.

$Z_0$  = characteristic impedance of slot line based on power, voltage definition.

$\eta_0$  = intrinsic impedance of free space  $\approx 120\pi$  ohms.

$\alpha$  = transform variable. Also the variable of integration.

$$\gamma_1^2 = \alpha^2 + k_s^2 - k_0^2$$

$$\gamma_2^2 = \alpha^2 + k_s^2 - \epsilon_r^s k_0^2$$

When  $t/d \ll 1$ , it can be shown that  $\Delta\lambda'/\lambda'$  is given by

$$\frac{\Delta\lambda'}{\lambda'} = -\delta\epsilon_r \left( \frac{\lambda'}{\lambda_0} \right) \left( \frac{t}{W} \right) \left( \frac{Z_0}{\eta_0} \right) \left\{ 1 + \frac{2}{\pi W} \frac{\epsilon_r^s}{\epsilon_r^s} I(\epsilon_r^s, W, d) \right\}$$

$$\text{where } I(\epsilon_r^s, W, d) = \int_0^\infty (1 - \cos \alpha W) \left| \frac{1 + \epsilon_r^s \frac{\gamma_1}{\gamma_2} \tanh(\gamma_2 d)}{\gamma_1 \epsilon_r^s + \gamma_2 \tanh(\gamma_2 d)} \right|^2 d\alpha$$

It is seen that the change in slot wavelength is directly proportional to the differential permittivity  $\delta\epsilon_r$  and to the thickness  $t$  of the adhesive. The characteristic impedance  $Z_0$  of a slot line increases as the slot width  $W$  is increased. However, it increases at a rate slower than the increase in  $W$ . The overall effect of  $W$  in the above expression is that the magnitude of the change in slot wavelength decreases as the slot width is increased. The improper integral  $I(\epsilon_r^s, W, d)$  can be computed in a numerically efficient manner by extracting the asymptotic contribution of the integrand. As a sample calculation, when  $\epsilon_r^s = 20$ ,  $W/d = 0.695$  and  $d/\lambda_0 = 0.02$

$$\lambda'/\lambda_0 = 0.373, \quad Z_0 = 82.26 \text{ ohms}$$

For an adhesive with  $\epsilon_r^s = 3.25$  and  $t/d = 0.02$ , the above expression gives

$$\Delta\lambda'/\lambda' = +4.2 \times 10^{-2}$$

**APPENDIX B**

**MEASURED RADIATION PATTERNS**

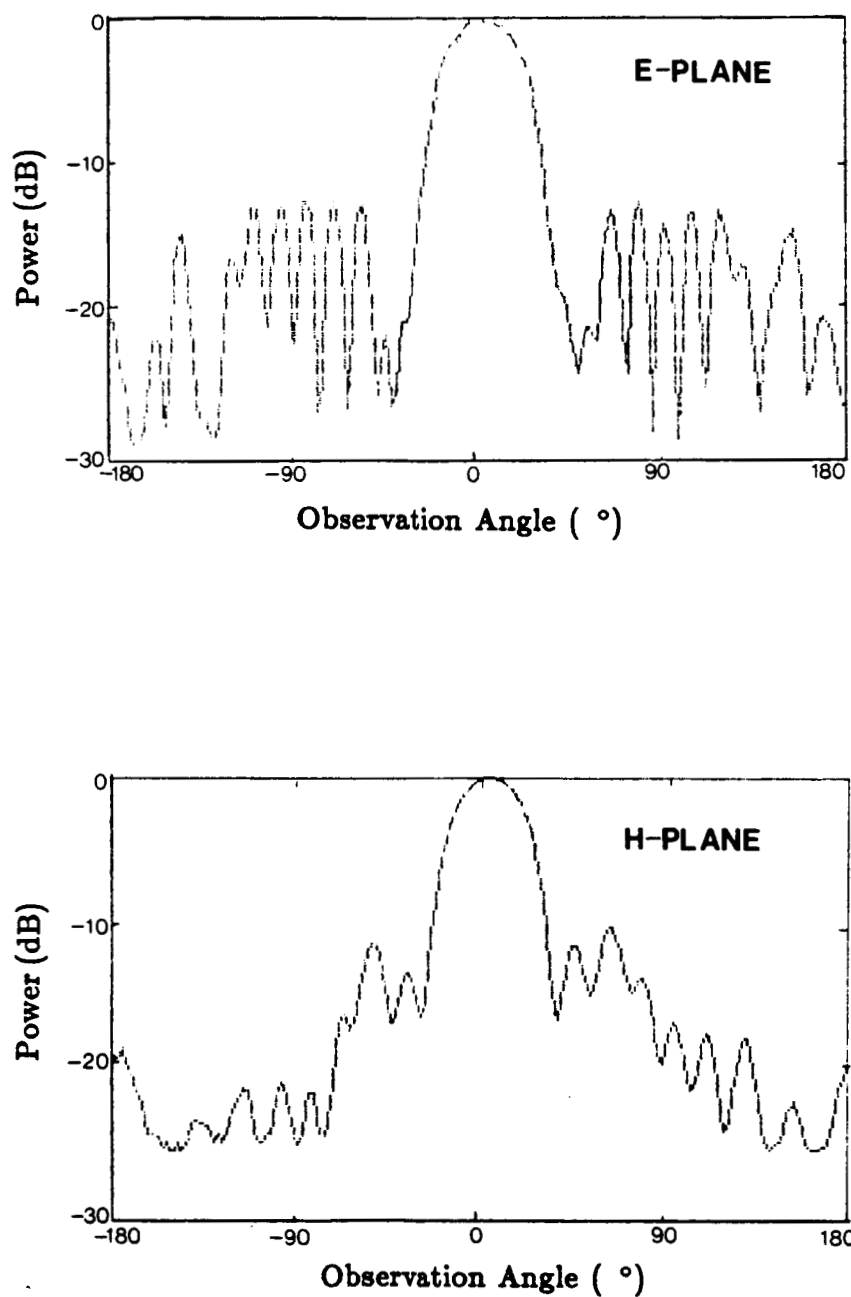


**Fig. B1.** Measured radiation pattern of LTSA on thin substrate.  
( $\epsilon_r = 2.22$ ,  $d = 20$  mils,  $L = 12.6$  cm,  $2\gamma = 10^\circ$ ,  $W_f = 1.5$  mm,  
 $W_o = 2.35$  cm,  $H = 7$  cm,  $f = 10$  GHz)

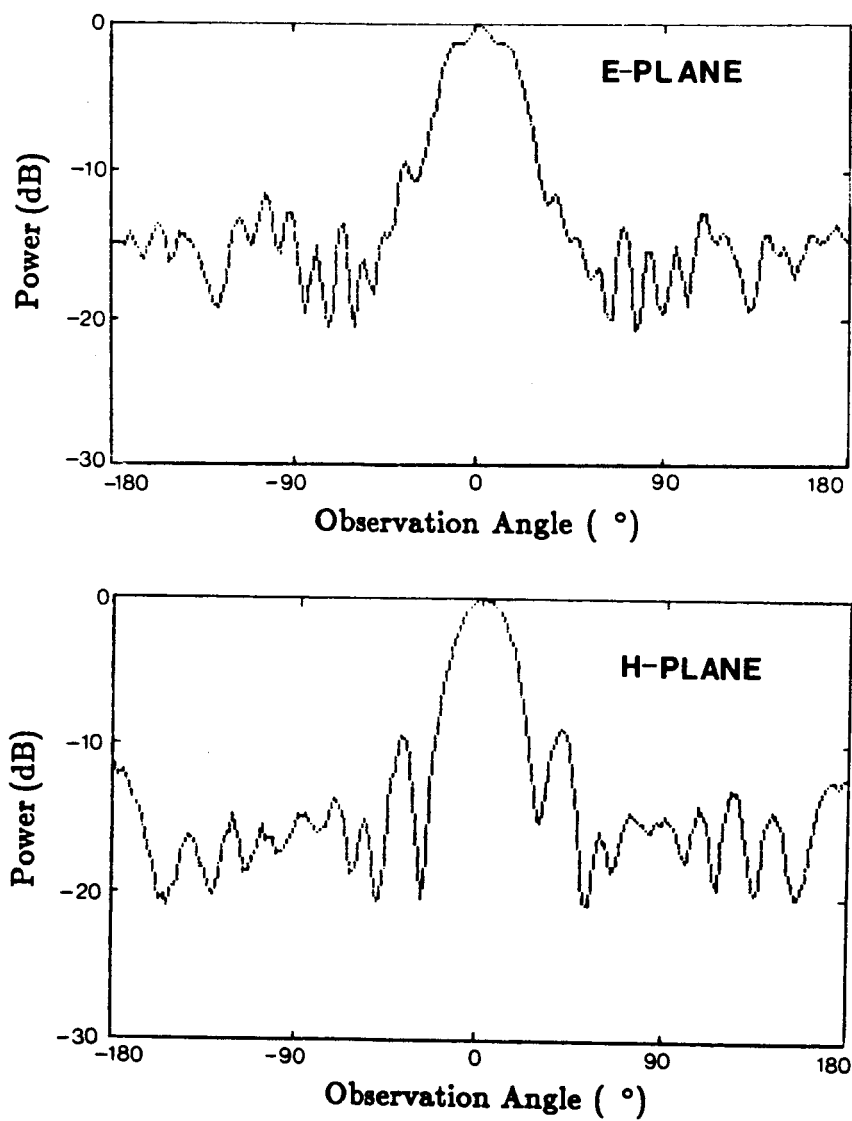


**Fig. B2.** Measured radiation pattern of LTSA on thin substrate.  
 ( $\epsilon_r = 2.22$ ,  $d = 20$  mils,  $L = 15.0$  cm,  $2\gamma = 16^\circ$ ,  $W_f = 1.5$  mm,  
 $W_o = 4.37$  cm,  $H = 10.2$  cm,  $f = 8$  GHz)



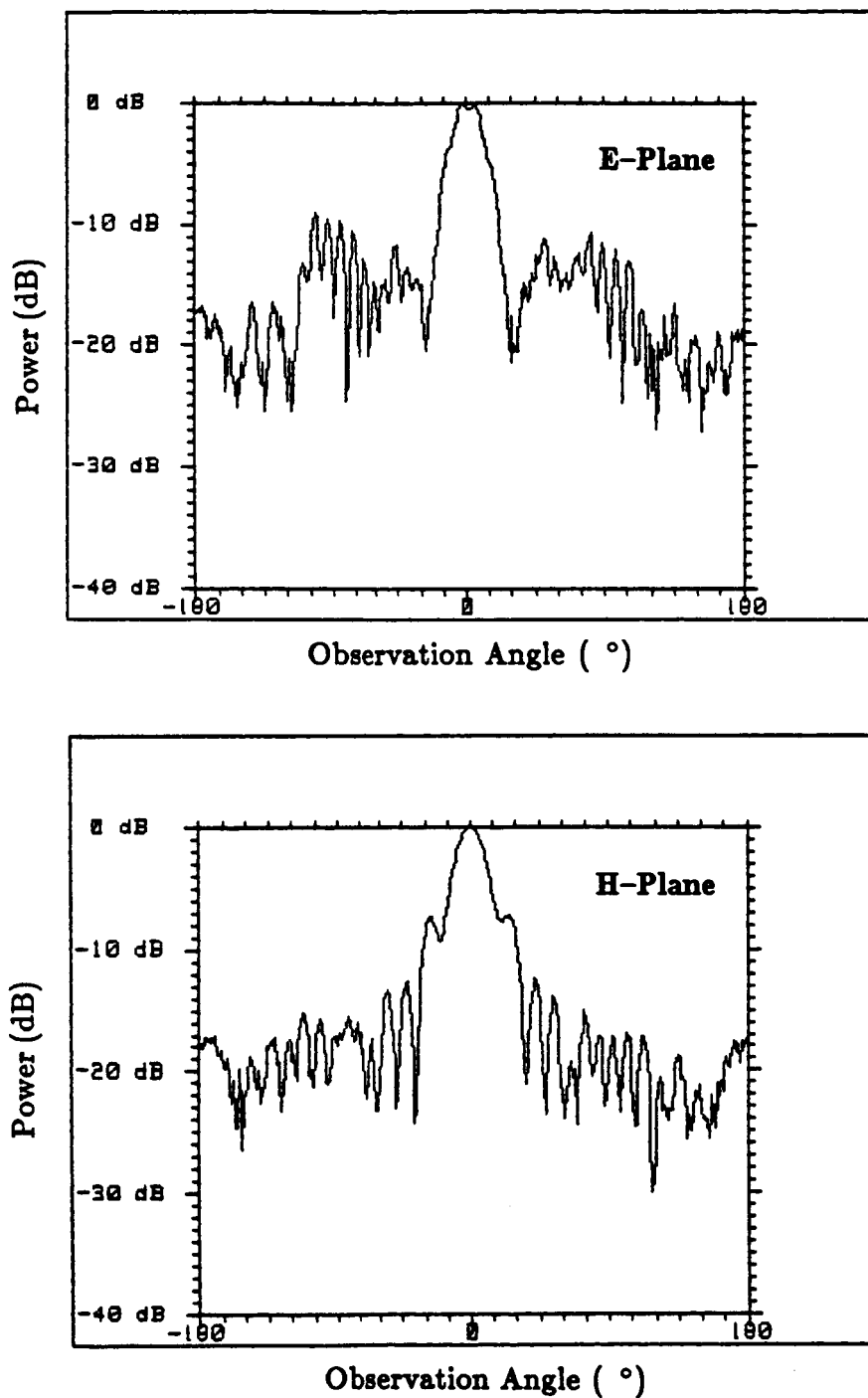


**Fig. B3.** Measured radiation pattern of LTSA on thick substrate.  
 ( $\epsilon_r = 2.22$ ,  $d = 59$  mils,  $L = 15.2$  cm,  $2\gamma = 14.25^\circ$ ,  $W_f = 0.5$  mm,  
 $W_o = 3.8$  cm,  $H = 12.7$  cm,  $f = 12$  GHz)

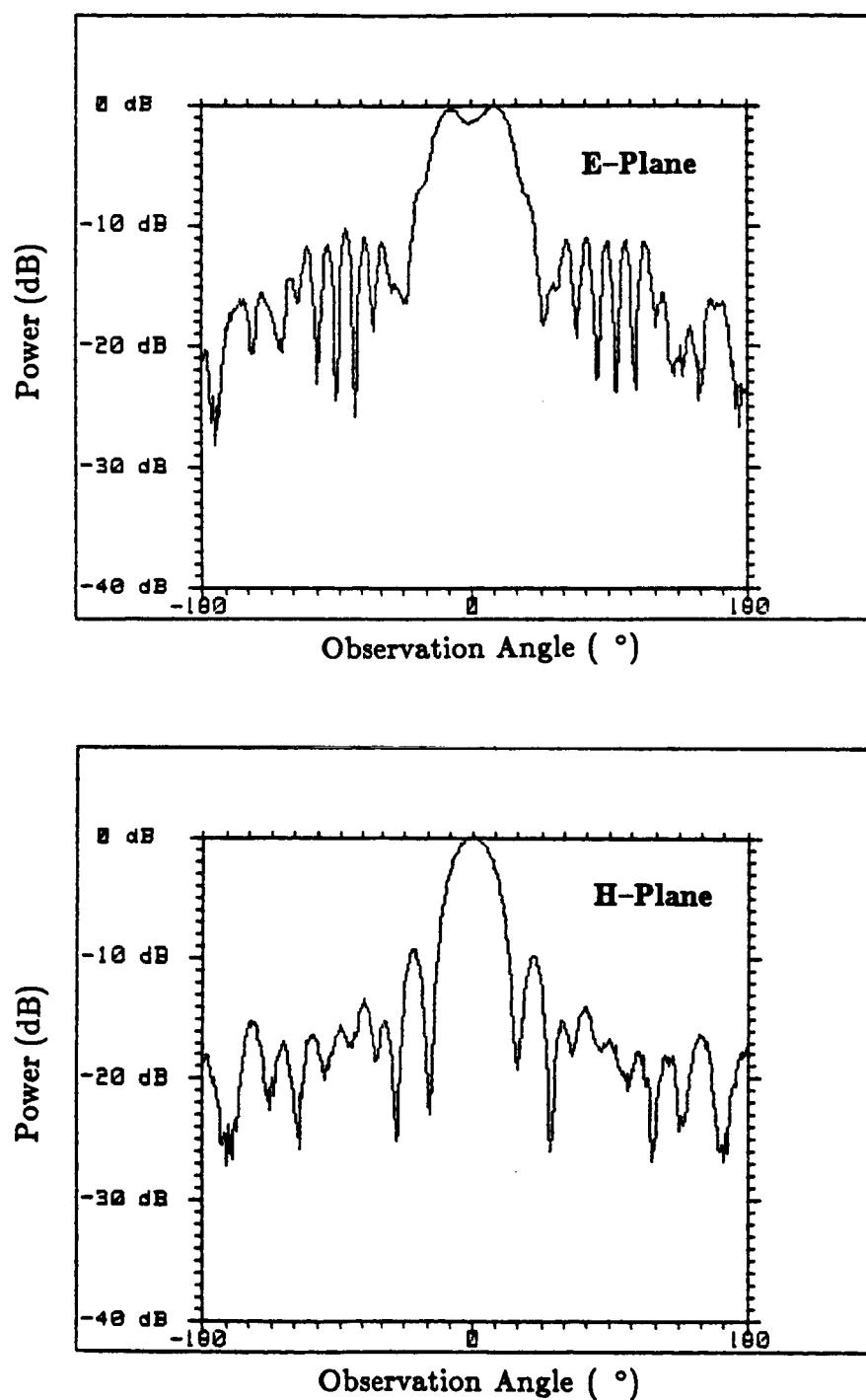


**Fig. B4.** Measured radiation pattern of LTSA on thick substrate.  
 $(\epsilon_r = 2.22, d = 59 \text{ mils}, L = 15.2 \text{ cm}, 2\gamma = 14.25^\circ, W_f = 0.5 \text{ mm},$   
 $W_o = 3.8 \text{ cm}, H = 12.7 \text{ cm}, f = 8 \text{ GHz})$

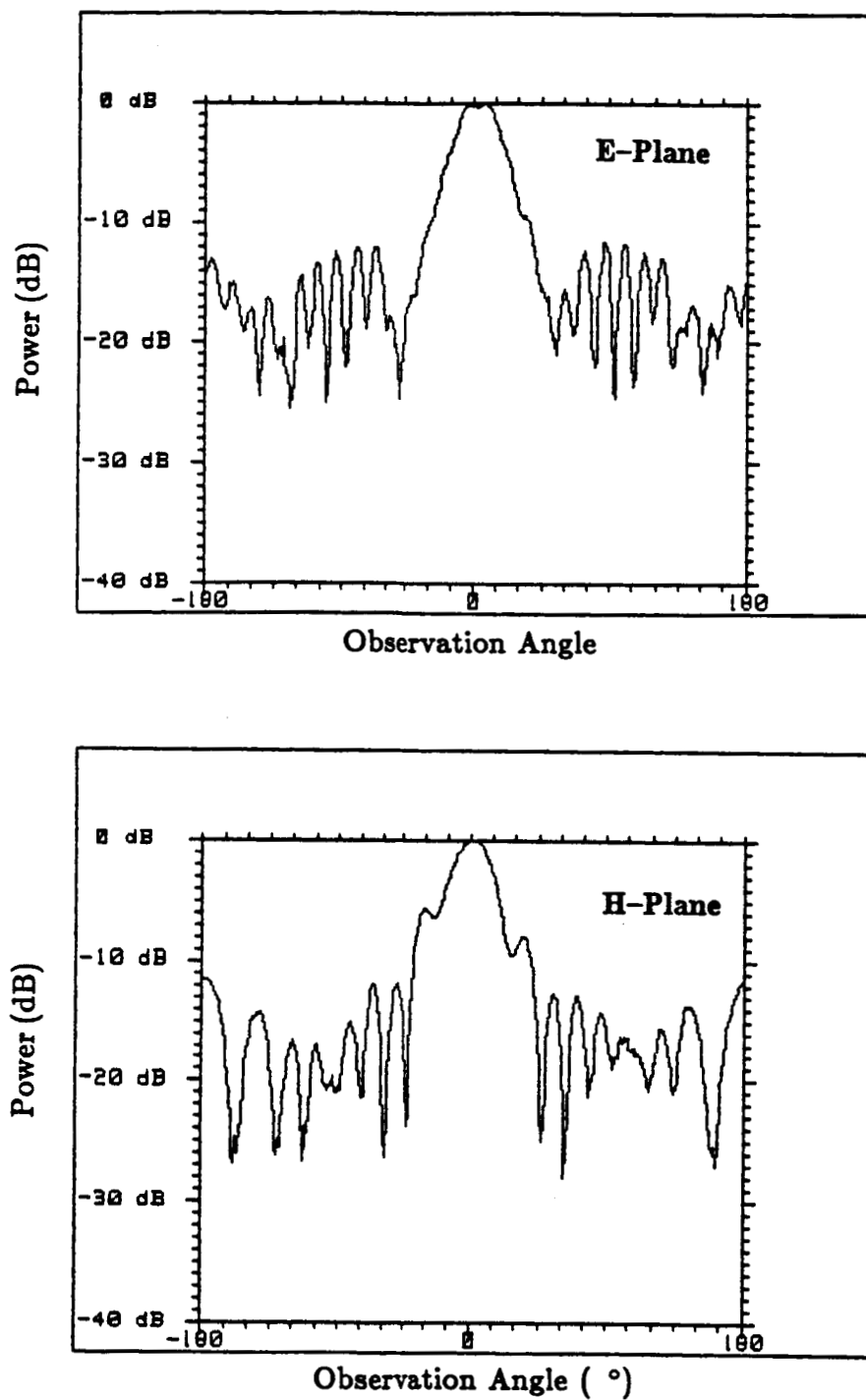


**Fig. B5.** Measured radiation pattern of LTSA on high- $\epsilon_r$  substrate.  
 ( $\epsilon_r = 10.5$ ,  $d = 10$  mils,  $L = 14.9$  cm,  $2\gamma = 14^\circ$ ,  $W_f = 0.5$  mm,  
 $W_o = 3.7$  cm,  $H = 12.7$  cm,  $f = 8$  GHz)

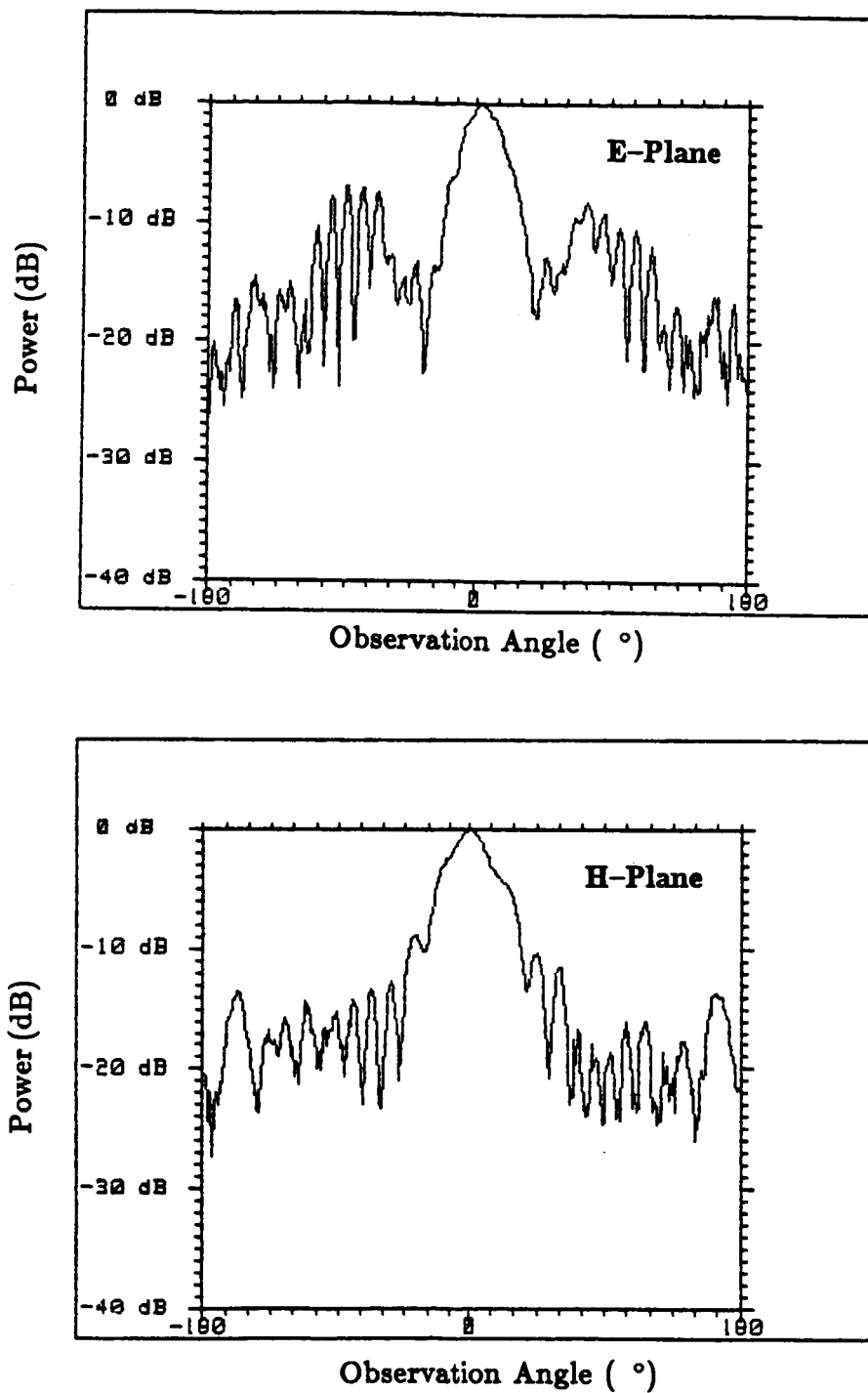


**Fig. B6.** Measured radiation pattern of LTSA on high- $\epsilon_r$  substrate.  
 $(\epsilon_r = 10.5, d = 10 \text{ mils}, L = 14.9 \text{ cm}, 2\gamma = 14^\circ, W_f = 0.5 \text{ mm},$   
 $W_o = 3.7 \text{ cm}, H = 12.7 \text{ cm}, f = 10 \text{ GHz})$

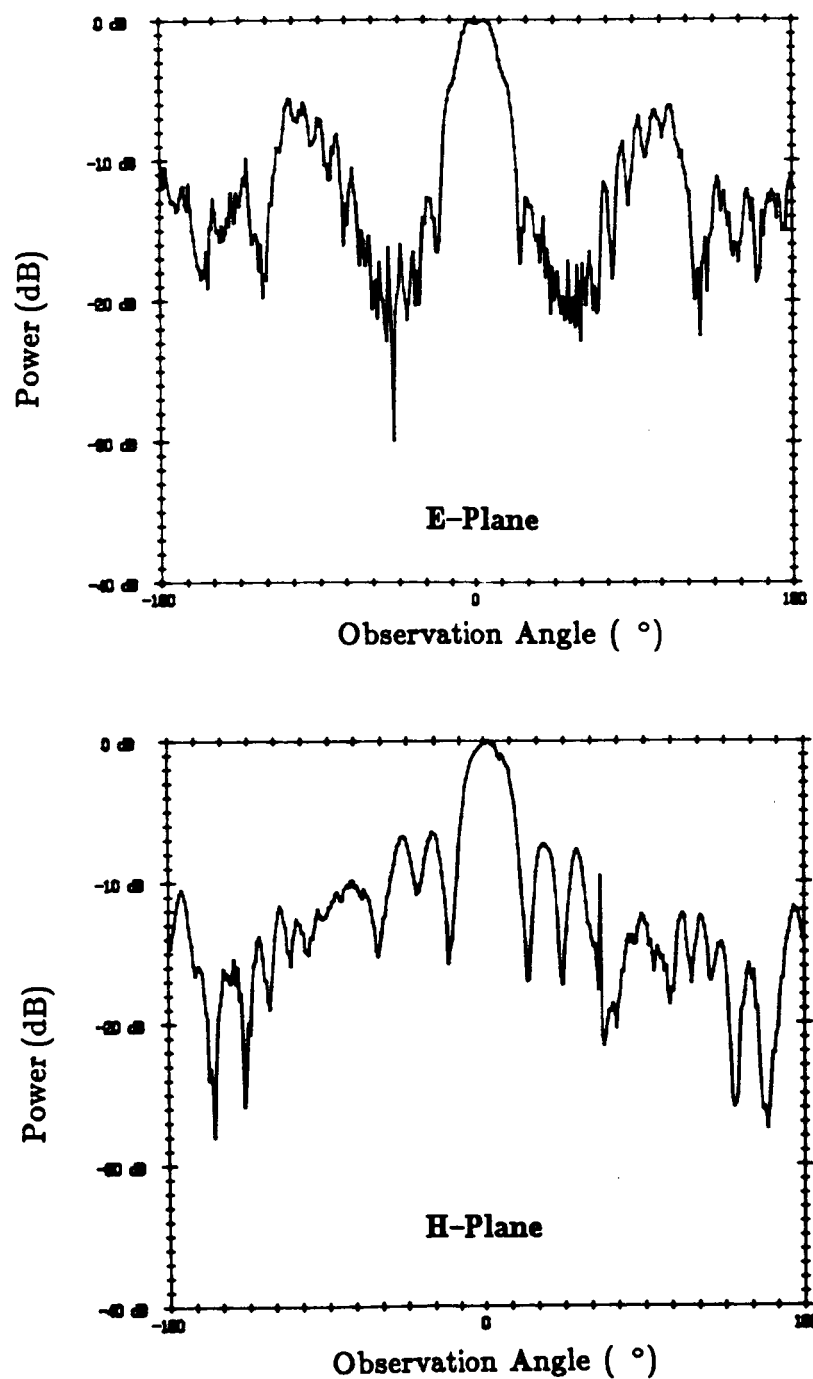
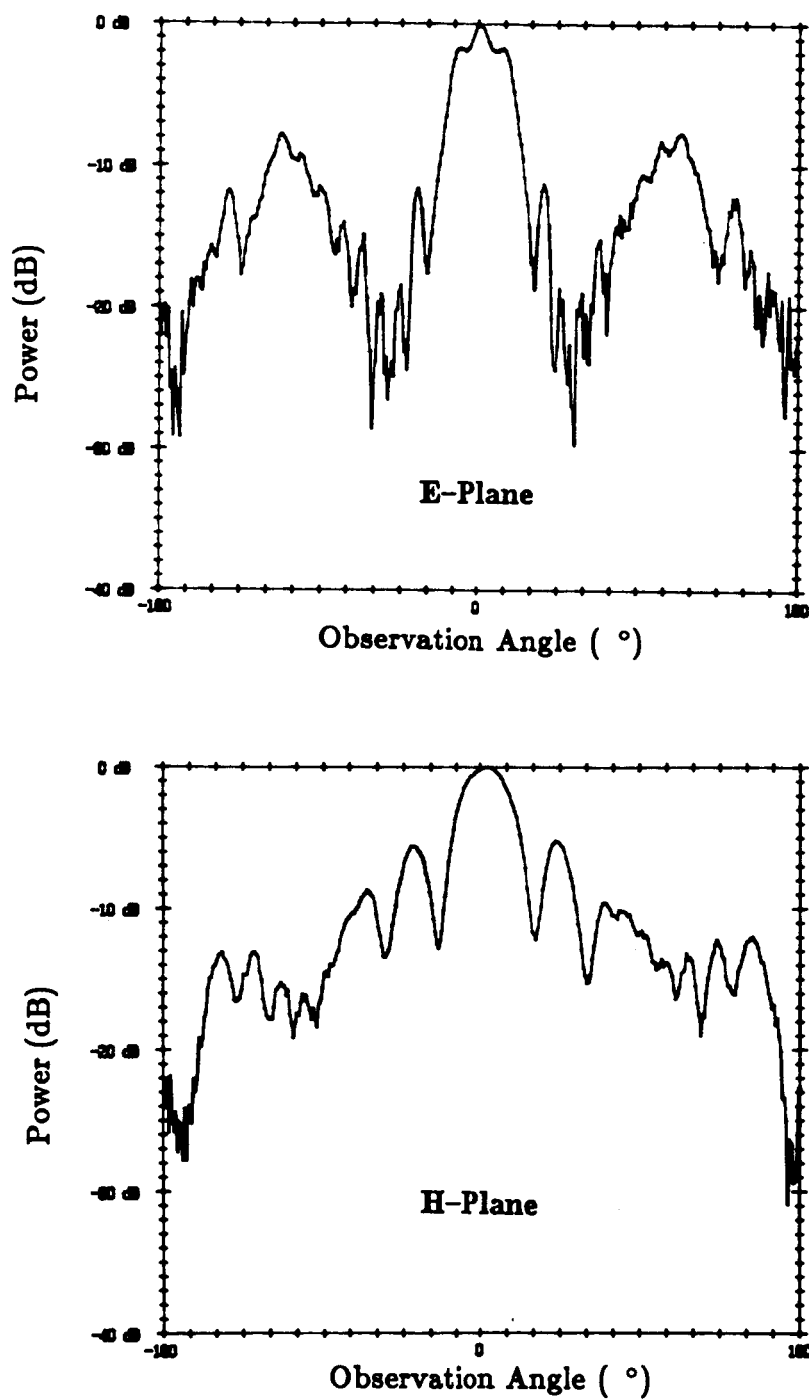
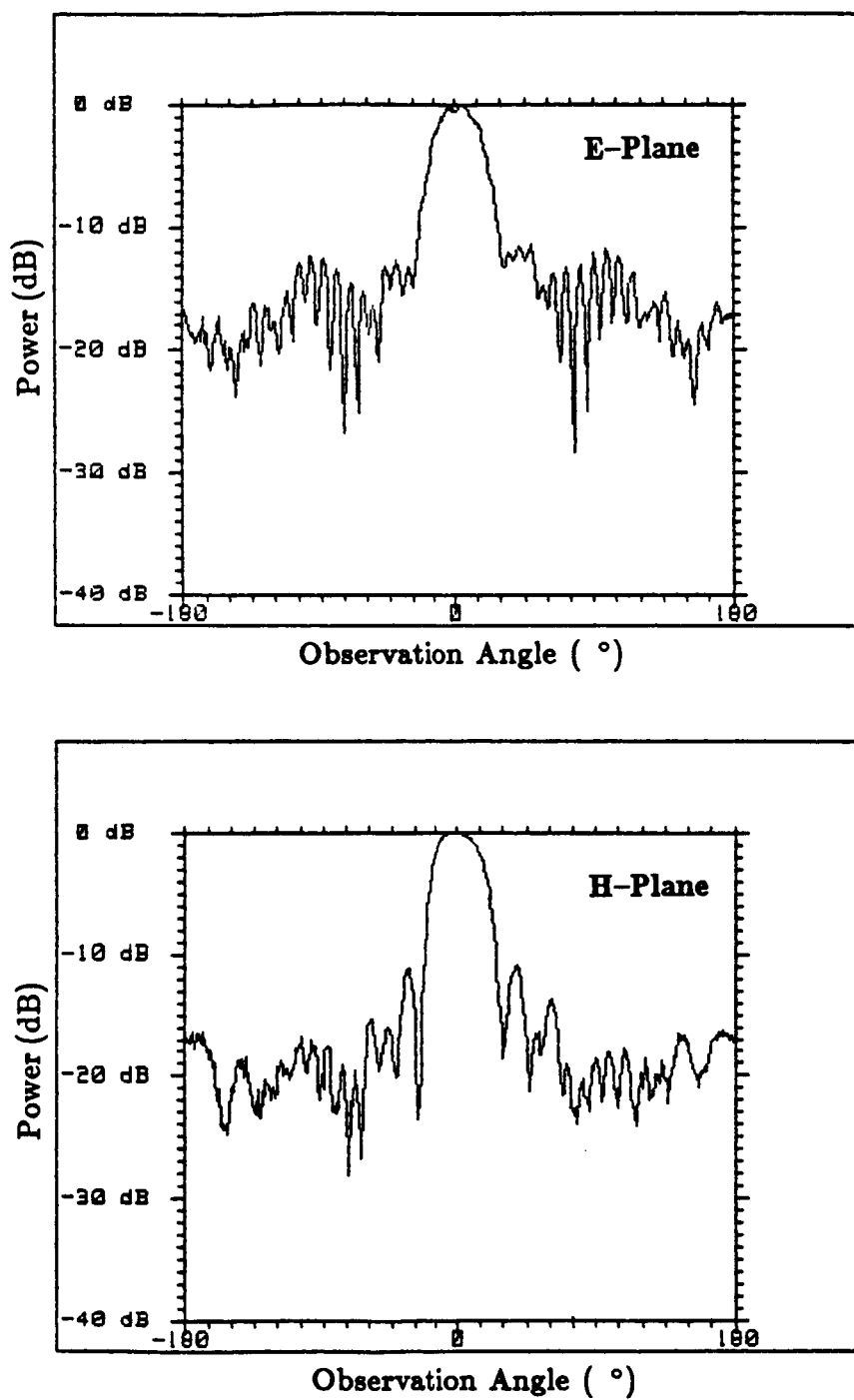


Fig. B7. Measured radiation pattern of CWSA on thin substrate.  
 $(\epsilon_r = 2.22, d = 20 \text{ mils}, L_f = 2.5 \text{ cm}, L_a = 14.8 \text{ cm}, W_f = 0.5 \text{ mm},$   
 $W_o = 2.95 \text{ cm}, H = 12.7 \text{ cm}, f = 10 \text{ GHz})$



**Fig. B8.** Measured radiation pattern of CWSA on thin substrate.  
 ( $\epsilon_r = 2.22$ ,  $d = 20$  mils,  $L_f = 2.5$  cm,  $L_a = 14.8$  cm,  $W_f = 0.5$  mm,  
 $W_o = 2.95$  cm,  $H = 12.7$  cm,  $f = 8$  GHz)



**Fig. B9.** Measured radiation pattern of Vivaldi antenna.  
 ( $L = 18.9$  cm,  $W_f = 1.2$  mm,  $W_o = 5.3$  cm,  $H = 12.7$  cm,  $f = 10$  GHz)

## BIBLIOGRAPHY

- [1] CARREL, R. L., The characteristic impedance of two infinite cones of arbitrary cross section, *IRE Trans. Antennas and Propagation*, vol. AP-6, pp. 197-201, 1958.
- [2] COHN, S. B., Slot line on a dielectric substrate, *IEEE Trans. Microwave Theory and Techniques*, vol. MTT-17, pp. 768-778, October 1969.
- [3] COLLIN, R. E., *Foundations for Microwave Engineering*, Chapter-5, McGraw-Hill Book Company, New York, 1966.
- [4] COLLIN, R. E., and F. J. ZUCKER (Eds.), *Antenna Theory*, pt. 2, Chapters 20-22, McGraw-Hill Book Company, New York, 1968.
- [5] ERDELYI, A., *Tables of Integral Transforms* vol. 2, McGraw-Hill Book Company, New York, 1954.
- [6] GARG, R., and K. C. GUPTA, Expressions for wavelength and impedance of a slot line, *IEEE Trans. Microwave Theory and Techniques*, vol. MTT-24, p. 532, August 1976.
- [7] GIBSON, P. J., The Vivaldi aerial, *Proc. 9<sup>th</sup> European Microwave Conference*, Brighton, U.K., pp. 120-124, 1979.
- [8] HANSEN, R. C. (Ed.), *Geometric Theory of Diffraction*, IEEE Press, New York, 1981.
- [9] HARRINGTON, R. F., *Time-Harmonic Electromagnetic Fields*, McGraw-Hill Book Company, New York, 1961.
- [10] ITOH, T., Spectral domain immittance approach for dispersion characteristics of generalized printed transmission lines, *IEEE Trans. Microwave Theory and Techniques*, vol. MTT-28, pp. 733-736, July 1980.
- [11] ITOH, T., and R. MITTRA, Dispersion characteristic of slot lines, *Electron Letters*, vol. 7, pp. 364-365, July 1971.
- [12] JANASWAMY, R., and D. H. SCHAUBERT, Dispersion characteristics for wide slot lines on low permittivity substrates, *IEEE Trans. Microwave Theory and Techniques*, vol. MTT-33, pp. 723-726, August 1985.
- [13] JANASWAMY, R., and D. H. SCHAUBERT, Analysis of the tapered slot antenna, *IEEE AP-S Symposium Digest*, vol. 2, Philadelphia, PA, pp. 689-692, June 1986.



- [14] JANASWAMY, R., and D. H. SCHAUBERT, Characteristic Impedance of a wide slot line on low permittivity substrates, *IEEE Trans. Microwave Theory and Techniques*, vol. MTT-34, pp. 900-902, August 1986.
- [15] JANASWAMY, R., D. H. SCHAUBERT, and D. M. POZAR, Analysis of the TEM-Mode linearly tapered slot antenna, to appear in *Radio Science*.
- [16] KITAZAWA, T., Y. FUJIKI, and M. SUZUKI, Slot line with thick metal coating, *IEEE Trans. Microwave Theory and Techniques*, vol. MTT-21, pp. 580-582, September 1973.
- [17] KNORR, J. B., and J. SAENZ, The effect of surface metal adhesive on slot line wavelength, *IEEE Trans. Microwave Theory and Techniques*, vol. MTT-21, pp. 642-644, October 1973.
- [18] KNORR, J. B., and J. KUCHLER, Analysis of coupled slots and coplanar strips on dielectric substrate, *IEEE Trans. Microwave Theory and Techniques*, vol. MTT-23, pp. 541-548, July 1977.
- [19] KORZENIOWSKI, T.L., *A 94 GHz Imaging Array Using Slot Line Radiators*, Ph.D. Dissertation, University of Massachusetts, September 1985.
- [20] KORZENIOWSKI, T. L., D. M. POZAR, D. H. SCHAUBERT, and K. S. YNGVESSON, Imaging system at 94 GHz using tapered slot antenna elements, presented at the *Eighth-IEEE International Conference on Infrared and Millimeter Waves*, Miami Beach, Florida, 1983.
- [21] MARIANI, E. A., C. P. HEINZMAN, J. P. AGRIOS, and S. B. COHN, Slot line characteristics, *IEEE Trans. Microwave Theory and Techniques*, vol. MTT-17, pp. 1091-1096, December 1969.
- [22] MILLIGAN, T. A., *Modern Antenna Design*, McGraw-Hill Book Company, New York, 1985.
- [23] POZAR, D. M., *On Moment Method Solutions for Plate and Wire Geometries*, Ph.D. Dissertation, The Ohio State University, 1980.
- [24] PRASAD, S. N., and S. MAHAPATRA, A novel mic slot line aerial, *Proc. 9<sup>th</sup> European Microwave Conference*, Brighton, U.K., pp. 120-124, 1979.
- [25] TAI, C. T., *Dyadic Green's Function in Electromagnetic Theory*, Intext Educational Publishers, Scranton, Pennsylvania, 1971.

- [26] YNGVESSON, K. S., D. H. SCHAUERT, T. L. KORZENIOWSKI, E. L. KOLLBERG, T. THUNGREN, and J. F. JOHANSSON, Endfire tapered slot antennas on dielectric substrates, *IEEE Trans. Antennas and Propagation*, vol. AP-33, pp. 1392-1400, December 1985.